ABSTRACT

Title of Document: DRUG DELIVERY THROUGH THE BLOOD-BRAIN BARRIER THROUGH USE OF VASCULAR CELL ADHESION MOLECULE 1-TARGETED NANOPARTICLES

Sakib Adnan, Regina Borsellino, Alice He, Somdutta Mukherjee, Victor Peng, Karthya Potti, Kelly Shih, Janina Vaitkus, Victor Wang, Rani Woo, Robert Zhang

Directed By: Dr. Jose Helim Aranda-Espinoza

The blood brain barrier (BBB) is a semi-permeable membrane separating the brain from the bloodstream, preventing many drugs that treat neurological diseases, such as Alzheimer's and Parkinson's, from reaching the brain. Our project aimed to create a novel drug delivery system targeting the brain during neural inflammation. We developed a cationic solid lipid nanoparticle (CSLN) complex composed of cationic nanoparticles, biotin, streptavidin, and anti-vascular cell adhesion molecule-1 (anti-VCAM-1) antibodies. The anti-VCAM-1 antibody is used to target VCAM-1, a cell adhesion protein found on the BBB endothelium. VCAM-1 expression is elevated in the presence of inflammatory molecules, such as tumor necrosis factor-alpha (TNF-α). Through the use of a simple BBB model, results showed that our novel drug delivery system experienced some level of success in targeting the brain inflammation due to increasing TNF-α concentrations. This is promising for drug delivery research and provides support for VCAM-1 targeting using more robust and complex BBB models.

DRUG DELIVERY THROUGH THE BLOOD-BRAIN BARRIER THROUGH USE OF VASCULAR CELL ADHESION MOLECULE 1-TARGETED NANOPARTICLES

By

Team B^3: Team Blood Brain Barrier

Sakib Adnan, Regina Borsellino, Alice He, Somdutta Mukherjee, Victor Peng, Karthya Potti, Kelly Shih, Janina Vaitkus, Victor Wang, Rani Woo, Robert Zhang

Thesis submitted in partial fulfillment of the requirements of the Gemstone Program University of Maryland, College Park 2013.

Advisory Committee:
Dr. Jose Helim Aranda-Espinoza
Dr. Zhihong Nie
Dr. Avis Cohen
Dr. Kimberly Stroka
Dr. Heather Hayenga
Dr. Daniel Butts

Acknowledgements

We would like to first thank our mentor, Dr. Helim Aranda-Espinoza for his guidance over the past three years along with all the members of his lab. We would also like to thank our discussants, Dr. Zhihong Nie, Dr. Avis Cohen, Dr. Kimberly Stroka, Dr. Heather Hayenga, and Dr. Daniel Butts for taking the time to review our thesis and give us feedback. Our thanks is also extended to the Atlantic Coast Conference Inter-institutional Academic Collaborative (ACCIAC) and the Howard Hughes Medical Institute (HHMI) for their generous grants to support our research. Our gratitude also goes out to the Gemstone program that gave us the opportunity and funding to engage in this team research. Finally, we would like to thank all of our friends and family for their unwavering support in all our endeavors.

Table of Contents

List of Figures

List of Tables

List of Abbreviations

ACBRI 376 – Applied Cell Biology Research Institute
ALCAM – Activated Leukocyte Cell Adhesion Molecule
ALS – Amyotrophic Lateral Sclerosis
ANG-1 – Angiopoietin-1
BBB – Blood Brain Barrier
CBSA – Cationic Bovine Serum Albumin
CMC – Critical Micelle Concentration
CNS – Central Nervous System
CSF – Cerbrospinal Fluid
CSLN – Cationic Solid Lipid Nanoparticle
EC – Endothelial Cells
ECGS – Endothelial Cell Growth Supplement
FBS – Fetal Bovine Serum
FGF – Fibroblast Growth Factor
FITC – Fluorescein Isothiocyanate
Gb3 – Globotriaosylceramide
GDNF – Glial-Derived Neurotrophic Factor
GSL – Glycosphingolipid
HBMEC – Human Brain Microvascular Endothelial Cell
HUVEC – Human Umbilical Vein Endothelial Cell
IDE – Idebenone
ICAM-1 – Intercellular Adhesion Molecule 1
ICAM-2 – Intercellular Adhesion Molecule 2
ISF – Interstitial Fluid
JAM – Junction Adhesion Molecule
LDL – Low Density Lipoprotein
MFI – Mean Fluorescence Intensity
MPC – Mean Fluorescence Intensity per Cell
NIH – National Institute of Health
NP – Nanoparticle
NVU – Neurovascular Unit
RPMI – Roswell Park Memorial Institute
SLC – Solute Carrier Transporter
SLN – Solid Lipid Nanoparticle
TEER – Transendothelial Electrical Resistance
TGF-β – Transforming Growth Factor
TJ – Tight Junction
TNF-α – Tumor Necrosis Factor Alpha
VCAM-1 – Vascular Cell Adhesion Molecule-1
VLP – Virus-Like Particle

1. Introduction

1.1 Research Problem

Millions of people struggle emotionally and physically with terminal neurological pathologies, many of which are rooted in the brain. The blood brain barrier (BBB) is the brain's defense mechanism against outside compounds. The BBB is a highly selective, semipermeable membrane that regulates passage of molecules from the circulatory system into the central nervous system (CNS). Although the BBB is beneficial in protecting the brain from harmful molecules in the bloodstream, it also prevents life-saving drugs from reaching the CNS. Technology today has advanced to the point where pharmaceuticals have the potential to treat and cure specific neurological maladies, yet these potentially life-saving medicines are hindered simply by the membrane that filters access to the brain. If drug treatments were able to bypass the BBB and gain access to the brain, the medical community would be a significant step closer to curing many neurological maladies. Diseases such as Alzheimer's, multiple sclerosis, or meningitis would potentially be less harmful and possibly curable.

The selective permeability of the BBB only allows certain substances directly related to maintenance of brain homeostasis and function to diffuse. Certain hydrophobic molecules can permeate, whereas hydrophilic molecules such as proteins and peptides are prevented from crossing the BBB.[1] The complexity of the BBB composition and certain pathways for transversal are shown in Figure 1. This constraint severely limits the research and development into drugs to treat neurological diseases because of the BBB obstacle. Currently, there are a number of ways that researchers have begun to try and

permeate the BBB, mostly through transport mechanisms that target certain adhesion molecules on the BBB structure to facilitate diffusion. Among those transport mechanisms are using T-cells, viruses, micelles, and nanoparticles. However, there is yet to be a proven method stable enough to stimulate significant development of additional neurological drugs. Thus, this project seeks to find a novel and effective delivery system that can cross the BBB so that in the future, researchers may be able to adapt this method and carry it further by targeting specific sites beyond the BBB.

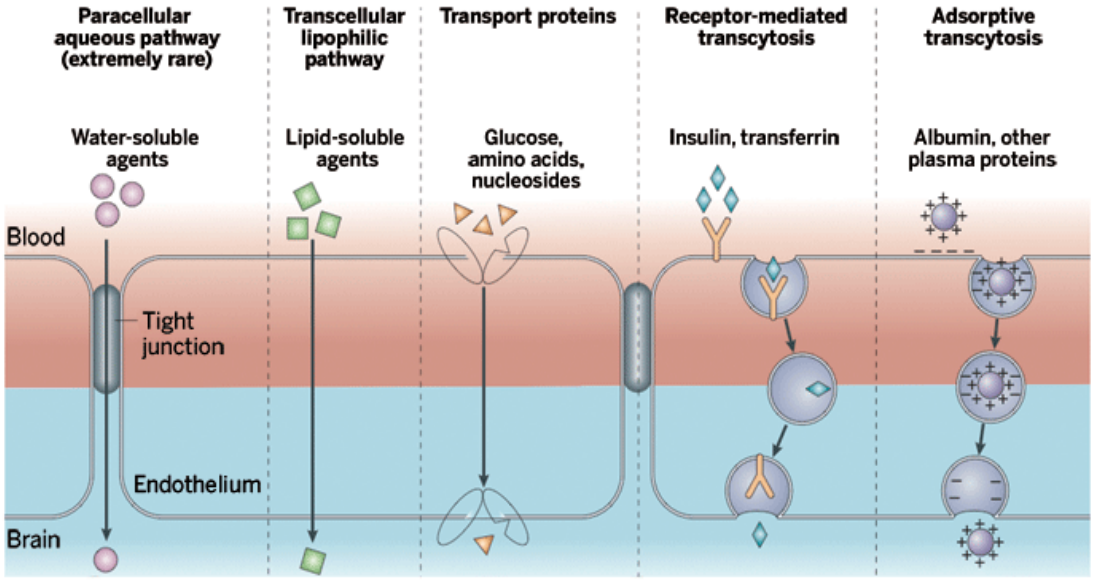

Figure 1. Varying methods and pathways of molecular transmigration across the BBB. Nature, http://www.nature.com/nrn/journal/v7/n1/fig_tab/nrn1824_F3.html

1.2 Team Research Focus

This project focuses on finding a novel drug delivery method to permeate the BBB. We chose to focus our project on the use of a nanoparticle-antibody complex as a transportation method to ferry drugs into the brain and treat neurological diseases. It is known that antibody targeting can be used to transport material into individual cells. In addition, drugs can be encapsulated through the use of nanoparticles. The focus of this

research project is twofold: to create a working *in vitro* BBB model that simulates the complex interactions that a real BBB would have, and to create a nanoparticle-antibody complex that will permeate the BBB model. Our targeting method of choice is through vascular cell adhesion molecule-1 (VCAM-1), a molecule present on the surface of the BBB endothelium. The logic behind our decision is that inflammation in the brain, often instigated by disease, results in the presence of a cytokine, tumor necrosis factor alpha (TNF-α) which, in turn, up-regulates the presence of VCAM-1. Therefore, neurologically diseased brains have increased amounts of VCAM-1. Thus, we decided to use a VCAM-1 targeting antibody in our nanoparticle-antibody complex to facilitate permeation through our *in vitro* BBB model.

1.2.1 Research Question

Specifically, the questions that will be assessed are (1) will an increase in TNF-α up-regulate the presence of VCAM-1 on an *in vitro* BBB model, (2) is it possible to construct a cationic solid lipid nanoparticle (CSLN)-antibody complex that targets VCAM-1, (3) will the streptavidin-biotin interaction be strong enough to stabilize the CSLN-antibody complex, and (4) will targeting VCAM-1 on endothelial cells (EC) be a viable way to get drugs encapsulated by a CSLN-antibody complex through the *in vitro* BBB model? Streptavidin and biotin are receptors that we will use to join together the nanoparticles and VCAM-1 targeting antibodies. We will use a fluorescent dye encapsulated in the nanoparticles to simulate potential drugs.

1.3 Research Hypothesis

The main approach taken was to construct a stable CSLN-antibody complex that would permeate the BBB model by targeting VCAM-1. The nanoparticle will serve as a vessel for our drug substitute. The biotinylated anti-VCAM-1 antibody is to ensure that our vessel is successful in both traversing the BBB and targeting VCAM-1. The stability of our drug delivery method is heavily dependent on the streptavidin-biotin complex, which is one of the strongest non-cationic bonds formed in nature.

For the first component of our experiment in creating an *in* vitro BBB model, we expect to be able to successfully create an *in vitro* BBB model at varying levels of inflammation with the use of TNF-α. We used TNF-α because past studies have found that the increased presence of TNF-α also up-regulates the expression of VCAM-1 on the BBB (see Figure 2).[2]

In the second component of our experiment of creating a transport method, we expect to create a CSLN-antibody complex using the streptavidin-biotin interaction to stabilize the connection between the dye-infused CSLN and VCAM-1 targeting antibody.

Finally, when combining the CSLN-antibody complex with our *in vitro* BBB model, we expect that the CSLN-antibody complex will permeate the barrier at higher levels than the simple nanoparticle control. We also hypothesize that we will see a gradual uptrend in uptake of the CSLN-antibody complex by the *in vitro* BBB model with increasing levels of TNF-α.

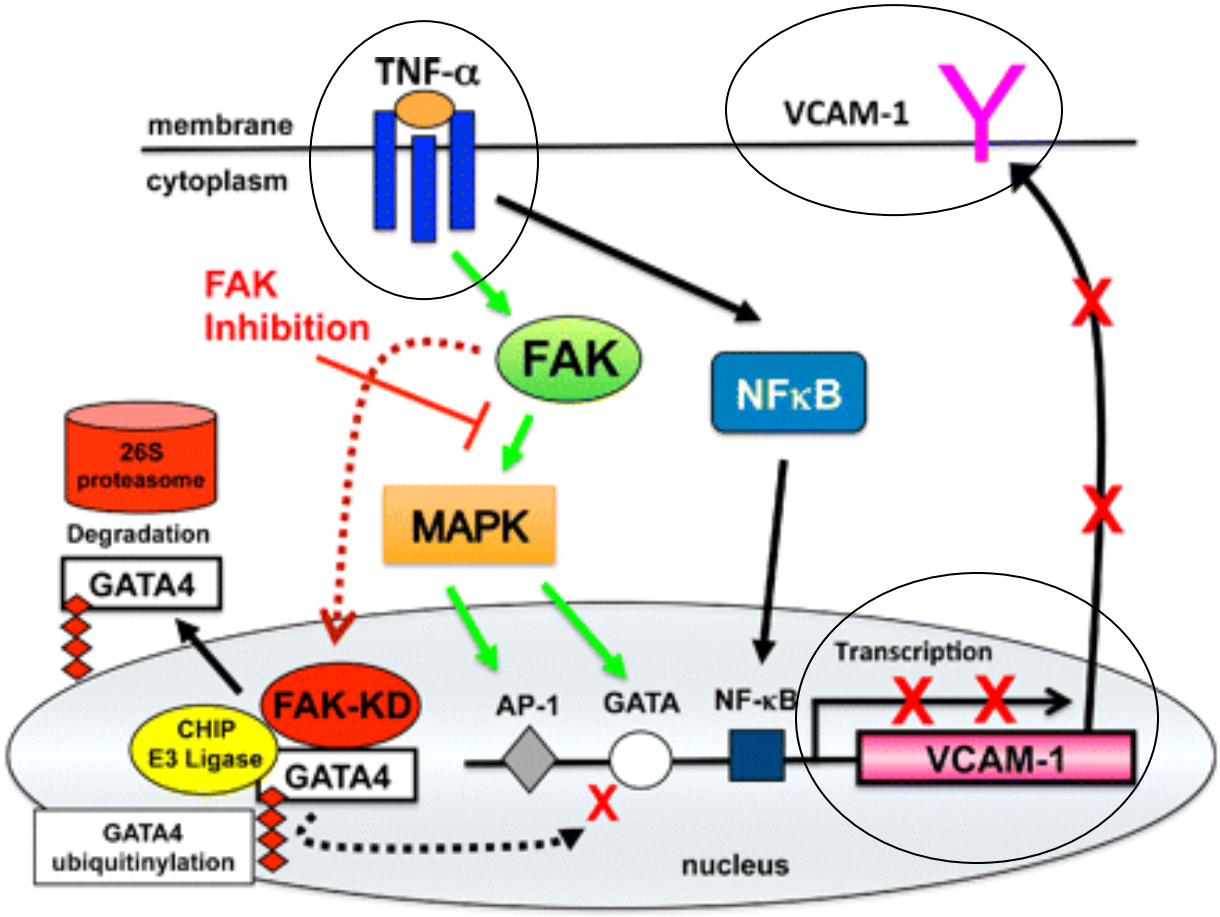

Figure 2. Presence of TNF-α in the regulation of VCAM-1 expression**.** TNF-α binding to cell surface receptors triggers intracellular signaling cascade activation, which results in the transcription of VCAM-1.
Journal of Cell Biology, http://jcb.rupress.org/content/197/7/907.long

1.4 Objectives

Ultimately, the goal of our research was to devise a novel method of drug delivery that can be expanded on in the future. We hoped to conclude that targeting VCAM-1 on brain ECs would increase the uptake of a modified nanoparticle drug delivery system through the BBB.

Our project focused on three distinct phases: creating an *in vitro* BBB model that mimics the properties of the real barrier, assembling an antibody-nanoparticle complex, and combining the two elements to test the complex's ability to transverse the BBB

model. Thus, our BBB sub-team and nanoparticle sub-team worked simultaneously until the *in vitro* BBB model was created and the antibody-nanoparticle complex was constructed. The two teams proceeded to work together in testing the CSLN-antibody complex's ability to transverse the BBB model.

In the first phase in which the *in vitro* BBB model was created, the first objective was to create a dependable, consistent monolayer of Human Brain Microvascular Endothelial Cells (HBMECs) and Human Umbilical Vein Endothelial Cells (HUVECs) on which to test our experiments. The HBMECs represent the layer of cells on the surface of the BBB whereas the HUVECs are a similar type of EC. The next objective in the first phase was to add various levels of TNF-α to the monolayer of HUVECs and observe immunofluorescent staining of VCAM-1. The third objective was to utilize fluorescent microspheres to determine whether the BBB model functions properly in taking up molecules.

Simultaneously occurring was the second phase during which the antibody-nanoparticle complex was assembled. The first objective was to create the nanoparticle. The next objective was to add streptavidin to the nanoparticle so that it would attach to the biotinylated anti-VCAM-1. Following the addition of streptavidin to the nanoparticle, the next objective was to ensure that the streptavidin-nanoparticle complex would attach to biotin by using biotin-coated plates. The final objective was to create the final complex and attach biotinylated antibodies to the streptavidin-nanoparticle complex.

In the final phase where the BBB model and nanoparticle complex were combined, the sole objective was to observe whether the CSLN-antibody complex crosses the BBB model. Our experiment sought to find correlation between how damaged

the BBB was, and how much penetration and attachment our drug delivery method could achieve.

1.5 Research Significance

The conclusion of our research shows that there is another viable method of drug delivery through the BBB. Our CSLN-antibody complex encapsulates a drug-simulating dye and delivers it across the BBB to targeted cells. The benefits of our research could potentially progress the field of drug delivery through the BBB. If our drug delivery vehicle were compatible with drugs capable of delaying or curing neurological diseases, then this would spur more research and development into creating such drugs. Patients afflicted with neurological diseases like Alzheimer's, multiple sclerosis, or meningitis would have more potential for treatment. Also, if treated early enough, it is possible that victims would experience just a fraction of the symptoms that they would normally experience because of lessened neurological damage.

These findings can potentially be used to aid other research groups' methods. Given that the CSLN-antibody complex is able to permeate the BBB successfully, other researchers can then investigate methods of inserting other drugs into our CSLN, or a more efficient means of building the complex for specific diseases. There are also many possibilities of improvement to our drug delivery vessel. Modifications to the complex could be made, whether to improve binding, add additional binding sites, or add additional space for drugs. Similarly, researchers could use our method of forming a vessel-binding complex to form other vehicles that carry different drugs to different sites.

We hope that our research can be used as a stepping-stone for other researchers to find more effective ways of permeating the BBB.

Not only will this research contribute to the possibility of successfully transporting a drug to cure diseases, but it will further general knowledge in the neurological and pharmaceutical research field. The molecules could be manipulated so that they may possibly serve purposes other than simple drug delivery.

1.6 Thesis Organization

This thesis is organized by the order of our experimental process. A literature review is presented in Chapter 2 to give additional context to the current stage of BBB understanding and drug delivery mechanisms available. Chapters 3 and 4 focus on the *in vitro* BBB model and nanoparticle complex, respectively. Both chapters include a more comprehensive background, methodologies for these preliminary experiments, data and results, as well as discussion of these preliminary results. Chapter 5 describes the combination of the two parts: using our CSLN-antibody complex to test permeability of the *in vitro* BBB model by targeting VCAM-1. This chapter includes a methodology, data and results, and a discussion of this main objective. Finally, Chapter 6 provides a conclusion that summarizes our objectives and results as well as describes limitations of our experiment and possible future directions.

2. Literature Review

2.1 Blood Brain Barrier

The BBB is the membranous, physical separation of the circulatory system from the CNS in an organism. Its presence was discovered in the late 19th century by German studies observing that dyes injected into the bloodstream would stain all other organs with the exception of the brain and spinal cord.[1] It was also found that acids injected directly into the brain produced seizures while those injected through other capillaries did not.[3] Researchers determined from these experiments the presence of a barrier between the fluid in the brain and the bloodstream—the BBB.

The BBB's main functions are to maintain homeostasis in the CNS, regulate the supply and passage of essential nutrients in the brain, protect the brain from extracellular objects, and induce inflammation in response to exogenous changes in the environment.[1,4] To accomplish these tasks, the BBB is composed of a unique physiological structure that functions as a selective gateway to the brain.

Most simply, the BBB is understood as a membrane surrounding capillaries running through the brain, separating these capillaries from the fluids of the brain.[3] While the blood portion of the BBB consists of the thin capillaries surrounding the CNS, the barrier portion consists of a monolayer of ECs that surround these capillaries. Individual cells of the CNS and circulatory system are in close contact to one another. Most CNS cells are no more than 40 μm apart from a capillary.[5]

The cellular building blocks of the BBB are brain microvascular ECs, pericytes, and astrocytes.[6] The ECs are held together by tight junctions (TJs) that control permeability through the BBB. The ECs are surrounded by an extracellular matrix called

the basement membrane that physically holds the EC layer in place.[7] Together these components are known as the neurovascular unit (NVU).

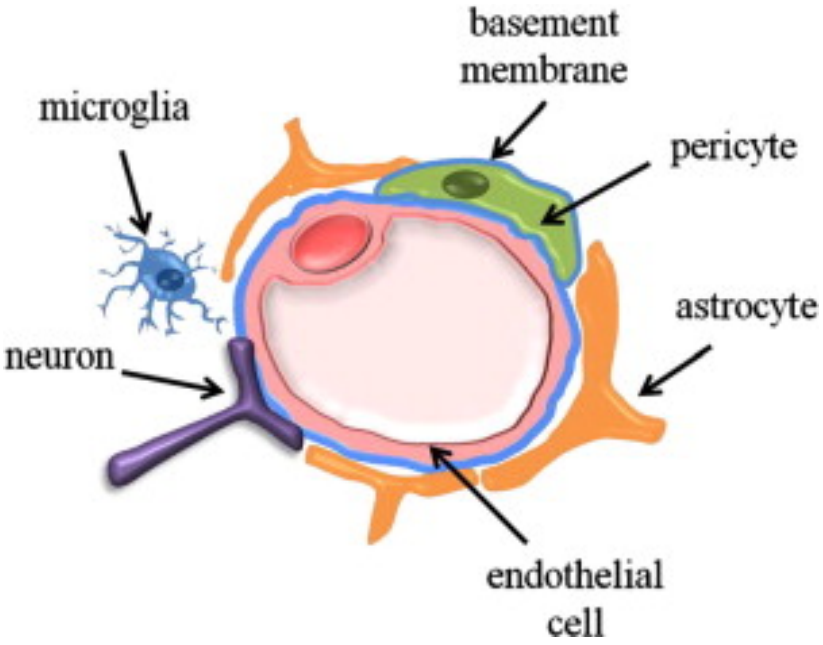

Figure 3. The neurovascular unit (NVU) with all of its components. The interactions between brain endothelial cells, astrocytes, pericytes, the basal lamina, and microglia create the neurovascular units
Brain Research Reviews,
http://www.sciencedirect.com/science/article/pii/S0165017310000676.

It is in the basement membrane that pericytes serve their function of providing physical support and regulating the ECs.[8] Astrocytes surround the basement membrane, attached by thin endfeet, and regulate interaction between neurons in the CNS, endothelium, and basement membrane of the BBB.[9] The direct association between astorcytes and ECs of the brain allow astrocytes to secrete substances into the BBB that contribute to its differentiation and impermeability. Pericytes are wrapped around the ECs to both provide structural support and regulate permeability. Both pericytes and astrocytes are essential to the differentiation of the BBB.

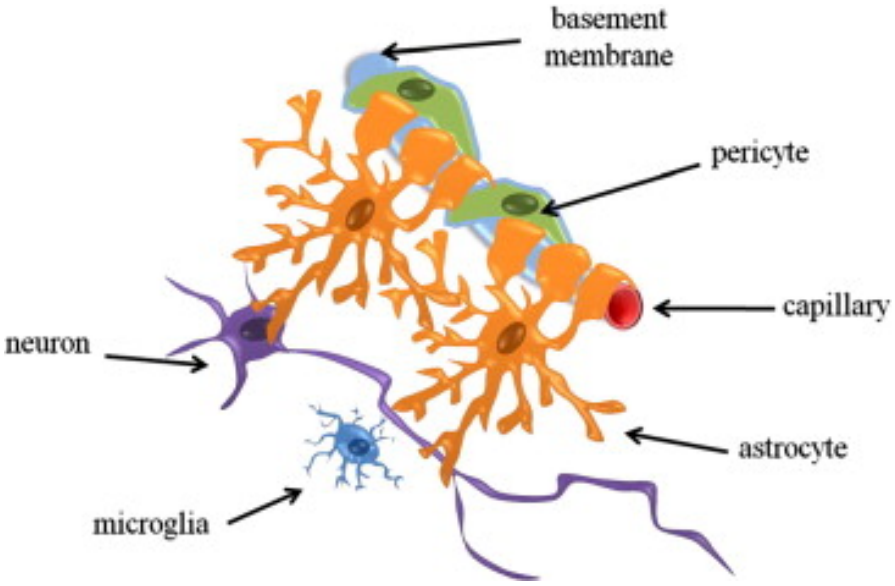

Figure 4. Side view of BBB components and their interactions. The interactions between brain endothelial cells, astrocytes, pericytes, the basal lamina, and microglia create the neurovascular units
Brain Research Reviews,
http://www.sciencedirect.com/science/article/pii/S0165017310000676.

The EC layer serves as the core of the BBB membrane. The brain is one of the most sensitive organs in the body, and thus functions only in certain physiological conditions. In order to maintain this strict range of conditions, the ECs serve as a selectively permeable membrane that highly regulates the paracellular and transcellular diffusion of molecules. Paracellular diffusion is the transport of molecules between individual cells, while transcellular diffusion is the transport of molecules through individual cells. The ECs allow the passage of small hydrophobic molecules, but retard the movement of most hydrophilic molecules through the BBB.[10] Only compounds that serve to uphold neurological function, such as glucose and amino acids, are able to permeate the barrier through the EC's expression of transport proteins.[4] The ECs of the brain are highly differentiated from other ECs in the body because of this capacity to control molecule passage through unique receptors and transporters.[11]

TJs are another essential component of BBB function and the main structure that creates the selectively permeable barrier properties.[1] TJs are formed by several proteins anchored between ECs, which fuse these cells together to prevent seepage of substances between cells.[12] These proteins include claudins, occludins, and junction adhesion molecules (JAMs). Claudins and occludins work together to form intramembranous strands that dictate selective diffusion of hydrophilic molecules.[6] Over forty proteins are associated with the TJ, making it the most complex element of the body's vasculature.[1]

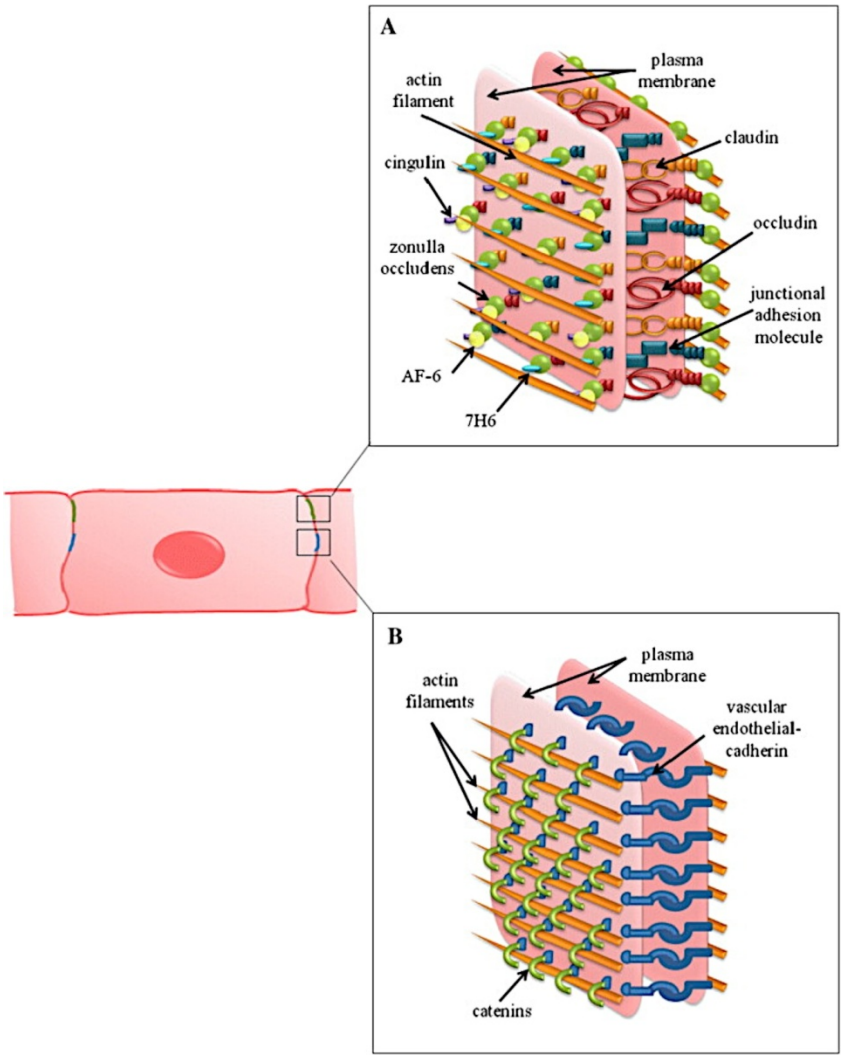

Figure 5. Breakdown of complex TJ components.
Brain Research Reviews,
http://www.sciencedirect.com/science/article/pii/S0165017310000676.

TJ functionality is associated with high transendothelial electrical resistance (TEER) values. High TEER values have been associated with the increased selectivity of the BBB, as shown by experimental observations tracking membrane electrical resistance in developing rat pups.[13] With increased electrical resistance, electron microscopy showed less atomic diffusion and increased TJ functionality.

2.1.1 Substrates and Types of BBB Models

The *in vivo* BBB consists of a single layer of ECs located in the brain capillaries that separate the bloodstream from the CNS. *In vivo* BBB models offer pinpoint representativeness of BBB biophysiology, but they are significantly more expensive, difficult to use, and limited in producing high throughput experiments when compared to *in vitro* BBB models.[14] *In vitro* BBB models still offer notable representativeness since they are commonly composed of a monolayer of brain ECs. At the very least, *in vitro* BBB models will be formed using ECs with similar protein expression found in cortical cells. Typically, an EC monolayer is attached upon glass or plastic with another layer of material called a substrate. Ideally, the EC monolayer will have similar biological properties as HBMECs, which comprise the *in vivo* BBB. However, porcine and murine ECs are usually used for *in vitro* studies since they are economic and easily obtainable.[15] However, for our purposes, we used HUVECs to form the monolayer as they have been shown to mimic many of the same biological functions of HBMECs in the *in vitro* BBB model.[16]

Several components of an *in vitro* BBB model contribute to the models overall ability to biologically represent the true BBB. For example, astrocytes play a crucial role

in the *in vitro* BBB model construct. Co-culture of astrocytes and ECs promotes TJ formation between ECs. The use of actual astrocytes in this co-culture, as opposed to conditioned media from astrocytes, is important to this model to simulate the cross-talk that occurs between astrocytes and ECs. It is expected that a larger astrocyte:EC ratio would produce a less permeable, stiffer BBB model, while a smaller ratio would produce a more permeable membrane.[10] Thus, variations in the astrocyte:EC ratio would mimic different BBB pathophysiological states, where a lower astrocyte:EC ratio would represent a more compromised BBB. However, astrocyte and EC interactions are not the only components that alter BBB permeability and integrity. More biorepresentatitive models of the BBB have used a substrate of appropriate stiffness to represent the natural permeability BBB.

The Matrigel substrate, which involves a co-culture of HUVECs and mesangial cells, has displayed significant biorepresentativeness. Mesangial cells, smooth muscle cells that surround blood vessels in the kindeys to regulate blood flow, are sandwiched between the HUVECs and the Matrigel substrate to eliminate contact between HUVECs and the Matrigel substrate. Interestingly, HUVECs grown directly on Matrigel substrate displays limited proliferation and monolayer or network formation. Thus, the Matrigel substrate displays acceptable network formation only when the HUVECs are co-cultured with mesangial cells.[17] Matrigel is a commonly used and commercially available basement membrane for growing several cell lines used for *in vitro* modeling. The Matrigel substrate is composed mainly of collagen, laminin, and entactin. Moreover, unlike many other commercially available substrates, Matrigel naturally contains several growth factors and small amounts of other proteins in unspecified concentrations.

Therefore, the Matrigel substrate would not be ideal for our intentions. Since *in vitro* BBB modeling requires precise knowledge of protein concentration, distribution, and expression, the Matrigel model includes variability that would interfere with our end goals.[18]

Other substrates have been shown to provide appropriate permeability properties of the BBB when coated with ECs. Mainly, gelatin-coated and hydroxyapatite-coated substrates provide an appropriate environment for EC attachment and proliferation. However, gelatin has been shown to dissolve overtime, which ultimately leads to cell detachment from the substrate. To bypass this limitation of the gelatin substrate, supplemental protein binding methods must be implemented. Hydroxyapatite-coated substrates also supports cell attachment, proliferation, and differentiation, but at a greater degree than gelatin substrates. Still, hydroxyapatite substrates dissolve overtime as well, which mandates supplementary methods to limit cell detachment.[19]

A collagen substrate is also suitable for composing *in vitro* BBB models, and is one of the more common substrates currently used. Typically, ECs are co-cultured with astrocytes. The ECs and astrocytes are then isolated and transferred onto the collagen substrate, ultimately forming a monolayer.[20] Collagen has been shown to limit BBB permeability, which ultimately augments the barrier's overall integrity. Commonly, the ECs and collagen substrate are inserted into a semi-permeable membrane, typically a Transwell insert to form the *in vitro* BBB model.[17]

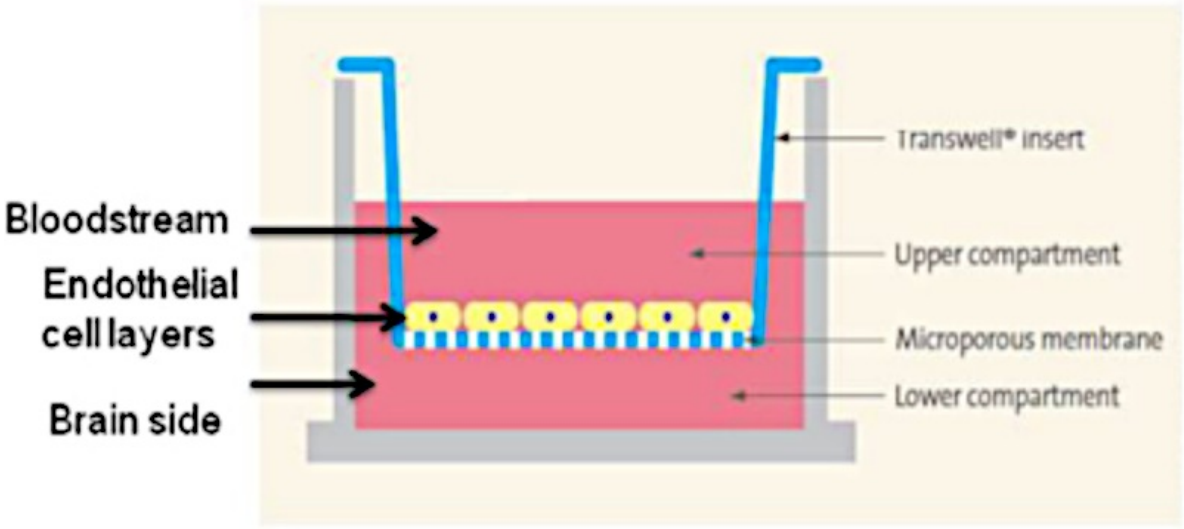

Figure 6. *In vitro* BBB model with Transwell inserts.
European Journal of Pharmaceutics and Biopharmaceutics,
http://www.sciencedirect.com/science/article/pii/S0939641110003656

Transwell inserts are also used for *in vitro* BBB modeling. Transwell inserts contain a semi-permeable filter coated with a monolayer of ECs, which is submerged in media appropriate for the type of ECs. Fibronectin is added to promote adherence of the ECs to the filter.[20]

Previously, researchers have also used fibronectin-covered polyacrylamide gels, coated with HUVEC monolayers to mimic the BBB. Interestingly, this model of the BBB involved glass coverslip as the surface for the HUVEC monolayer in place of the Transwell insert. This *in vitro* model of the BBB was also sufficient to promote transmigration of neutrophils, as would occur in the *in vivo* BBB. Moreover, this model could be exposed to TNF-α to represent various degrees of BBB pathophysiologies.[21]

2.2 Drug Delivery Mechanisms

The treatment of brain diseases requires the infiltration of the BBB.[22] We sought to develop a novel carrier and method in which to transfer drugs across the BBB. We

considered four main possibilities of drug delivery: viruses, T-cells, micelles, and solid lipid nanoparticles (SLNs). Although all methods were considered equally possible when we began our experiments, we gradually narrowed our choices down based on structure, feasibility, and results from prior experiments.

2.2.1 Viruses

The first option we chose to explore was the use of a virus as a method of drug delivery. Human immunodeficiency virus, also known as HIV, enters cells by binding to the surface of the body's cells. A protein called gp120, which is located on the surface of the virus, binds to the CD4 receptor on the surface of a healthy cell. Once bound, the cell membranes of the virus and the healthy cell fuse together.[23] This is the first step of the viral replication cycle, and there is evidence to suggest that this method of entry could serve as a drug delivery method, as shown in Figure 7 below. Although HIV was used in this example, many particles are able to gain entry into cells. In general, we will refer to these as virus-like particles (VLP).

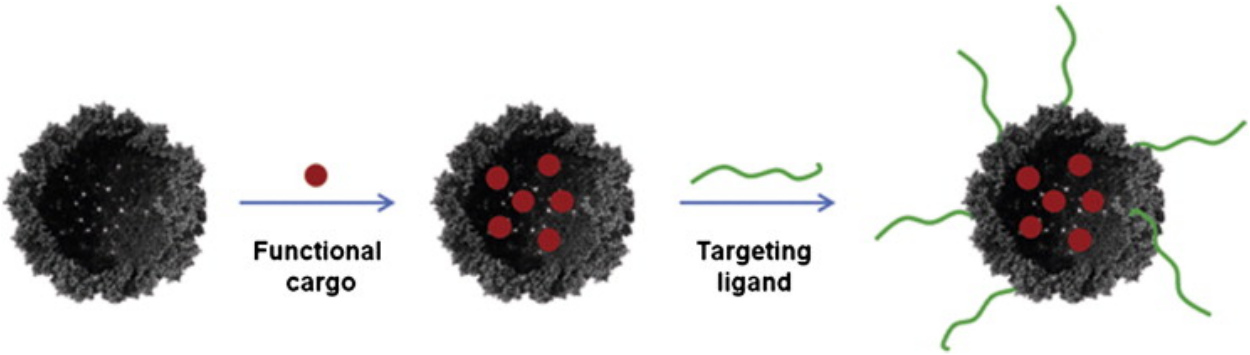

Figure 7. The virus is first introduced to its protein cargo. After full assembly, targeting ligands attach themselves to the outer shell of the virus.
Advanced Drug Delivery Reviews,
http://www.sciencedirect.com/science/article/pii/S0169409X12000087.

There are several qualities of the VLP that make them an attractive vehicle for drugs. Their ability to hold nucleic acids and small molecules means that there is a way for the drug to accompany the VLP through the cell. VLPs usually store their genetic materials within the viral capsids.[24] There are generally two methods of inserting cargo into the VLP. First, an "osmotic shock" of intact VLPs causes the spaces in between the viruses to increase. This gives enough room for nucleic acids to slip through. The second method is an *in vitro* assembly of the subunits of the VLPs with the presence of the nucleic acids.[25] There are several different viruses that have been explored thus far as drug carrying vehicles. They are: cowpea chlorotic mottle virus, the brome mosaic virus, the Simian virus, the red clover necrotic mosaic virus, the human polyomavirus JC virus, the Hibiscus chlorotic ringspot virus, and the alphaviruses.[24]

2.2.2 T-cells

The T-cell is also a potential carrier for drugs across the BBB. Research has shown that certain T-cells activated outside the CNS have the ability to migrate across a healthy BBB and into the CNS. Once there, they begin natural healing processes like inflammation, loss of barrier properties, edema formation, and demyelination. This process only holds true for active T-cells, not resting one.[26] The different stages of T-cell response once activated is shown below in Figure 8. The presence of endothelial intercellular adhesion molecule 1 (ICAM-1) and intercellular adhesion molecule 2 (ICAM-2) are both involved in the lymphocyte extravasation during the immune response.[27]

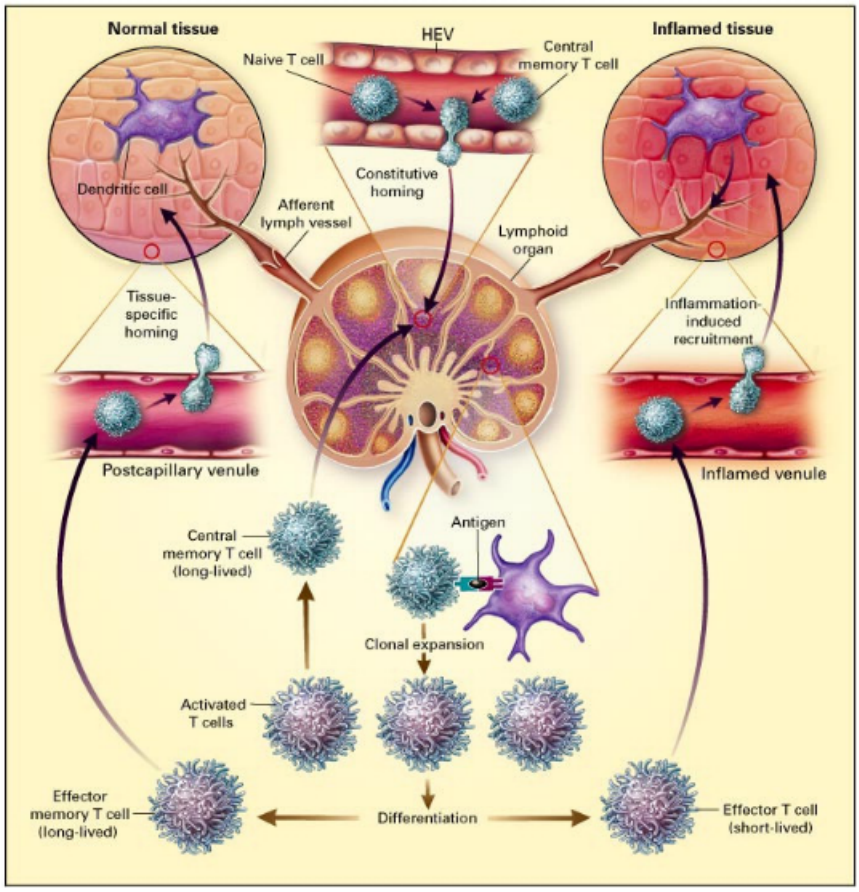

Figure 8. The stages of typical T-cell response.
The New England Journal of Medicine,
http://www.nejm.org/doi/full/10.1056/NEJM200010053431407.

2.2.3 Micelles

Another drug delivery method is the use of polymeric micelles. They typically are comprised of hydrophilic and hydrophobic monomer units. A micelle is created from an aggregate of surfactant molecules in an aqueous solution. They form a hydrophilic "head" that is in contact with the outside solution, and a hydrophobic "core". Some specific conditions must be met for the micelle to form. Factors like surfactant concentration, temperature, pH, and ionic strength contribute to the formation of the micelle. The critical micelle concentration (CMC) is the concentration of surfactants

necessary for the micelles to start forming. In addition, the critical micelle temperature must be met as well.[28] The strength of micelle drug delivery is their ability to carry drugs with poor solubility. The micelles act as a vehicle by encapsulating the low solubility drug into its hydrophobic core. The core-drug reaction is stable.[29] This allows the micelles to ferry the drug across the BBB.

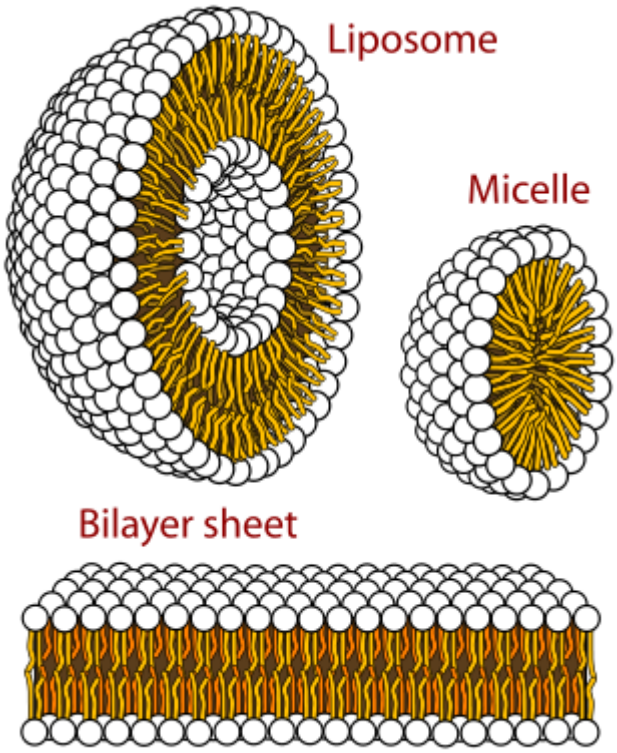

Figure 9. The cross-section view of a micelle. The drug is typically encapsulated in the middle cavities.
Progress in Molecular Biology and Translational Science,
http://www.sciencedirect.com/science/article/pii/B9780124160200000061.

2.2.4 Solid Lipid Nanoparticles

The development of genetic engineering techniques in recent times has led to an increasing number of protein complexes on the market. The extensive knowledge known about protein structure and function has furthered this growth. One of the most common

and useful methods of drug delivery include SLNs. SLNs consist of a spherical, solid, lipid core, stabilized by surfactants and ranging from sizes 1 to 1000 nm.[30] They use biological pathways to deliver their load to their target destinations.[31] This transportation includes carriage within and past the BBB. The lipids attached can range from triglycerides, diglycerides, monoglycerides, waxes, fatty acids, and steroids.[30]

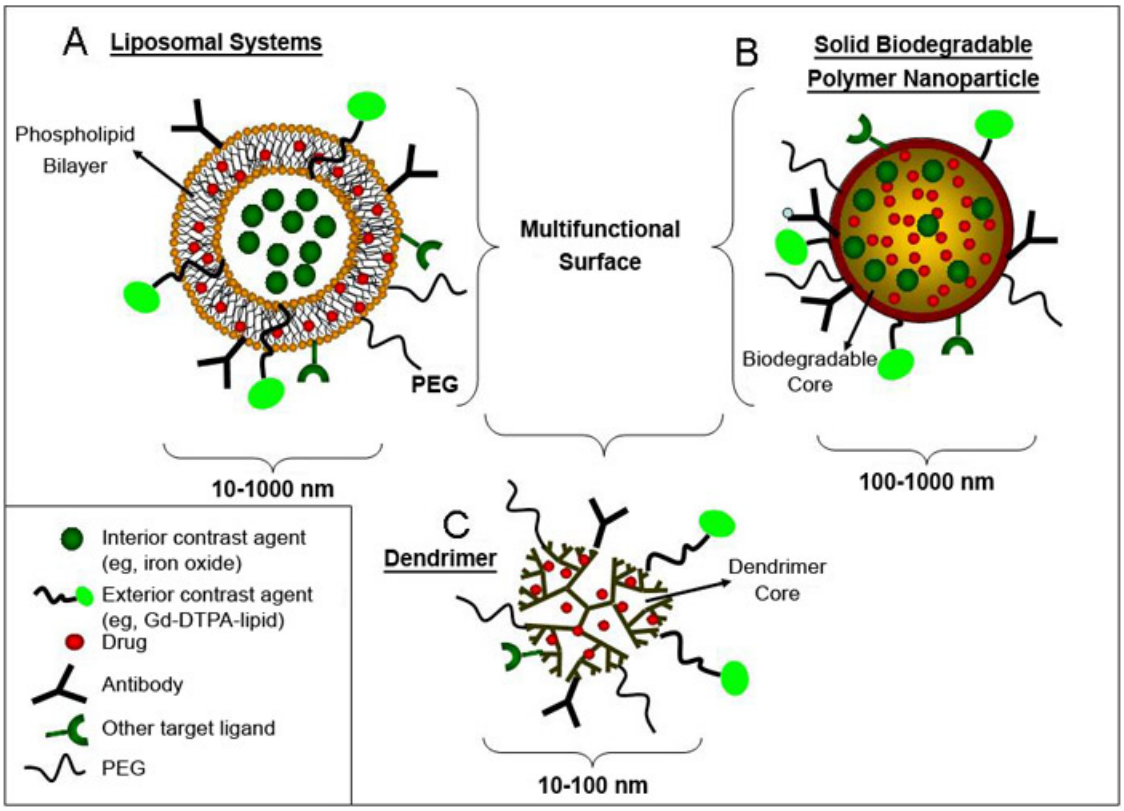

Figure 10. The structure of solid lipid nanoparticles. The phospholipid bilayer serves as a carrier for the encapsulated drugs.
The AAPS Journal, http://link.springer.com/article/10.1208%2Faapsj0902019.

SLNs also offer some unique qualities that make them preferable to other drug delivery methods. Drug stability, ability to carry lipophilic and hydrophilic drugs, possibility of controlled drug release, long-term storage, and potential large-scale production are some of the advantages. In addition, their well-known ingredients are already approved for pharmaceutical use—they are generally accepted as safe to use.[30]

Furthermore, their general flexibility and ability to be manipulated are some of the qualities that make them the strongest candidate for drug delivery. The spherical shape of the nanoparticle contributes to its general stability. SLNs can be engineered with three common hydrophobic core designs: a homogenous matrix, a drug-enriched core, or a drug-enriched surface.[31] Even within the realm of nanoparticles, some are better for drug delivery than others. For example, enhanced physical stability and decreased degradation of the drug are qualities in SLNs that aren't shared by polymeric nanoparticles.[22] SLNs also mitigate the effects of drug resistance. Drug resistance is a property of cells that impedes the efficacy of molecularly targeted and conventional chemotherapeutic agents. Specifically, P-glycoprotein prevents the accumulation of most drug delivery vessels—however, it is known that nanoparticles have the ability to accumulate without the resistance of P-glycoprotein.[32]

There are two major methods for producing SLNs, including (1) a high-pressure homogenization technique by Müller and Lucks and (2) a microemulsion technique developed by Gasco.[31] The emulsion technique involves distributing the monomer in aqueous solution, as a uniform emulsion. The surfactants cause emulsification by decreasing surface tension at the monomer-water surface. This persists until the CMC is achieved. The CMC is the concentration in which the surfactants become part of a molecular aggregate.[33] To sterilize the SLNs, stearic acid-PEG 2000 is generally accepted as the standard.[34]

SLNs have proven to be successful as a delivery method in the past.[22] For example, cationic bovine serum albumin (CBSA) has been known to enter the BBB without compromising its integrity.[35] Use of nanoparticles as a drug delivery method is

not limited to just transportation across the BBB. In a study done by Kwangjae Cho et al., drug-carrying nanoparticles were used to target cancerous tumor cells. They targeted the unique pathophysiology of tumors, some of the traits include enhanced permeability and retention effect and the tumor microenvironment.[32] In October 2003, Hiroshi Fukui and his associates conducted an experiment involving amphotericin-B and drug delivery through the liver. They used lipid nano-spheres, a small-particle lipid emulsion. The drug uptake was compared to that of using Fungizone, the traditional intravenous dosage form of amphotericin-B. The lipid nano-spheres performed favorably against the benchmark.[36] Another study favoring the continued research of SLNs as a drug delivery method was conducted by Yong Hee Yu and associates at the College of Pharmacy and Research Institute of Pharmaceutical Sciences in Seoul, South Korea. Specifically, they formed CSLNs for co-delivery of paclitaxel and siRNA to tumors in mice. 1,2-Dioleoyl-sn-glycero-3-ethylphosphocholine-based CSLN were prepared through emulsification techniques. Their research concluded that CSLNs were strong candidates for co-delivery systems of various anti-cancer drugs and therapeutic siRNAs.[37]

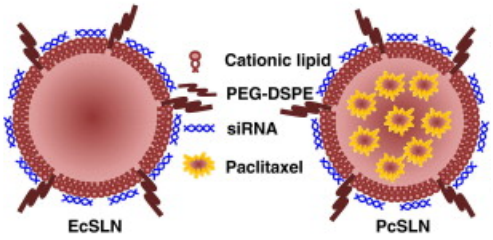

Figure 11. The structure of co-delivery of paclitaxel and siRNA, as performed by Yong Hee Yu and associates.
European Journal of Pharmaceutics and Biopharmaceutics, http://www.sciencedirect.com/science/article/pii/S0939641111003195.

A study done in January, 2012 also supported the use of SLNs as a viable form of drug delivery. In a study done by Montenegro, L. et al., an antioxidant agent Idebenone (IDE) was loaded into SLNs across an *in vivo* MDCKII-MDR1 cell monolayer, which emulates the cell interactions of the BBB. It was discovered that IDE loaded into these nanoparticles permeated the cells far more effectively than free IDE. Montenegro and his team concluded that the future of SLNs for use as a drug delivery method was "promising."[38]

Our method of drug delivery involves forming a drug delivery complex based upon the biotin-streptavidin bond. It is known as one of the strongest noncovalent bonds in nature, having a dissociation constant, K_d, in the order of 4×10^{-14} M. Because of this, it is one of the most commonly used bonds in molecular, immunological, and cellular assays.[39] The biotin-streptavidin bond is essential for the stability of our proposed drug delivery model. Without it, the CSLN and anti-VCAM-1 would attach to become a complex. The nanoparticle is essential as a vessel for the drug, and the anti-VCAM-1 provides a targeting system for our vehicle.

2.3 Targeting Molecules

Among the many molecules on the surface of the BBB, cell surface adhesion molecules exist to bind other cells to the BBB surface.[40,41] Because the BBB has low permeability and high resistance for the brain's protection, the cell surface adhesion molecules on the BBB are highly specialized and selective in which molecules they bind to.[40,42] They are transmembrane proteins that have an intracellular domain for cytoskeleton interaction, a transmembrane domain, and an extracellular domain for

binding of other molecules.[43] Their placement on the BBB is indicated below in Figure 12.

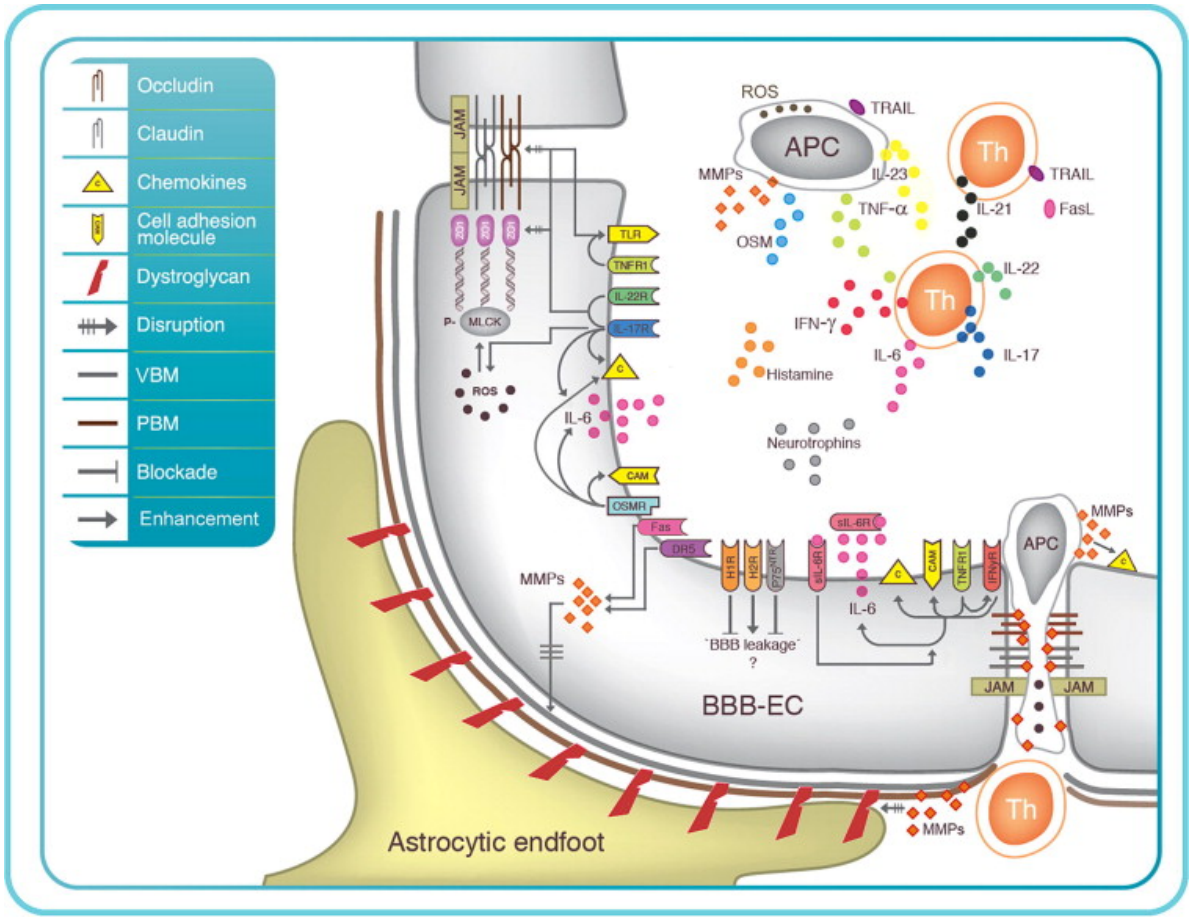

Figure 12. Cell surface adhesion molecules indicated by yellow arrows on BBB diagram. Febs Letters, http://www.sciencedirect.com/science/article/pii/S001457931100336X.

In addition to binding to extracellular molecules, most cell surface adhesion molecules allow for the migration of the molecules (i.e. nutrients, immune cells, and various communicative molecules) through the BBB.[43,44] Thus, cell surface adhesion molecules are valuable as targets for the delivery of drugs specifically through the BBB.[45] In diseased states, the vascular endothelium of the BBB plays a large role in the process of inflammation.[45] ICAMs are surface adhesion molecules in the endothelium and have an essential role in inflammation processes.[43] ICAM-1, in particular, is up-regulated by

TNF-α, a molecule that induces inflammation of the BBB.[46] Thus, when there is inflammation, there is an increase in ICAM-1 because they facilitate the transmigration of leukocytes to reduce the inflammation.[27,43]

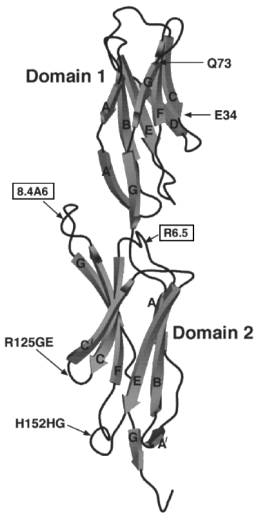

Figure 13. The three dimensional protein structure of ICAM-1.
Biochemical Journal, http://www.biochemj.org/bj/351/0079/bj3510079.htm.

VCAM-1 is also a cell adhesion molecule that acts similarly to ICAM-1.[47-49] VCAM-1 is a transmembrane glycoprotein that has the ability to internalize and transmigrate other molecules through the endothelial layer of the BBB once the molecules are bound to it.[45,50] VCAM-1 is similar to ICAM-1 in that it is up-regulated by TNF-α and the molecule itself is not a health risk for humans regardless of the concentration levels in blood plasma.[51,52] VCAM-1 specifically has been known to enhance the adhesion of monocytes, a critical player in the immune system, to the ECs that it is expressed in, further confirming that it is involved in recovering diseased organ states.[53] In order to adhere to uptake molecules such as monocytes, the internalized molecule must have a specific, complementary antibody that matches VCAM-1.[54,55] Thus, anti-VCAM-1 has been proven to be the perfect complementary antibody to VCAM-1 on the BBB.[54,56] The vehicle and anti-VCAM-1 complex results in becoming a

great means of drug delivery specific to the increased amount of present VCAM-1 in diseased states of the BBB.[54,57] Since using ICAM-1 has been well observed as a targeting method, we decided to use VCAM-1 as our cell adhesion molecule to better understand its role in BBB transmigration.

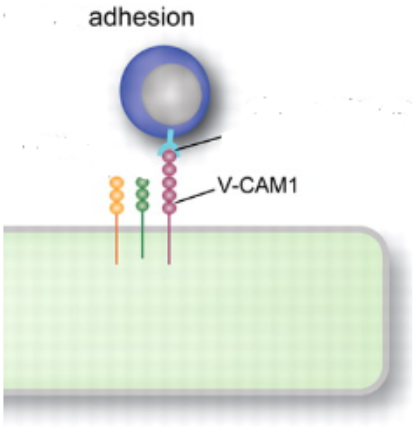

Figure 14. VCAM-1 on the BBB surface adhering to a molecule. Neurology, http://www.neurology.org/content/78/16/1268/F2.large.jpg.

3. Blood Brain Barrier

3.1 BBB Background

3.1.1 BBB Architecture

The BBB is the membranous, physical separation of the circulatory system from the CNS in an organism. Specifically, cerebrovascular ECs lining the thin capillaries separate the blood and brain interstitial fluid (ISF), the choroid plexus structure that produces cerebrospinal fluid (CSF), and the protective meningeal arachnoid epithelium of the spinal cord.[58,59] Closely associated with the ECs of the BBB are astrocytes, pericytes, and the extracellular matrix, specifically the basal lamina.[6,58,60] The several cell types associated together compose structured NVUs, which are involved in the regulation of blood to and from the brain, as shown in Figure 15 below.[3,58,61]

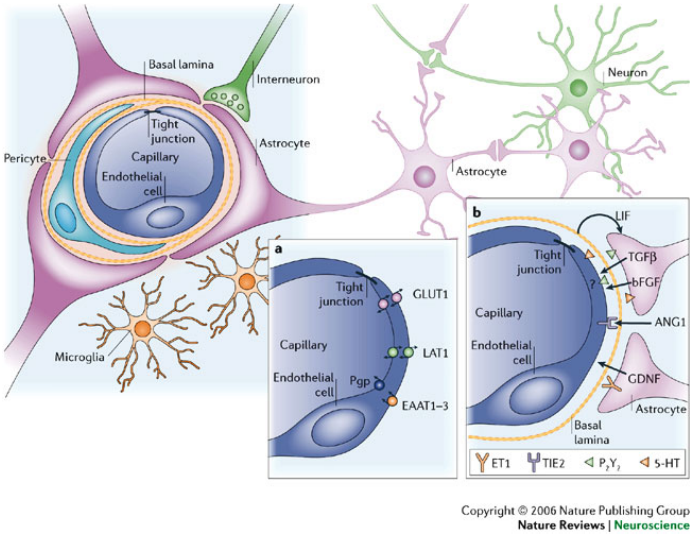

Figure 15. Architecture of the BBB. The interactions between brain endothelial cells, astrocytes, pericytes, the basal lamina, and microglia create the neurovascular units. Nature Reviews Neuroscience, http://www.nature.com/nrn/journal/v7/n1/fig_tab/nrn1824_F2.html

The surface area of these NVUs in the brain is large (nearly $20m^2$ per 1.3kg of brain), but the tight association between the cells allows the BBB endothelium to highly regulate the microenvironment.[58] A distinct feature of the BBB is the lack of leakage and restrictive permeability both to and from the brain. This restrictive membrane between the brain and blood was initially conceived from experiments in the late 19th and first half of the 20th century.[62] There appeared to be an apparent barrier that would prevent the transport of solutes to the brain ISF. The capillary endothelium was thought to be a contributing factor to this selective permeability.[62] Acidic and basic dyes were injected into the bloodstream of a patient, and observations showed a lack of penetration into brain tissue. Additional studies showed that this was not due to lack of uptake by individual neurons, but instead due to a physical barrier that separated the peripheral circulation from central circulation.[3,59] The dyes, when in circulation, bound to albumin proteins, and these proteins were unable to traverse the barrier separating the blood and the brain. Peripheral vessels in other parts of the body were found to be permeable to many types of solutes, including water-soluble compounds, through the presence of pores within the endothelium membrane. Horseradish peroxidase was used as an enzymatic tracer to localize these pores in different types of endothelium (skeletal, cardiac, and cerebral). The metabolized product accumulated greatly, creating an opaque center of activity upon visualization.[62] The peroxidase product appeared to be unable to pass through to the brain interstitium, and instead accumulated within the intercellular spaces.[62] The peroxidase product appeared within the brain fluid only when injected directly into the interstitium. Direct injection of dyes in the CSF showed clear staining, and additional quantitative experiments confirmed the existence of a physical barrier.

There are distinct differences between brain ECs and other ECs found in an organism: cerebrovascular cells have 1) fewer fenestrations (pore-like openings) between ECs, allowing for less diffusion, 2) more TJ proteins, 3) less pinocytic vesicular transport and hydrophilic compound diffusion, and 4) a higher number of mitochondria associated with strong metabolic activity.[3,6,61]

The main contributors to the strong regulation of substances across the membrane are TJs. TJs are proteins linking the cytoskeletons of adjacent ECs and that exclude many, if not most, substances in the blood from reaching the brain, and establish the barrier properties of the BBB.[6,60] TJs contain six subunits and appear as fusions of the plasma membrane of adjacent ECs.[6,60] Many regulatory signaling pathways exist, which include G-proteins, serine-, threonine-, and tyrosine-kinases, cAMP, and others.[60] TJs are primarily composed of three integral membrane proteins, specifically occludin, claudin, and JAMs.

Occludin was initially identified through freeze fracture microscopy in chickens and mammals.[6] Occludin proteins highlight a molecular difference between brain and other ECs, in that occludin expression is greater in brain ECs. Specifically, the cytoplasmic side of the occludin is heavily phosphorylated in TJs, and acts as a regulatory protein to affect membrane permeability.[6,58,60,61] Claudins are another family of proteins within TJs that affect membrane permeability. Specifically, claudin-1 and claudin-5 have been isolated in cerebrovascular endothelial cell tight junctions, and current speculation indicates claudin-12 to have some contribution.[58, 60] Claudins associate with occludins to form and maintain TJ integrity.[58] JAMs are also proteins present within TJs, have a single transmembrane domain, and serve to form and maintain

TJ structure.[6] There are several types of JAMs that are found in specific cell types: JAM-1 is found in endothelial and epithelial cells; JAM-2 and JAM-3 are found in mainly endothelial and not epithelial cells.[60] JAMs serve to regulate interactions at the TJ area. In addition to the three main protein families described above, there are other accessory proteins that compose TJs, such as zonula occludin proteins that face the cytoplasmic side. Another important molecule, while not considered to be one of the three primary integral TJ proteins, is the protein β-catenin. In the context of the BBB, it anchors the cytoskeleton of adjacent ECs to strengthen their junctions and decrease permeability, and also plays a role in signaling cascades that lead to angiogenesis during BBB formation as well as maintenance of the mature BBB.[63,64]

3.1.2 BBB Differentiation

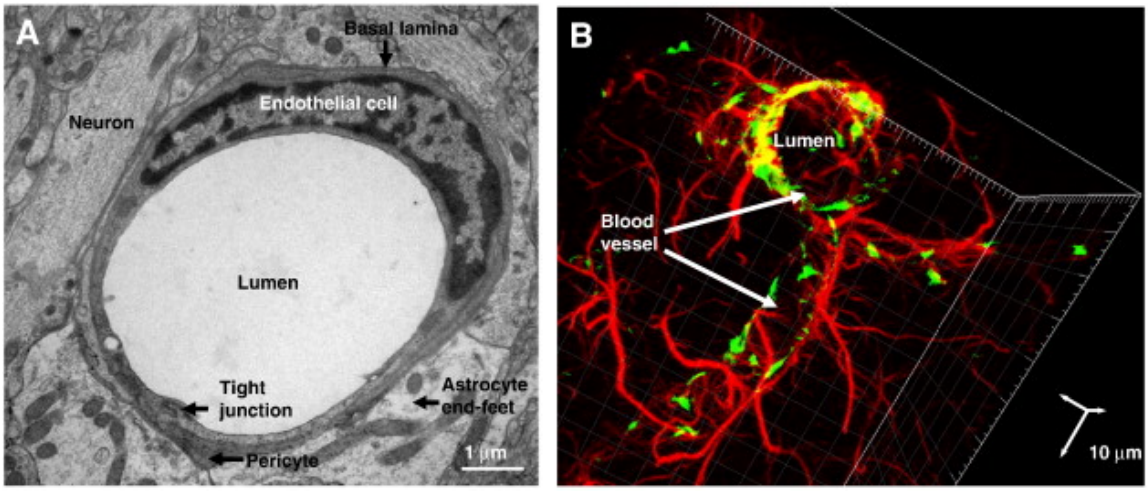

Figure 16. *In vivo* imaging of a neurovascular unit (NVU). A) Electron microscopy image of a NVU. B) Confocal microscopy of a rat brain NVU, with green fluorescence marking endothelial cells, and red fluorescence indicating astrocytes.
Science Direct, http://www.sciencedirect.com/science/article/pii/S0005273608003489

BBB selective permeability characteristics, such as the presence of TJs, are inherent to the ECs, but the differentiation of the membrane barrier is linked to the

remaining components of the NVU: astrocytes, pericytes, and the basal lamina, shown below in Figure 17. The close associations between individual components allows for induction of new cell growth during both during development and after maturity, for maintenance purposes. While the traditional and most researched relationship is the induction of the growth of ECs by astrocytes, pericytes, and the basal lamina, studies have shown that the ECs themselves can, in turn, induce the growth of these cells, in particular astrocytes.[58] There is a constant "cross-talk" within the NVU that allows for BBB growth induction and function.[3]

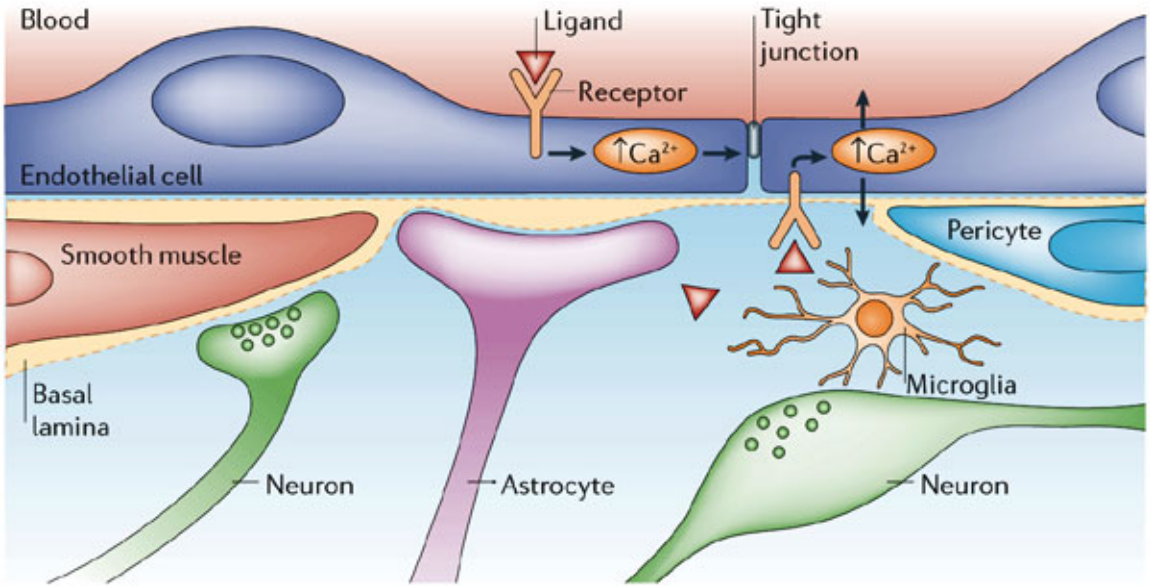

Figure 17. Composition of the differentiated BBB on a cellular level. Not the multiple cell types involved in the creation of the BBB.
Nature Reviews Neuroscience,
http://www.nature.com/nrn/journal/v7/n1/fig_tab/nrn1824_F5.html

Astrocytes are considered to be the major contributor to BBB differentiation, as their ends are associated directly with the cerebrovascular ECs.[65] Astrocytes descend

from the ependymoglia of the neural tube, and are polarized cells whose ends are directly associated with the cerebroendothelial cells. Astrocytes secrete several substances, including transforming growth factor-β (TGF-β), glial-derived neurotrophic factor (GDNF), fibroblast growth factor (FGF), and angiopoietin-1 (ANG-1)[58]. TGF-β and GDNF have been found to mature the BBB postnatally.[6] These several factors can induce BBB differentiation *in vivo,* including the formation of TJs.[60] Studies have shown that the implantation of cultured astrocytes into areas with a leaky endothelium induced tightening of the endothelium.[6] Co-culture of brain ECs with astrocytes has also shown the inductive effects of the latter, with BBB properties illustrated in culture.[61] Astrocytes maintain and up-regulate existing BBB features, such as expression of transport proteins and presence of enzyme systems.[58] One particular study injected astrocytes into the eye chamber of adult rats, and within 48 hours, those cells became vascularized. Dyes were injected into the same chamber, and aggregates of cells that were not associated with astrocytes were highly stained with the dye, but aggregates of cells that were associated with the astrocytes were not stained. The ECs that formed capillaries had functioning TJs, while others were much more leaky.[65]

Pericytes are embedded within the basal lamina that is adjacent to the ECs. Pericytes wrap around the ECs to provide structural support, assist in vasoregulation, restrict permeability, and assist in the differentiation of the ECs and TJs.[6,58,61] Pericytes are the least studied component of the NVU, but research has shown that these cells assist in BBB function *in vivo* by regulating BBB-specific gene expression patterns and by inducing polarization in the ends of astrocytes that surround the blood vessels in the

CNS.[61,66] While more is to be discovered and understood, it is clear that pericytes play a direct role in the stability of the BBB.

The basal lamina is a complex network of consisting of collagens, including laminin, fibronectin, enactin, thrombospondin, and proteoglycans.[60,61] There are three main layers, one produced by the ECs, one produced by the astrocytes, and one in which both cell types contribute. It works in tandem with the other components of the NVU to maintain BBB properties and function, specifically BBB integrity.[61] Specifically, the basal lamina contains agrin, a heparin sulfate proteoglycan, which accumulates during initial BBB formation, and works to sustain BBB integrity.[58]

3.1.3 BBB Permeability

The ISF within the brain has a different ion concentration from the rest of the body, and this ion concentration is independently maintained through BBB mechanisms.[13] The BBB produces a physical barrier primarily through the presence of restrictive TJs between ECs, which forces molecules to take a transcellular route.[58] Small gaseous molecules such as O_2 and CO_2 can diffuse freely through lipid membranes, as well as small lipophilic molecules, but the remaining polar (and semi-lipophilic) and large compounds are generally impermeable. [6,58] The BBB additionally produces a metabolic barrier through intracellular and extracellular enzymes, which include peptidases, nucleotidases, monoamine oxidases that are used to metabolize substrates. This property of the barrier can breakdown or inactivate many compounds and toxins.[58]

The main methods of BBB transversal are receptor-mediated entry and adsorptive-mediated transcytosis. Insulin and transferrin use receptor-mediated

transcytosis to cross the BBB, and glucose uses the GLUT-1 insulin independent carrier. Adsorptive-mediated transcytosis, which requires the interaction of the ligand to membrane surface charges before internalization, is most frequently utilized by cationic molecules.[58,67,68] Amino acids, nucleobases, and nucleosides use their own individual, specific carriers.[58,61] The large family of solute carrier transporters (SLC) contributes to many transport mechanisms.[61] Immune cells, such as leukocytes, traverse the BBB through adhesion molecules, such as ICAM-1, VCAM-1, PECAM-1, and CD44.[6,61]

TEER has additionally been associated with the selective permeability of the BBB. In general, a higher TEER value (measured in Ohms) is associated with a low paracellular permeability, and therefore a tighter and more selective membrane.[69] Researchers have measured the TEER values in developing rats through the use of lanthanum (a chemical element) and electron microscopy. The resistance was measured in pial vessels in fetal rats between 17 and 21 days of gestation, in 1 to 10 day neonates, and 28 to 33 day old rats.[13] There was a significant increase in TEER from 20 to 21 days gestation (323Ω to 1128Ω), with no significant increase after that period. Lanthanum appeared to accumulate on the apical side of TJs, and did not appear to traverse to the brain interstitium, as the mature and functioning BBB does not allow the passage of this element to the brain.[13] Pathological conditions were also observed to illustrate the importance of high TEER values to maintain a homeostatic environment. During hyperosmotic shock, when there is a significant increase in permeability, TEER values measured were significantly lowered. Similar conclusions were made with *in vitro* monolayers of ECs, with higher TEER values associated with tighter and more confluent monolayers.[70] Many studies have been performed to better understand the effects of

particular molecules, such as malathion, malaoxon, cAMP, and vasoactive agonists on the TEER values of *in vitro* BBBs.[71,72] High TEER values *in vitro* also occurred in BBB models that were associated with cultured astrocytes.[6]

3.1.4 BBB Pathology

Neural diseases have a variety of implications for the integrity of the BBB. Generally, there tends to be a change in permeability of the membrane that causes drastic movement of substances. Physiological manifestations are inflammation, edema, and breakdown of tissue.[6,58,61] While neural diseases may affect the integrity of the BBB, loss of healthy BBB function may conversely result in the worsening or development of neurological diseases. These include acute and chronic cerebral ischemia, multiple sclerosis, brain tumors, and Alzheimer's disease.[73] An important reason for the BBB dysfunction or breakdown is due to malfunctioning TJs between ECs, which allow passage of molecules within the gaps between ECs.[58] Claudins within the TJs are lost or down-regulated in diseased states, leading to the breakdown of TJs.[6]

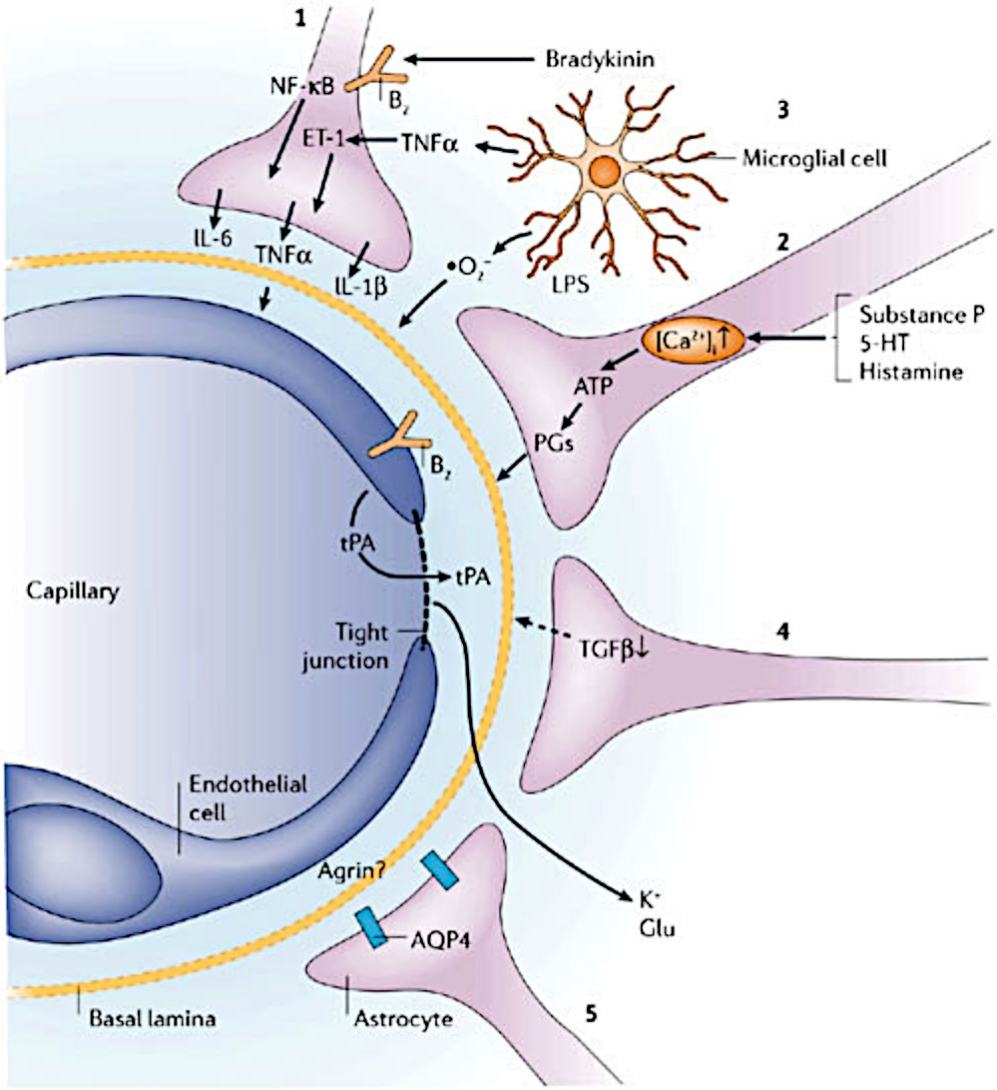

Figure 18. Various cytokines associated with pathological conditions and the BBB. Histamine and TNF-α, among other inflammatory signals, are released during inflammation of the BBB.
Nature Reviews Neuroscience,
http://www.nature.com/nrn/journal/v7/n1/fig_tab/nrn1824_F6.html

Other chemical mediators released during neural diseased states alter BBB structure and permeability. Histamine, a major inflammatory chemical, allows for the passage of antibodies into the brain.[58] Histamine can be released in conjunction with

TNF-α, interferon γ, nitric oxide, and several other mediators, which also act to decrease BBB permeability, as shown in Figure 18.[6,58,61] TNF-α has also shown to rearrange the cytoskeleton of the cell through its cytokine effects.[3] The BBB tries to counteract permeability changes with the support of the components of the NVU, especially astrocytes and other microglia, by limiting TJ protein destruction.[6] However, this support is at the early stages, and is overpowered as diseases progress.

Changes in the BBB and associated components of the NVU depend upon the specific disease. In Alzheimer's, the accumulation of amyloid-β proteins is initially observed in the blood vessels, and this accumulation causes the degradation or impairment of adjacent astrocytes and ECs of the NVU.[58] Additionally, the loss of agrin from the basal lamina adjacent to ECs can cause BBB damage and weakness.[58] This physiological symptom preceded other clinical symptoms of neurological decline in Alzheimer's animal models. Cascades of cellular events are signaled, which exacerbates the ongoing damage, specifically affecting neuronal integrity and synaptic function.[6,61] Alzheimer's, HIV, and multiple sclerosis become progressively worse after BBB dysfunction due to the infiltration of immune cells into the brain, which additionally triggers inflammatory effects through cellular cascades. TJ proteins are degraded further.[6] In certain cancers, such as gliomas and adenocarcinomas, TJs begin to open, which leads to similar brain infiltration.[6] Cytokines were also elevated in animal models after local and global ischemia, and in stroke, which can also enhance ischemic injury. [6,61] Bacterial infections also enhance cytokine production and other inflammatory mediators to increase BBB permeability.[61]

The relationship between disease onset, disease progression, and BBB changes is very complex, yet its understanding and exploitation is crucial to developing safe and successful treatment modalities. There have been numerous explorations into drug-delivery devices, but of particular interest are those that directly target the BBB endothelium.

3.1.5 BBB Targeting

BBB damage often precedes the major physiological consequences of disease, which is why it is becoming a prominent area of research in relation to a drug-delivery target.[58] Through early targeting and treatment of the BBB, it may be possible to reduce the progression of a disease or the severity of symptoms. There are additional hopes for a prophylactic treatment of the BBB to delay the onset of a disease.[58] During diseased states, the release of cytokines causes the up-regulation of numerous cellular adhesion molecules and receptors on the BBB through a cascade of signaling. The entry of leukocytes and other immune cells into the BBB is a multi-step process: there is the initial immediate contact of the immune cell to the BBB membrane, followed by the cessation of rolling across the surface, followed by adhesion to the membrane through receptor binding, and then finally passage through the membrane to the brain.[3] Leukocytes gain entry to the brain by binding to adhesion molecules on the endothelium, specifically ICAM-1, VCAM-1, E-selectin, and recently-identified activated leukocyte cell adhesion molecule (ALCAM).[61] It is thought that cell adhesion molecules work together with one another to increase leukocyte transmission into the brain to fight infections.[61] ICAM-1 is particular for both leukocytes and lymphocytes, and is both a

passive adhesion site and traversal site for immune cells through the activation of cellular cascades.[60] Because of its up-regulation in the BBB endothelium during diseased states, it has been investigated as a potential target for novel treatment models.[41,74,75] VCAM-1 is typically expressed in minute quantities, in the vascular endothelium. When cytokines cause the up-regulation of VCAM-1 expression, lymphocytes, monocytes, eosinophils, and basophils are able to adhere and interact with normal and diseased vasculature states. For example, up-regulation of VCAM-1 has been shown to play a role in the development of atherosclerosis, as well as other inflammatory diseases such as multiple sclerosis.[76,77]

As discussed in the literature review section above, there have been various targeting methods investigated in the past. This project aims to use the natural up-regulation of VCAM-1 expression on the BBB endothelial membrane during diseased states as the target of a CSLN drug delivery complex.

3.1.6 Project Aims

While the overall aim of this project is to develop a novel drug delivery complex to traverse an *in vitro* BBB model, this section of the project is focused on the development and characterization of the BBB model. The methodology below will discuss cell culture methods and techniques, model formation, proof of model formation through staining of TJ proteins, characterization of VCAM-1 expression as TNF-α concentration varies, and lastly, quantification of fluorescent bead migration through the BBB model.

3.2 BBB Methodology

3.2.1 Human Brain Microvascular Endothelial Cell Culture

The primary HBMECs were purchased from Applied Cell Biology Research Institute (ACBRI 376). The HBMEC medium was made using the following reagents: Roswell Park Memorial Institute (RPMI) media, fetal bovine serum (FBS), L-glutamine, EC growth supplement (ECGS), heparin, and penicillin/streptomycin. The RPMI media was stored at 4^{o}C and the other supplements and antibiotics were stored at -20^{o}C. In order to make one batch of medium with a final volume of 500 mL, 370 mL of RPMI media was used. One hundred mL of 100% FBS was used, yielding a final concentration of 20% FBS. 5 mL of a stock solution of 200 mM L-glutamine was added, making the final concentration 2 mM L-glutamine. 15 mL of 1 mg/mL ECGS was used in order to give a final concentration of 30 µg/mL ECGS. 5 mL of 10 mg/mL heparin was added to the solution, giving a final concentration of 100 µg/mL heparin. Finally, 5 mL of the penicillin/streptomycin stock solution (10,000 U/mL and 10 mg/mL respectively), yielding a final concentration of 100 U/mL penicillin and 100 µg/mL streptomycin. This is summarized in Table 1. Once the HBMEC medium was made, it was stored at 4^{o}C.

	Stock	Final (in 500 mL)	Volume to make 500 mL
RPMI Media			370 mL
FBS	100%	20%	100 mL
Endothelial Cell Growth Supplement (ECGS)	1 mg/mL	30 µg/mL	15 mL
Heparin	10 mg/mL	100 µg/mL	5 mL
Penicillin/streptomycin	10,000 U/mL (pen) 10 mg/mL (strep)	100 U/mL (pen) 100 µg/mL (strep)	5 mL

Table 1. Recipe for HBMEC Media

The media for the HUVECs was made according to Table 2. The basal medium was stored at 4^{o}C and the supplements and penicillin/streptomycin were stored at -20^{o}C. After the media was prepared it was stored at 4^{o}C. HUVEC media was used within 2-3 weeks after it was made. The volumes of the reagents were adjusted if more or less media needed to be made so that reagents were not wasted.

	Final (in 500 mL)
Basal Media	461 mL
EnGS	1 mL
Rh EGF	500 µl
Ascorbic Acid	500 µl
Hydrocortisone Hemisuccinate	500 µl
Heparin Sulfate	500 µl
FBS	10 mL
L-glutamine	25 mL
Penicillin/ Streptomycin	1 mL

Table 2. Recipe for HUVEC media.

3.2.2 Procedure for Changing Media

The media was placed in the 37°C water bath for 30 minutes until it was warm. In the cell culture hood, the media in the flask containing the cells was aspirated out using a glass pipette. 5 mL of fresh HBMEC media was added to a T-25 flask, or 10 mL for a T-75 flask. The media was changed every other day during the week. Every Monday and Wednesday, 5 mL of media was added to a T-25 and 7 mL of media was added on Friday to account for the weekend. For the T-75 flasks, 10 mL of media was added every Monday and 12 mL of media was added on Friday. After fresh media was added, the flask containing the cells was placed back in the incubator. The cells were

grown in a humidified incubator at 37°C and 5% CO_2. The same procedure was used to change the media for HUVECs. The HUVECs were also grown under the same incubator conditions.

3.2.3 Procedure for Splitting Confluent Cells

The following reagents were used for the cell splitting procedure: 0.01 M phosphate buffered saline (PBS) (pH ~7.1), 0.05% Trypsin-EDTA, and HBMEC media. These solutions were warmed in the 37°C water bath before they were used. The media in the flask containing confluent cells was aspirated out using a glass pipette. The cells in the flask were washed by adding 5 mL of PBS and tilting the flask around. The PBS was aspirated off after 10 seconds. The cells were detached from the wall of the flask by adding 750 µl of trypsin-EDTA. The flask was tilted around to expose the cells and then incubated at 37°C for 2 minutes. The flask was observed under a light microscope to ensure that the cells were spherical in shape and floating in the liquid. The trypsin was diluted by adding 5 mL of media to the flask. The solution was then transferred to a 15 mL conical tube and centrifuged for 5 minutes at 5°C and 150x g. The supernatant was removed, leaving a small amount of media and the cell pellet at the bottom of the tube. The pellet was re-suspended in 5 mL of media by pipetting up and down until no clumps of cells remained. The cells were counted by adding 10 µl of the cell-media solution to a hemacytometer. The number of cells were counted in each corner grid and then averaged. This number was multiplied by 10^4 to give the concentration in cells/mL. A fresh flask was filled with 5 mL of media. The number of cells added to the new flask depended on how fast the cells were needed to be confluent, as seen in Table 3. The volumes of

solutions used in this procedure were for a T-25 flask. If a T-75 flask is used, double all volumes in the protocol. This procedure was used for splitting both HBMECs and HUVECs.

	T-75	**T-25**
Confluent	6.0E+06	3.0E+06
1 Day	3.0E+06	1.5E+06
2 Days	1.5E+06	7.5E+05
3 Days	7.5E+05	3.8E+05
4 Days	3.8E+05	1.9E+05
5 Days	1.9E+05	9.4E+04
Do not place less than	1.0E+05	5.0E+04

Table 3. Confluency Table. The number of cells to add to the flask based on when confluency is desired

3.2.4 Thawing HBMECs

5 mL of media was added to a T-25 flask. The flask was placed in the incubator for 30 minutes to warm up the media. To start a new line of HBMECs, a vial of cells was removed from the liquid nitrogen tank and placed in the 37^{o}C degree water bath. The vial was thawed for 1-2 minutes. When the cells were completely thawed, the entire 1 mL contents of the vial were added to the flask with the warmed media. The flask was placed in the incubator and the media was changed after 24 hours to remove any unattached cells. From this point, the cells were maintained with normal cell culture techniques. The HBMECs were used through passage 9, but not past passage 12.

3.2.5 Making the BBB Model: Monolayer of Cells on Glass Coverslips

Fibronectin was added to a 22 x 22 mm coverslip for the cells to attach to the surface of the glass coverslip. The coverslips were washed with PBS. A coverslip was added to each well of a 6-well plate. The dish was put under the UV for 1-2 hours. A 300 µl fibronectin solution (100 µg/mL) was added to each coverslip. The solution was made using 270 µl 1X PBS and 30 µl 1 mg/mL fibronectin. The 6-well plate was tilted to spread the solution evenly across the coverslip and left in the hood for 2 hours. After 2 hours the cells were split on to the coverslip. In order to make a monolayer of cells in 2-3 days, $4x10^5$ cells were split onto each coverslip.

3.2.6 Adding TNF-α

TNF-α is a cytokine that induces the inflammatory response in cells. It was added in varying concentrations to the monolayer of cells to simulate different diseased states. As the concentration of TNF-α increased, the cells simulated a more diseased state, therefore there we expected to observe an up-regulation of VCAM-1. The TNF-α was added to the monolayer of cells 18 hours prior to experiments that were conducted. The following concentrations were used for all experiments: 0 mg/mL, 2 mg/mL, and 20 mg/mL. 6 coverslips total were used for every experiment with 2 coverslips per concentration. Once the TNF-α was added, the monolayers of cells were placed back into the incubator until experiments were conducted 18 hours later.

3.2.7 Immunofluorescent Staining for VCAM-1

The cells incubated in TNF-α for 18 hours were fixed in order to stop them from growing. They were fixed in 2 mL of 2% paraformaldehyde for 20 minutes. The fixation step was done in the dark since paraformaldehyde is light sensitive. The cells were washed twice in 2 mL of PBS of for 5 minutes on a rocker to ensure uniform distribution of the PBS. After the washes, 2 mL of 2% BSA in PBS were added to each well to block nonspecific binding. The cells were blocked in the 2% BSA for 2 hours at room temperature. The blocking buffer was removed and 200 µl of primary anti-rabbit VCAM-1 antibody was added to each coverslip. The final concentration of the primary antibody was 10 µg/mL. The cells were incubated in primary antibody for 1 hour. After an hour, the cells were washed with PBS twice for 5 minutes each. The cells were blocked again with 2% BSA in PBS for an hour. The blocking buffer was removed and 200 µl of secondary goat anti-rabbit antibody was added to each coverslip. The final concentration of the secondary antibody was 5 µg/mL. The cells were incubated in secondary antibody for 1 hour. After an hour, the cells were washed with PBS twice for 5 minutes each. The nucleus was then stained with a Hoechst stain. 200 µl of the Hoechst stain diluted to 2 µg/mL was added to each coverslip for 20 minutes. After an hour, the cells were washed with PBS twice for 5 minutes each. The cells were then viewed under the microscope to take images. The cells were viewed under light using a DIC filter. To view the stained nucleus, the cells were viewed using the DAPI filter. The VCAM-1 was viewed under the TRIT-C filter.

3.2.8 Bead Experiments

Fluorescent microspheres (or beads) from Invitrogen were used as controls to test whether or not any materials could get through the BBB. These beads are polystyrene microspheres that have been modified with carboxylates on their surface. The fluorescent dyes added have been stated to have negligible effects on the properties and interactions of these beads. The purpose of using the fluorescent microspheres was to ensure that the nanoparticle complex that was synthesized would be able to be tested on the model. First, the microspheres alone were tested on monolayers of cells that had been incubated with different concentrations of TNF-α for 18 hours as mentioned in Section 3.2.6. 25 µl of fluorescent microspheres were added to the cells. After an hour, the microspheres were washed off of 1 set of cells (0 µg/mL, 2 µg/mL, and 20 µg/mL TNF-α) and were imaged under the microscope. Images using phase microscopy were taken at an exposure of 100 milliseconds. Images of the fluorescent microspheres were taken using the TRIT-C filter at an exposure of 10 milliseconds. The microspheres were washed off the other set of cells after 5 hours and were imaged under the same conditions.

This experiment was also repeated but VCAM-1 antibody was added to the HUVECs to block VCAM-1 receptors on the surface of the cells. The primary VCAM-1 antibody was added to monolayers of cells that were in 2 mL of media. The cells had been incubated with TNF-α for 18 hours prior to starting the experiment. The antibody was diluted in 2% BSA, giving a final concentration of 5 µg/ml. An hour after the cells were incubated, they were washed with HUVEC media. Then 25 µL of the fluorescent microspheres were added to each monolayer of HUVECs. After an hour, the

microspheres were washed off of one set of cells (0 μg/mL, 2 μg/mL, and 20 μg/mL TNF-α) and were imaged under the microscope. Images using phase microscopy were taken, with an exposure of 100 milliseconds and images of the fluorescent microspheres were taken using the TRIT-C filter with an exposure of 10 ms. The microspheres were washed off the other set of cells after 5 hours and were imaged under the same conditions.

Images were analyzed using the ImageJ processing program developed by the National Institute of Health (NIH). Both phase microscopy and fluorescence images were analyzed to count the concentration of fluorescence in the different staining and bead experiments. The data was then normalized if possible to counter the varying levels of noise in the background of images.

3.2.9 Imaging Techniques

Images were analyzed using the ImageJ processing program developed by the NIH as well as MATLAB developed by Mathworks. Fluorescence images were analyzed to quantify the concentration of fluorescence in the different staining and bead experiments. This was achieved in two ways. For single images, ImageJ's histogram feature was used to observe distribution and mean fluorescent intensities. ImageJ was also used for the cell counter tool when nucleus stains were available. When multiple images were averaged to create a histogram and/or when a modified histogram was needed, images were imported into MATLAB. The data was then normalized if possible to counter the varying levels of noise in the background of images.

ImageJ's histogram feature was the most basic way to quantify fluorescence. For a single image, it gives both a mean fluorescent intensity of the image as well as quantitative and visual representations of the intensity distribution. The histogram tool is found under the "Analyze" menu. One of the benefits of using the histogram tool is that it gives lots of quantitative information about the image. An important piece is Minimum Value; as the minimum value is representative of background noise in the image, sometimes it is valuable to subtract the background using ImageJ's subtract function (under "Process" →"Math" → "Subtract…") so that all images are on equal footing. This is one form of normalization available. The other form is normalizing to the number of cells in the sample. When nucleus stains are present, ImageJ's Cell Counter (as seen below) is used. It can be found under "Plugins"→"Analyze"→"Cell Counter."

In MATLAB, the histogram functionality was available through the use of the "histc" function. The function takes a vector and returns the frequency of values in the vector. To determine the frequency across multiple samples, images were reshaped into vectors in MATLAB and concatenated together before being passed to the histc function. To differentiate the histograms from those in ImageJ, any post-processing steps can applied to the output of histc. The one we are interested in is taking the logarithm of the output frequencies to better visualize distributions when compared to ImageJ histograms. The plots can then be displayed using MATLAB's "bar" function.

3.3 BBB Data and Results

3.3.1 HBMEC VCAM-1 Staining

The HBMECs were analyzed in ImageJ using the Cell Counter and Histogram functionalities to determine relative levels of fluorescence emitted by VCAM-1 staining. Fluorescence is correlated to VCAM-1 expression which can be compared with other samples. Fluorescence intensity is used to quantitatively compare samples both from the same experiment and other experiments. The nucleus and VCAM-1 stains were also combined to view localization of VCAM-1. The nucleus appears blue and VCAM-1 appears red. For cell counting, partial nuclei are included, although partial cells are not counted fully. Instead, any partial cells are typically counted as half unless the nuclei are almost completely outside the field of view.

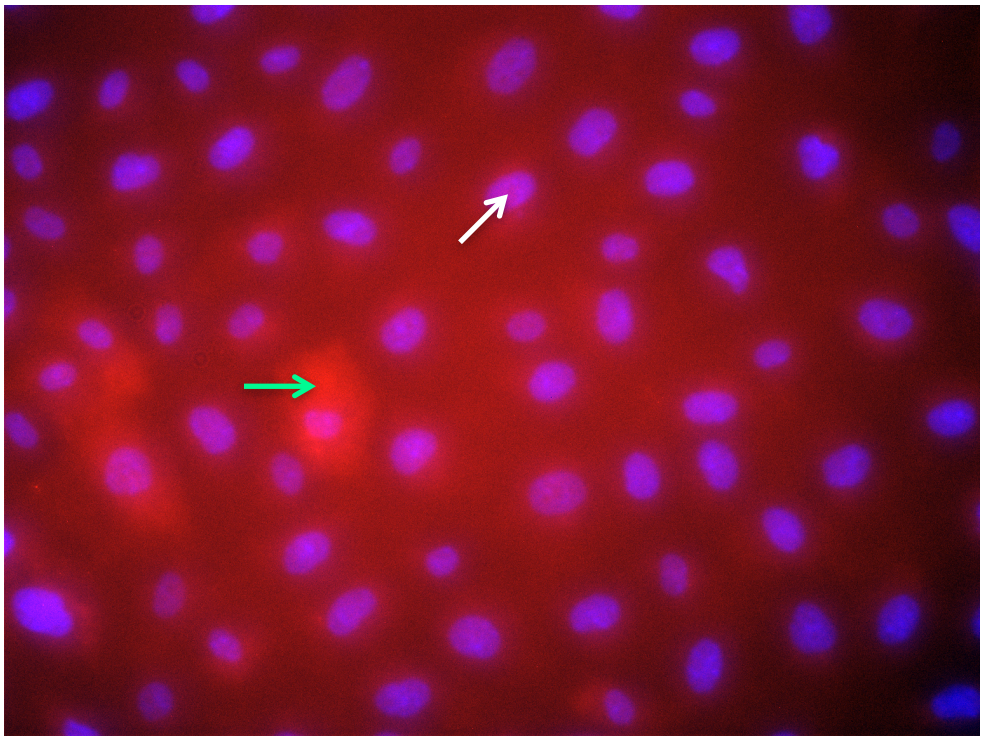

Figure 19. Composite image created of VCAM-1 stained HBMECs incubated without TNF-α. Very little localization of VCAM-1 expression is seen as most of the fluorescence is very diffuse. The white arrow indicates blue nuclei staining, and the green arrow indicates VCAM-1 staining.

As seen above in Figure 19, VCAM-1 staining for cells incubated with 0 µg/mL of TNF-α show very different levels of fluorescence throughout the sample. There is no specific localization of VCAM-1 in the cell layer; rather, fluorescence appears in random fashion. The noisy image also suggests that VCAM-1 expression is fairly low, which in turn suggests low fluorescent intensities. However, the mean fluorescence intensity (MFI) of the HBMECs is 115 with 65 cells present in the image. For an 8-bit image with pixel values ranging from 0 to 255, the MFI falls in the middle range of pixel intensities. This does not necessarily follow with the previous assumption that the fluorescence is low. To compare the results with the other samples, the fluorescence intensity is normalized by the number of cells, giving a value of 1.77 MFI per cell (MPC).

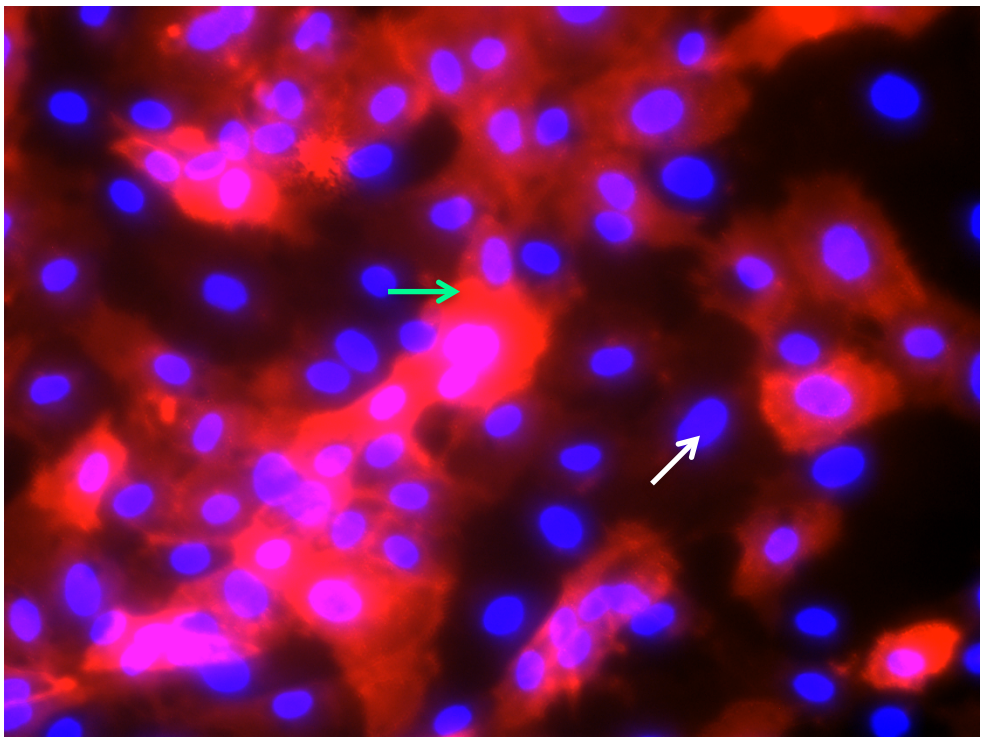

Figure 20. Composite image created of VCAM-1 stained HBMECs incubated with 2 µg/mL of TNF-α. Localization of VCAM-1 expression is evident as noticeable structures are occurring that are not present in the sample without TNF-α. The white arrow indicates blue nuclei staining, and the green arrow indicates VCAM-1 staining.

In the sample incubated with 2 µg/mL TNF-α, localization of VCAM-1 is readily apparent. VCAM-1 expression is no longer diffuse throughout the sample, as several regions in the image have higher levels of fluorescence unlike in the previous sample. By simple visual inspection, the fluorescence also appears to be greater with the inclusion of TNF-α, as there is less noise distorting the image. The MFI in turn is higher at 179 with 89 cells. Once normalized, the MPC becomes 2. Expression still looks to be fairly homogeneous, as most cells are expressing the receptor. There are a few cells that are not expressing VCAM-1 as well as some that are exhibiting low levels of expression. However, the overall trend shows increased expression of VCAM-1 in the presence of TNF-α.

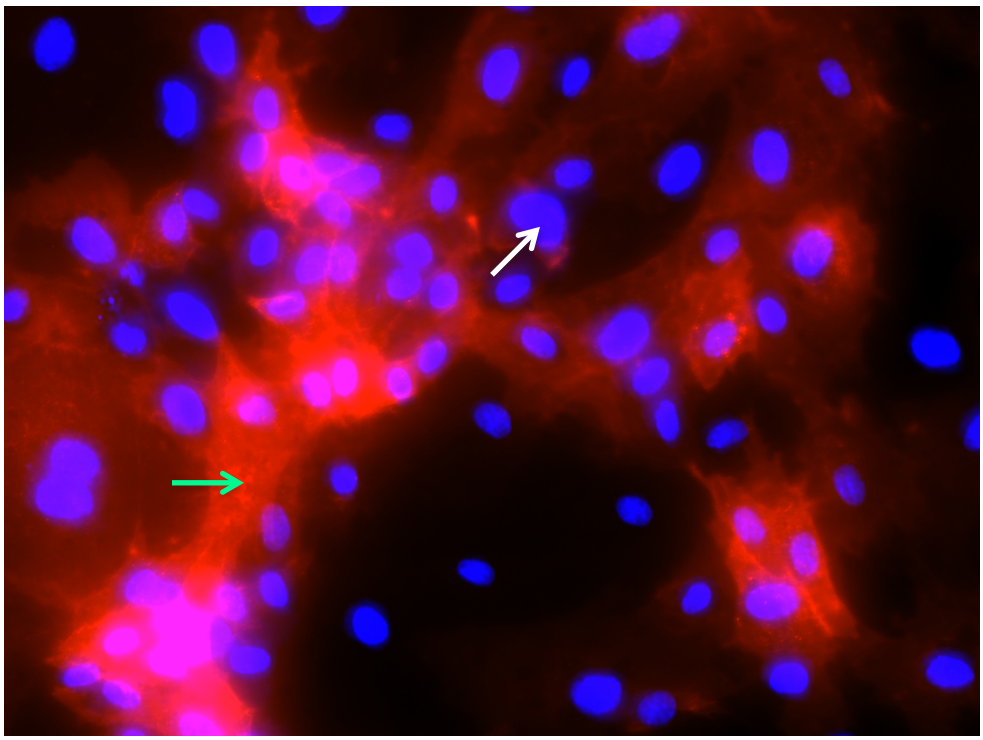

Figure 21. Composite image created of VCAM-1 stained HBMECs incubated with 20 µg/mL of TNF-α. Localization of VCAM-1 expression is evident again, but there are more cells that are either not expressing or weakly expressing the receptor. The white arrow indicates blue nuclei staining, and the green arrow indicates VCAM-1 staining.

The superficial results of the 20μg/mL sample are similar with respect to the previous sample. Localization of VCAM-1 is clear, as several cells are not expressing any of the receptor while some are expressing it very strongly. The pattern of expression is different from the previous two samples though, with fewer regions of VCAM-1 expression as well as slightly more defined boundaries of fluorescence. The images do not give a strong indication of the morphological changes, although some of the VCAM-1 structures look narrower. As a result of the different pattern, the MPC is only 116 with 79 cells, with a corresponding normalized value of only 1.47. The normalized value is lower than either of the two samples, indicating that there is an overall decrease in VCAM-1 expression that is unexpected of an increase in TNF-α.

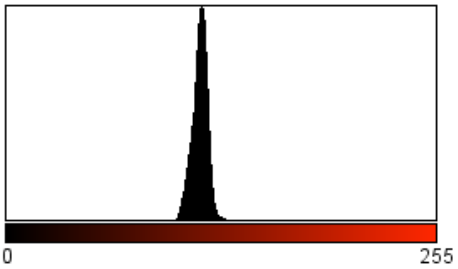

a)

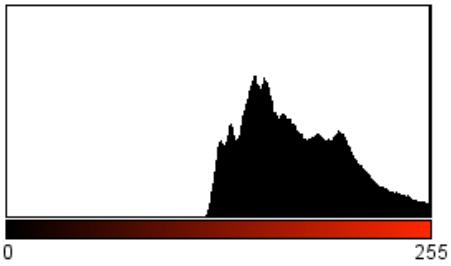

b)

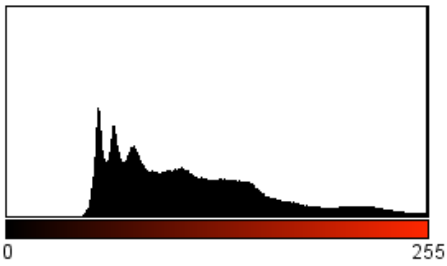

c)

Figure 22. Histograms representing the pixel intensity distributions of the three images, corresponding to the a) 0 µg/mL, b) 2 µg/mL, and c) 20 µg/mL samples. As the TNF-α concentration increases, distribution of pixel intensities widens.

To look for differences beyond the mean values, the histograms are also compared as a way to better gauge overall VCAM-1 expression. By simply observing distributions, TNF-α has a clear effect on the fluorescence intensity distribution. The

distribution for 0 μg/mL is very narrow and centered towards the middle of all intensity values. Considering the noise present in the image, it is no surprise that distribution is as so. The distributions for when TNF-α is added are wider and represent more pixel intensities. The overall trend seems to be that TNF-α widens the distribution of the fluorescence intensity, not necessarily just the raw mean intensity. The shapes of the distributions are also different. When no TNF-α is present, the shape is fairly symmetric about the mean, whereas when TNF-α is present the shape is more positively skewed. Having a wider distribution is indicative of more fluorescence, as the intensity is higher than the background noise. This is not reflected in only the mean intensity values.

Count: 1447680 Min: 0
Mean: 16.937 Max: 157
StdDev: 4.637 Mode: 18 (130183)

a)

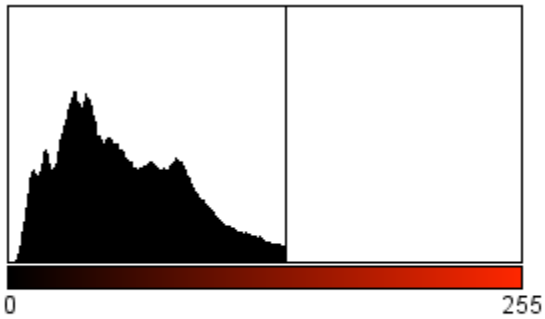

Count: 1447680 Min: 0
Mean: 61.872 Max: 138
StdDev: 35.771 Mode: 138 (90383)

b)

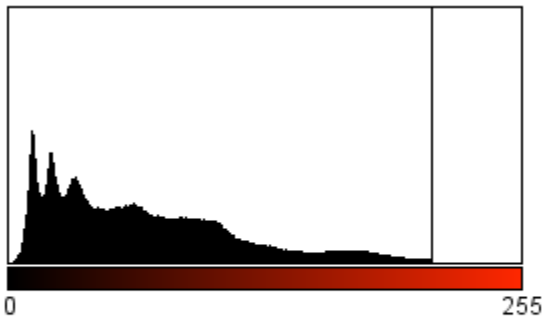

Count: 1447680 Min: 0
Mean: 72.025 Max: 211
StdDev: 53.324 Mode: 211 (47601)

c)

Figure 23. Histograms representing the pixel intensity distributions of the three images, adjusted to normalize all three background values to 0. The histograms correspond to the a) 0 µg/mL, b) 2 µg/mL, and c) 20 µg/mL samples. A trend in the means is more apparent in the adjusted data.

An underlying issue in the distributions is evident from the histograms. If the differences in background noise are not taken into account, then there is no reasonable trend of VCAM-1 expression in relation to TNF-α. The minimum values, which represent the background, differ greatly between the 20 μg/mL sample and the other two samples. To correct for the discrepancy, the histograms are shifted so that the minimum values become 0, negating the baseline background signal in the analysis. With the baselines uniform, the relative fluorescence intensities can be compared without any confounding factors.

Once the background is subtracted out, the MFI for the three levels of TNF-α correspond to 16.9, 61.872, and 72.025. Now the trend is positive correlation between VCAM-1 and TNF-α which is not readily apparent in the unadjusted data. The trend is not linear, which is unsurprising. Instead, the trend looks logarithmic. The relative difference between the 0 μg/mL and the 2 μg/mL is maintained since the backgrounds for the two samples were the same. An important note is that the difference between the two levels of TNF-α is not that large, despite the increase by an order of magnitude. This reinforces the notion that the fluorescence intensity follows a logarithmic trend for a linear increase in TNF-α. This indicates that small concentrations of TNF-alpha are sufficient to express VCAM-1 at high levels.

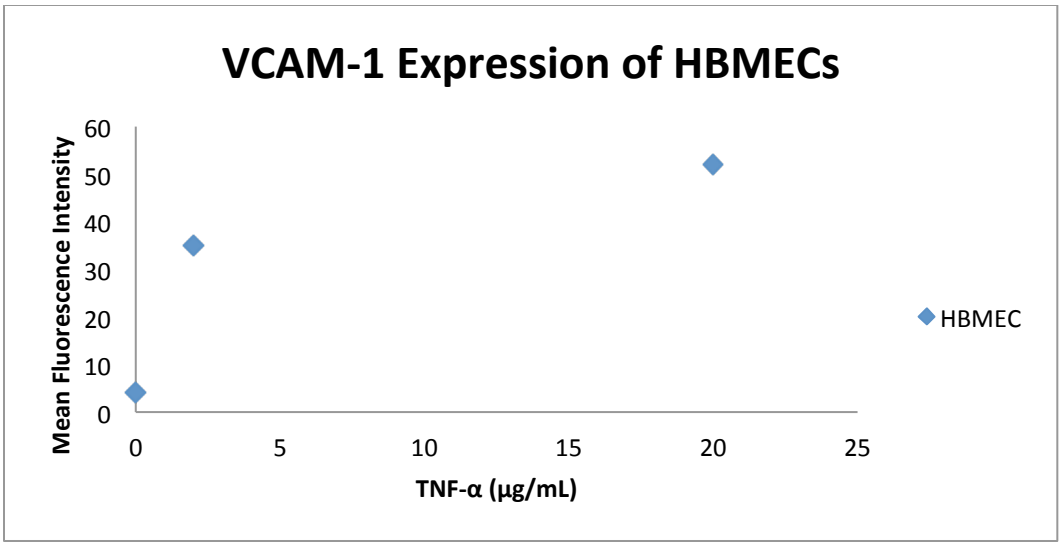

Figure 24. Trends of VCAM-1 expression in HBMECs in relation to TNF-α. The expression trend is similar to a logarithmic trend, with the highest concentration of TNF-α yielding the highest quantity of fluorescence. Points represent a single datum point.

In Figure 24, we can see a clear trend in VCAM-1 expression in relation to TNF-α. The trend is logarithmic, as there is a large increase in fluorescence from the sample without TNF-α to the 2 µg/mL sample. The difference between the 2 µg/mL and the 20 µg/mL sample is comparatively smaller. The difference is less important than the establishment of the logarithmic trend in VCAM-1 expression.

3.3.2 HUVEC VCAM-1 Staining

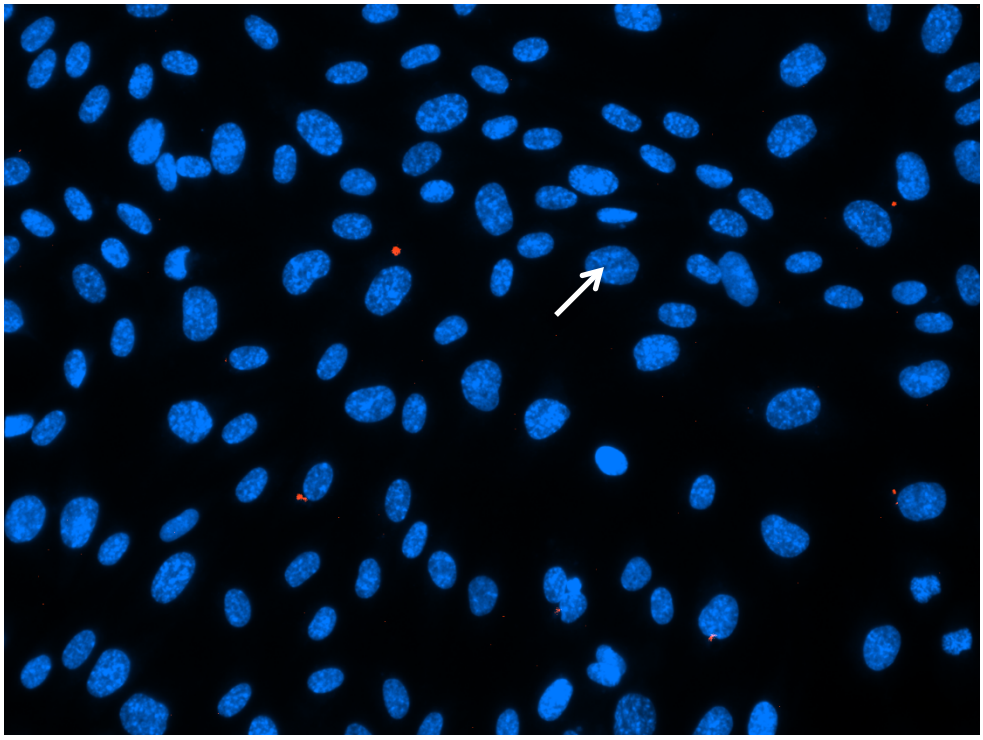

Figure 25. Composite image created of VCAM-1 stained HUVECs incubated without TNF-α. VCAM-1 is barely visible as it is indistinguishable from the background, much like in the HMBEC sample. The white arrow indicates blue nuclei staining.

The set of VCAM-1 stains on HUVEC cells was put through the same analysis steps as the HBMEC set. As seen in Figure 25, very little signal appears in the VCAM-1 fluorescence. Thus expression is not any different from the background captured by the camera. The result is not surprising, as HUVECs are not expected to express significant levels of VCAM-1 without cytokine stimulation.[78] The two samples taken have MFIs corresponding to 3.89 and 3.82 against 128 and 112 cells respectively. The result is a MPC of 0.03 and 0.034. Compared to HBMECs, HUVECs with no cytokine activation have about 1.75 orders of magnitude lower VCAM-1 expression. Unlike the HBMEC data, these numbers are low even without any adjustment to normalize background values.

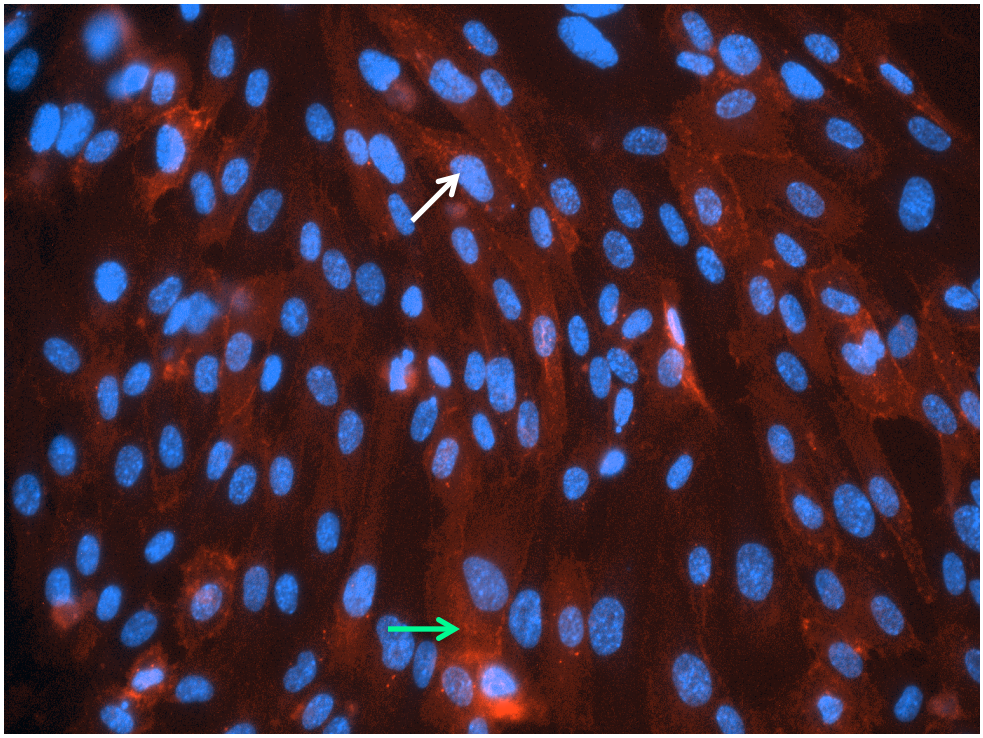

Figure 26. Composite image created of VCAM-1 stained HUVECs incubated with 2 µg/mL of TNF-α. VCAM-1 expression is visible, although fluorescence is not very strong compared to the HBMEC sample. The white arrow indicates blue nuclei staining, and the green arrow indicates VCAM-1 staining.

VCAM-1 expression is visible once the TNF-α is added to the samples. The same problem that plagues the HBMEC 0 µg/mL sample appears in the HUVEC samples though. The signal is weak, resulting in visible noise throughout the image. However it is consistent with the lower baseline VCAM-1 expression. The difference is that the fluorescence is distinguishable from the background noise, allowing visual confirmation of VCAM-1 expression. Visually, the boundaries of cells are more visible in the lower expression. Cell morphology is also more recognizable as the fluorescence does not seem to be overlapping.

An interesting revelation from the images is that the increased fluorescence is not reflected by the quantitative data. The two samples have MFIs of 4.5329 and 4.4806 to 136 and 141 cells respectively. While the mean values indicate an overall increase in

fluorescence, the normalized values come out to 0.033 and 0.032 which are not significantly different from the sample without TNF-α. The disparity between the measurements and the visual evidence thus is not a result of simply the normalized fluorescence. It is more likely due to a marginally wider distribution of fluorescence intensities, much like in the HBMEC samples.

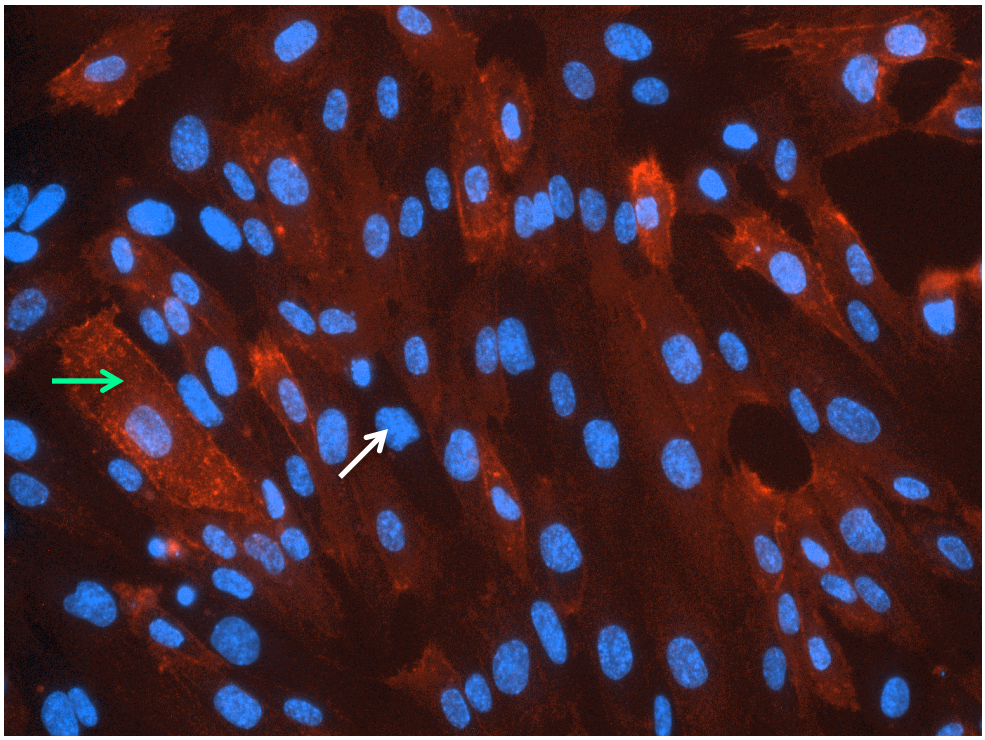

Figure 27. Composite image created of VCAM-1 stained HUVECs incubated with 20 µg/mL of TNF-α. VCAM-1 expression is comparable to the previous sample and shows fewer regions of no expression compared to the analogous HBMEC sample. The white arrow indicates blue nuclei staining, and the green arrow indicates VCAM-1 staining.

Similar results are seen when the sample is incubated with 20 µg/mL TNF-α. Visually, VCAM-1 expression is no different from the previous sample. The same noise is present, indicating that the fluorescence will not be much higher than before. The structure of VCAM-1 is very similar, showing that cell morphology is nearly unchanged in the presence of TNF-α. A major difference between the HUVEC and the HBMEC samples is the extent of expression. In the HBMEC sample, there are some cells not

expressing VCAM-1, resulting in dark spots in the image. While there are still a couple of dark spots in the 20 μg/mL sample, the amount of space is not on par with the HBMEC sample. Instead, it is more similar to the 2 μg/mL sample, where there are only a few dark spots and also a few areas of low fluorescence intensity.

The MFI of both samples is 4.5192, with 103 and 98 cells in each. The MFI is about the same as the previous sample, which reinforces the visual similarity. The MPCs are 0.44 and 0.46, a rise from the previous sample. VCAM-1 expression is expected to increase as TNF-α increases in HUVECs, which the MPC shows.[79] It also shows that the trend in VCAM-1 expression is similar to that seen in the HBMEC sample. However, considering how evenly VCAM-1 expression is expressed throughout the entire sample, normalizing to the number of cells may not be a reasonable move. While both the MFI and MPC are taken into account, the MFI holds more weight, at least in the HUVEC samples.

A result of the significantly lower intensity values is the drastically narrower intensity distributions available. The standard histograms produced by ImageJ are not presented as the displayed distributions do not represent the image overall. The range of values displayed on the histogram needs to be reduced because of the overall lower intensity. Also with fewer pixels representing the higher intensities, a standard histogram does not do justice to the pixels resulting in the displayed intensity. To better represent the distribution of fluorescence intensity, the histograms are made in MATLAB and the axes readjusted to better represent the data. The frequency count axis is scaled by a base 10 logarithm to better account for the lower number of pixels in the higher intensity

values. The range of intensity values plotted is also reduced to give a better view of the range of intensities.

a)

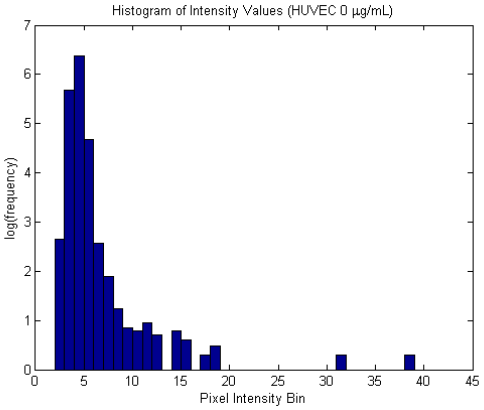

b)

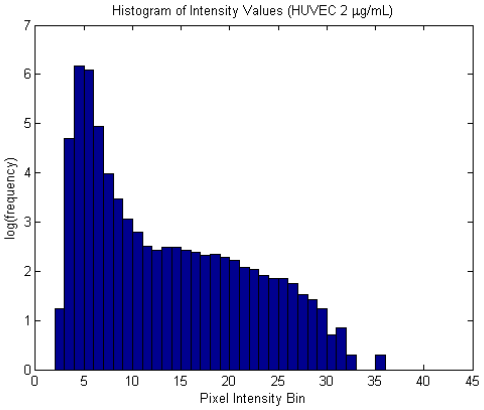

c)

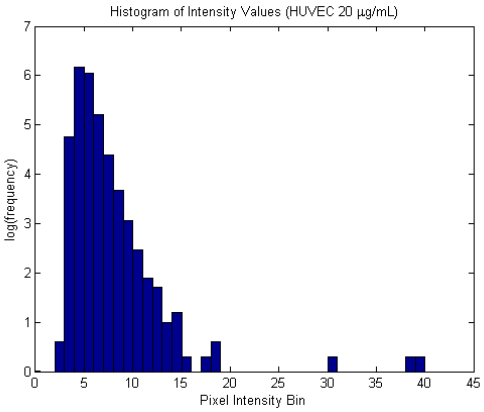

Figure 28. Histograms representing the pixel intensity distributions of the three images, corresponding to the a) 0 µg/mL, b) 2 µg/mL, and c) 20 µg/mL samples. The pattern of widened distributions does not hold through the HUVEC samples.

Fluorescence intensity distribution of the HUVECs reveals about the same amount of information as with the HBMECs. The narrow band present in the 0 μg/mL sample shows the reason for the lack of significant visualized fluorescence, much like in the HBMEC sample. Most of the contribution to the fluorescence comes from approximately 5 pixel intensities low in the spectrum. Considering how the background value has a pixel intensity of 3, there is not much of a jump between background and significant portions of the signal. This along with the lack of a 0-intensity pixel results in an image where most of the pixels are indistinguishable from the background noise. If a pixel value of 10 is arbitrarily taken to be visible, then less than 50 pixels are very visible, resulting in the few visible fluorescence areas.

With the addition of TNF-α, the intensity distribution widens much like with HBMECs. However, the trend is not the same, as the 2μg/mL sample has a much wider distribution than the 20 μg/mL sample. The 2μg/mL sample has many values that are well above the arbitrary threshold of visibility. The wide distribution accounts for the increased VCAM-1 visibility as more fluorescence is distinguishable from background. The reasoning is slightly different for the final sample. The presence of a 0-intensity pixel allows for the background to be distinguishable from signal. The distribution is also slightly wider than in the 0 μg/mL sample; while there are fewer pixels above the arbitrary visibility limit than in the 20 μg/mL sample, it still allows for easier visualization of the VCAM-1. Also, with the background shifted because of the presence of a 0 intensity pixel, more signal is visible because it is less likely to be confused as background.

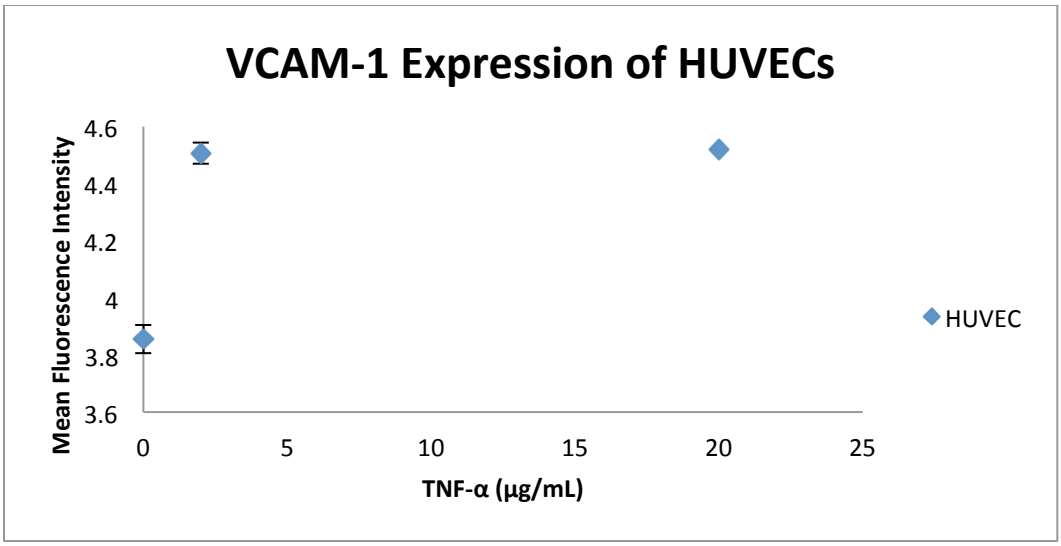

Figure 29. Trends of VCAM-1 expression in HUVECs in relation to TNF-α. The expression trend once again looks logarithmic, although the difference in fluorescence between the 2 µg/mL and the 20 µg/mL samples is smaller than in the HBMECs. All points represent averages of two data points.

Once again we can observe the expression trend in HUVECs in Figure 29. Much like in the HBMEC samples, the expression trend is logarithmic, as there is a large difference in fluorescence between the 0 µg/mL and 2 µg/mL samples, but not the 20 µg/mL sample. As seen earlier, the difference between the 2 µg/mL and 20 µg/mL groups is almost zero. However, this is inline with what we have seen in the HBMECs, with the only difference being a lower magnitude of fluorescence. While the HUVECs are not present in the BBB, we have shown that the VCAM-1 expression trends are similar to the HBMECs, providing a relationship between our use of HUVECs and their HBMEC counterparts.

3.3.3 HUVEC Bead Experiments

HUVECs incubated with TNF-α and fluorescent beads are subjected to the same analysis as the VCAM-1 experiments. However, without any nucleus stain, MFIs are presented without the corresponding MPC value. Also, fluorescence is superimposed on phase contrast images as opposed to nucleus stains to show localization of bead uptake in relation to cells.

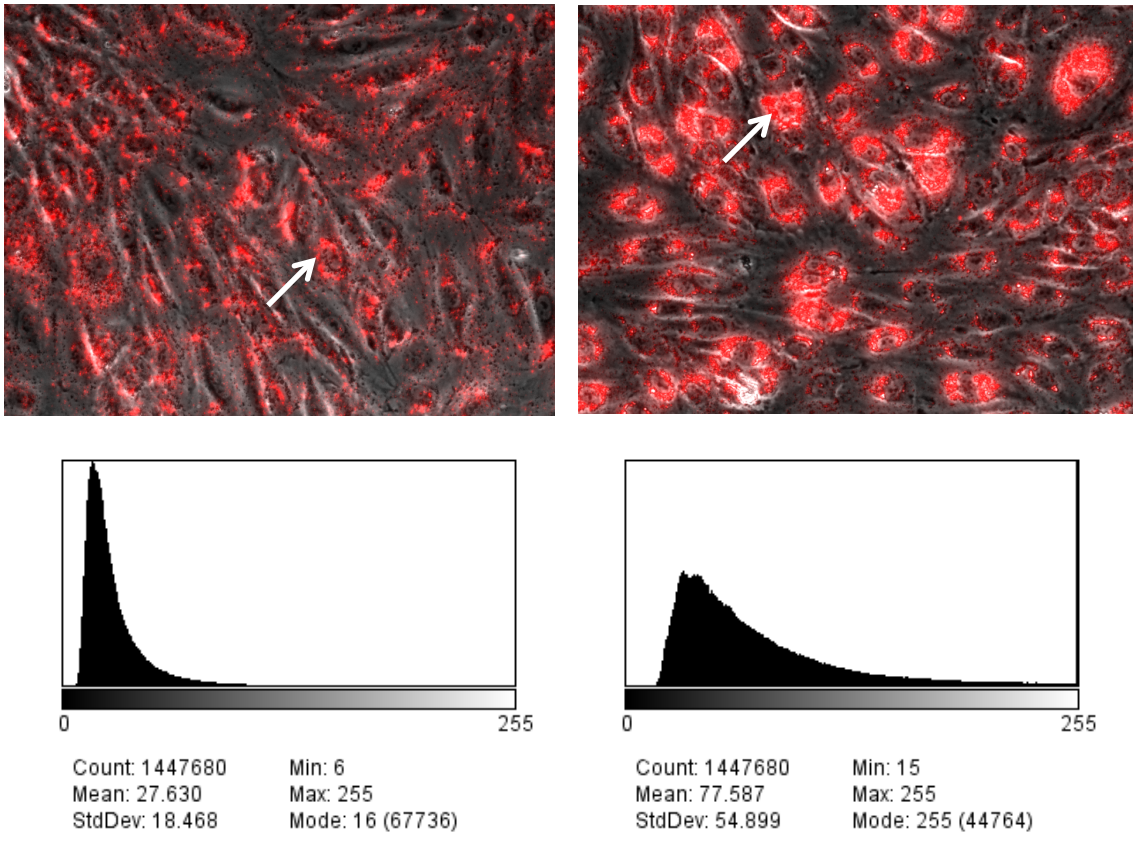

a) b)

Figure 30. Composite images and histograms depicting analysis of bead absorption in HUVECs incubated with no TNF-α. The a) 1 hour and b) 5 hour time points are shown, with a large increase in fluorescence visible. The white arrows indicate fluorescent bead aggregation around cells.

A comparison of the 1 and 5 hour time points is a rough way of estimating the baseline absorption kinetics of the HUVECs. For each 1-hour time point sample, 3 images are presented corresponding to the levels of TNF-α used. For the sample without

TNF-α, the MFI across the trials is 29.1. Fluorescence is clearly visible in the sample, showing that these samples do not share the same troubles as the VCAM-1 staining. While not fluorescing intensely, the beads are clearly distinguishable from the background. Beads appear to localize in and near cells, showing the degree of non-specific absorption in HUVECs. Another important observation is the degradation of the monolayer in the presence of the beads. Even without the presence of TNF-α, the monolayer is no longer tight, although the cell morphology is not changed significantly.

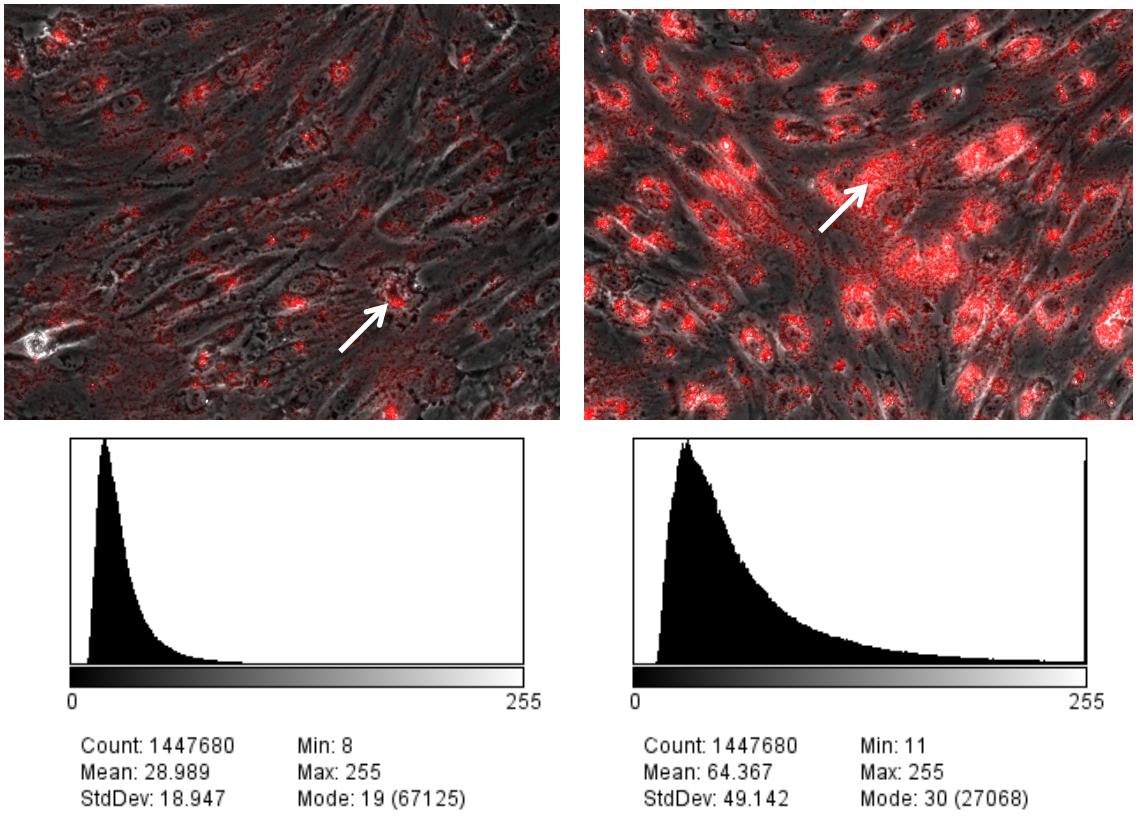

a) b)

Figure 31. Composite images and histograms depicting analysis of bead absorption in HUVECs incubated with 2 µg/mL TNF-α. The a) 1 hour and b) 5 hour time points are shown, with only marginal increases from the previous sample. The white arrows indicate fluorescent bead aggregation around cells.

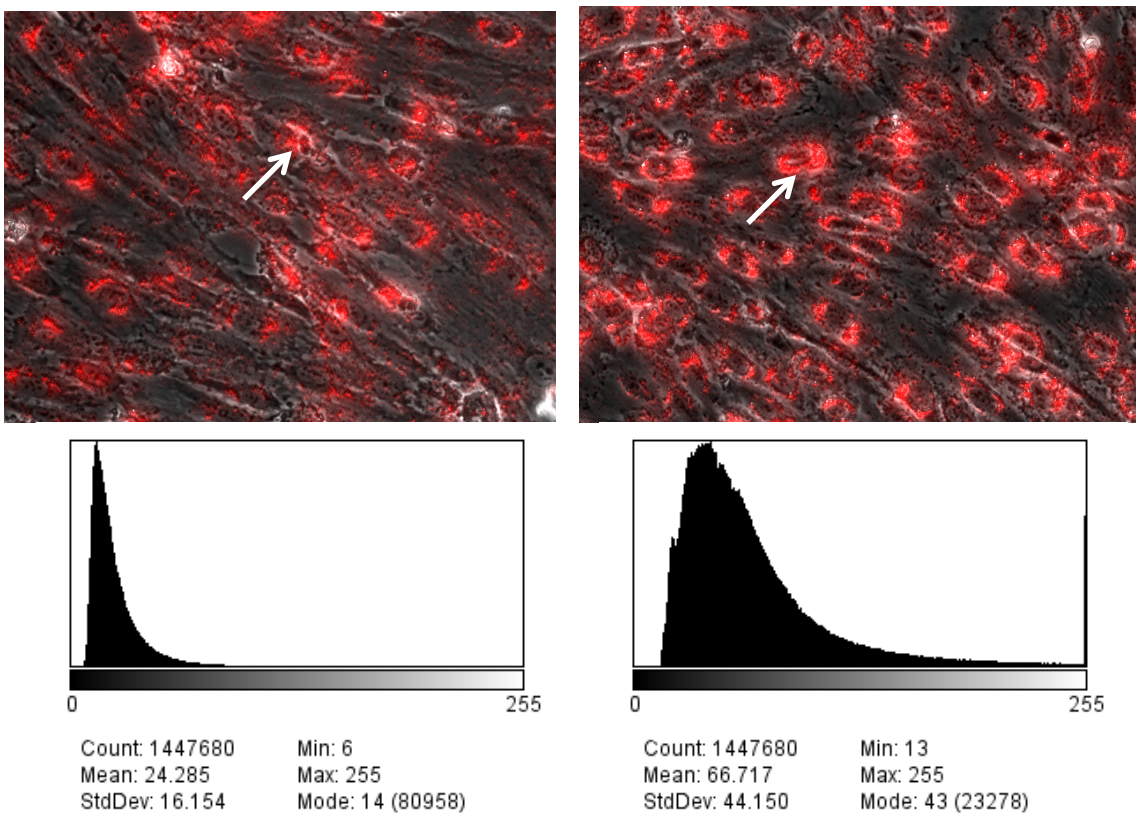

a) b)

Figure 32. Composite images and histograms depicting analysis of bead absorption in HUVECs incubated with 20 µg/mL TNF-α. The a) 1 hour and b) 5 hour time points are shown. Overall the trend from the VCAM-1 experiments are not necessarily maintained. The white arrows indicate fluorescent bead aggregation around cells.

The pattern of fluorescence for the two TNF-α samples looks similar to the results found in the VCAM-1 staining samples. Over the three samples of HUVECs incubated in 2 µg/mL TNF-α, the MFI is 28.1, whereas the MFI is 25.2 in the 20µg/mL sample. There is an evident dip in the number of beads absorbed by the cells in the final sample, something seen in the unadjusted HBMEC sample. The difference is that there is no adjustment in these results as the background is very much the same, thus the trend stands as is. Something to note in these samples is that cell layer morphology is changing in the presence of TNF-α, something not as evident in the VCAM-1 staining samples.

The monolayer is disrupted in both samples, with the 20 μg/mL sample suffering more. Despite the expectation that absorption should increase, TNF-α's effect on the monolayer must also be taken into account.

For the five hour time points, bead localization increases as seen from a visual inspection. A higher concentration of beads also localize in and near cells at all three levels of TNF-α as seen by the increased levels of fluorescence at bead clusters. The pattern at 5 hours is mostly maintained; there are many clusters of fluorescence corresponding to more intact cells and a better cell layer for the sample without TNF-α. The MFI over 2 samples is 73.9, yielding approximately a 2.5x increase in fluorescence over the 4 hours. The MFI for the 2 μg/mL and 20 μg/mL sample is 62.1 and 59.3 respectively over 2 and 3 images. These results correspond to a 2.2x and a 2.35x increase in fluorescence. Cell layer morphology patterns are seen once again as expected, which partially accounts for the trend seen in fluorescence levels.

Distributions for all six sets of data do not yield much more information. Unlike the previous experiment, where the distributions changed significantly depending on the level of TNF-α, the shapes of the distributions are more or less the same at the one hour time points. The shape does not grow wider nor does the mean shift like in the VCAM-1 experiments. At the five hour time points, the distribution towards the lower end of pixel intensities grow slightly wider with the addition of TNF-α, although this fact is not reflected by the mean intensity values. Despite the fluctuations in the fluorescence level, the results draw a rough picture of non-specific absorption by HUVECs which will be compared to specific absorption of the nanoparticle complex.

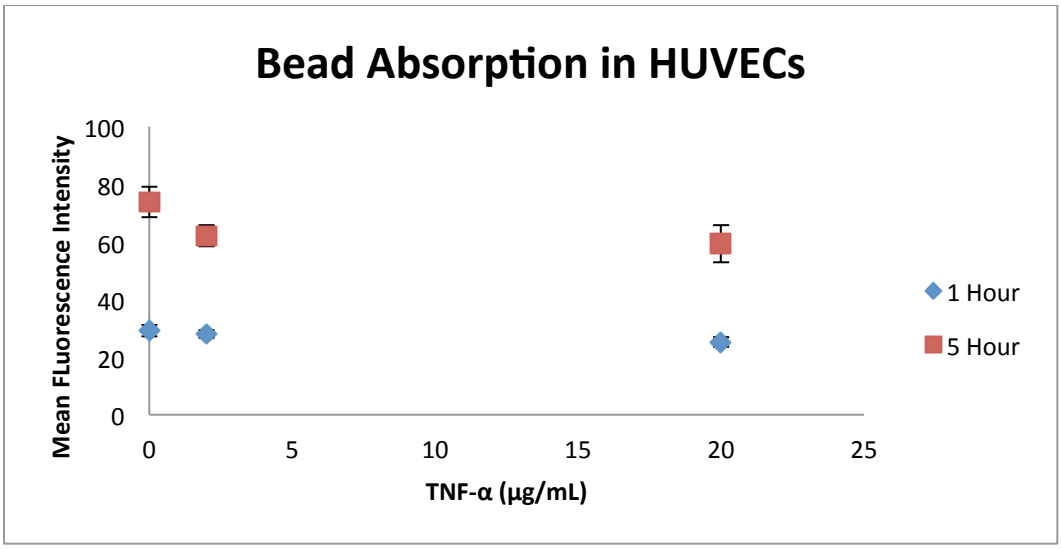

Figure 33. Trends of non-specific bead absorption in HUVECs. The 1-hour and 5-hour time points are shown. At both time points, both trends appear to be similar to exponential decay as opposed to the logarithmic trend in VCAM-1 expression. All points represent averages of two data points, with the exception of the 5-hour 20 µg/mL group, which averages three.

For the bead absorption experiments, we see a slightly different trend, as seen in Figure 33. The absorption trend looks similar to exponential decay, indicating a logarithmic decrease in fluorescence in relation to TNF-α. The maximum amount of fluorescence occurs in the bead sample incubated without TNF-α and the minimum occurs in the sample incubated with 20 µg/mL TNF-α. The trend is more noticeable at the 5-hour time point as the magnitude of fluorescence is higher. As we can see, the trends are inversely correlated with VCAM-1 expression; less bead absorption occurs with higher levels of TNF-α.

3.4 Blood Brain Barrier Discussion

Before discussing the results presented in the section above, we would like to first address the simplicities that we made in our BBB model formation, as we recognize that this likely plays a significant role in results obtained. As described in the background of this section, the *in vivo* BBB is not only composed of ECs with TJs, but also includes basal lamina, pericytes, astrocytes, interneurons, and microglia[58].

The first steps in developing this complex BBB model were to culture ECs on the Transwell surface without any other components, and to then measure the corresponding electrical resistance values to establish barrier characteristics. It was at this point that we ran into several problems, including the inability to produce consistent electrical resistance values, and the presence of excessive debris in the inserts. As we ran into these problems, we came to realize that we did not have a budget to support the continued purchase of these Transwell inserts nor the purchase of materials needed to start up and maintain the other cell lines that we would eventually want to add to the model. Because of these monetary and time constraints, many simplifications needed to be made to our BBB model. The Transwell inserts and additional cell lines were removed from our list of materials, as were components for use in synthesizing hydrogels. What we were left with, then, was a glass coverslip to which we would grow our EC monolayer. We realize that this final BBB model use in our experiments has many limitations. For example, without a hydrogel, or some sort of permeable substance/membrane, we cannot evaluate the effectiveness of our drug delivery model's movement within the 'brain' portion of the BBB model. Instead, we focus on strictly understanding the ability of our drug delivery complex to utilize VCAM-1 proteins expressed on the apical surface of the endothelium

as a method of beginning the traversing process. For the short term, showing that VCAM-1 can be used as a targeting molecule to help deliver drugs through the BBB would provide a solid foundation for future studies that, when using a more complex and developed *in vitro* BBB model, could explore how these drug delivery mechanisms interact with the rest of the BBB and brain once they pass the endothelial layer.

There are two key aspects to this portion of the overall experimental plan: characterizing VCAM-1 expression under the influence of TNF-α, and obtaining a rough estimate of the non-specific absorption properties of HUVECs.

3.4.1 Characterizing VCAM-1 Expression under the Influence of TNF-α

Ideally, HBMECs would have been the cell type used in the *in vitro* BBB model. However, a variety of problems stifled the ability for the cells to produce viable and reproducible results. After the VCAM-1 staining, the HBMECs were unable to grow in a healthy and predictable manner (others report difficulties in HBMEC culture as well), forcing a change to HUVECs.[80] We recognize that there are significant differences between these two cell lines, as HBMECs are used more in micro-circulatory studies and HUVECs are used in more macro-circulatory studies[81]. For example, while perhaps not a very significant difference for the purposes of our studies, HBMECs and HUVECs respond very differently to certain xenobiotics.[82] Another example is the difference in glycosphingolipid (GSL) patterns between HBMECs and HUVECs; in particular, the amount of globotriaosylceramide (Gb3), a neutral GSL, in HBMECs is approximately double that found in HUVECs.[80] While this may not seem to be of much importance here, as we are not interested in the effects of GSL expression for our drug delivery

method, it is interesting to note that other studies have found that Gb3 induces oxidative stress as well as up-regulates the expression of ICAM-1, E-selectin, and VCAM-1 in ECs related to Fabry disease.[83] Clearly, there are differences between HBMECs and HUVECs that would give preference to the use of HBMECs in our model since they would help us more closely replicate the *in vivo* conditions of the BBB. However, given that both cell types are human ECs, we expected that, despite their differences, their similarities in simple behavior and adhesion protein expression would allow for HUVECs to be a reasonable analog for our purposes.

With VCAM-1 as the nanoparticle's target, it was imperative that we characterize the difference in this protein expression between the two cell types. Without a handle on the difference, we cannot justify the use of HUVECs in our model. One problem that arose in the HBMECs was the VCAM-1 response to TNF-α. With increased levels of cytokines, VCAM-1 expression is expected to increase.[84,85] However, with the highest concentration of TNF-α (20 μg/mL), VCAM-1 expression actually decreases throughout the sample. An interesting observation from the experiments is the lack of expression in certain areas of the 20 μg/mL sample, which accounts for the lower fluorescence values. The only noticeable patterns as the concentration of TNF-α increased were fewer cells expressing VCAM-1 and the distribution of VCAM-1 expression within cells becoming increasingly patchy.

As mentioned earlier, there is a large disparity in fluorescence between the 2 μg/mL and 20 μg/mL samples. While the two samples look similar visually, the underlying fluorescence intensity differs. If VCAM-1 expression increased as expected, more fluorescence would be seen along with it. Instead, both the total fluorescence and

the normalized fluorescence intensities at the highest concentration of TNF-α are similar to the control, the sample that was not incubated with any TNF-α. The caveat is the distribution of pixel values. Normally this would not be an issue; however in this case, there may be one. The background signal for the control case is much higher than the highest concentration case, although it is similar to the middle case. With such high intensity background noise, weak signals are indistinguishable, as seen in the control case. A result of the increased background noise is a higher mean fluorescence, as the background essentially shifts all the pixel intensities by a certain constant. The middle case is visible because the distribution extends beyond the background even though the baseline value for the highest level is actually much lower than the other two, which contributes to the lack of a trend. Once the background is eliminated, a clearer positive trend appears - which was expected. The large difference in level of expression between the control and middle data points is preserved, as the background level is approximately the same for the two. With the background eliminated, it is clear that there is more fluorescence – more VCAM-1 expression – with higher levels of TNF-α. It is possible to eliminate the background because it acts as the baseline for the image. As seen in the first image, almost none of the VCAM-1 expression is clearly seen in the fluorescence despite intensities on par with the other groups. However, most of the image is just background noise which doesn't contribute to the fluorescence. Since it is not a result of the actual fluorescence, it is skewing the data. Readjusting the data does not affect the information present; it simply brings it to light. Therefore, results show a positive logarithmic trend: increasing amounts of TNF-α cause increasing expression of the VCAM-1 protein in the HBMEC monolayer.

VCAM-1 expression data in HUVECs suffers from the same problems as the unadjusted HBMEC data. In the HUVEC images, however, the data cannot be adjusted to show the same type of information. Unlike the HBMECs, the HUVECs in general have much lower expression of VCAM-1, as seen in the results section. Because of this, all three samples show low fluorescence totals, and this time, the background values are approximately the same. Thus, there is no adjustment to the histograms, and the MFIs for the two TNF-α samples are more or less the same. This suggests that TNF-α only regulates VCAM-1 expression up to a certain threshold, perhaps below or around a concentration of 2 μg/mL, in HUVECs. The only indication that VCAM-1 expression might go up is when the fluorescence values are normalized to the number of cells, in which case there is a slight increase on par with the increase seen in the HBMEC samples. The minor increase is reasonable, given how little fluorescence is present.

However, an issue arises with the normalization, as across all the normalized values, there is almost no difference between the control and the middle (2 μg/mL) sample. Despite the clear visual difference between the two samples, the normalization results suggest that the two are no different. Upon speculation, normalization is most likely not the most reasonable option. For example, the middle sample clearly has more cells than either of the other samples, but when compared to the higher sample, fluorescence is approximately the same. Given the density of cells in the sample, there is less area per cell for VCAM-1 expression. Although the same amount may be expressed across all the cells, each cell produces less, yielding a lower normalized value. Even though we can use the normalized value to gain an understanding of what is happening

on a per-cell basis, it is more likely that the mean total fluorescence is more objective for use in drawing any substantial conclusions.

Despite the fact that the fluorescence levels differ very little between the two experimental groups, there is a definite up-regulation in the presence of TNF-α. This result bodes well for the purposes of our BBB model, as it shows that HBMECs and HUVECs react similarly in the presence of TNF-α in regards to VCAM-1 expression. Granted, level of expression is on a different order, which will affect how effective targeting the protein is, but the overall action should remain the same. We suspect that there exist other morphological changes that differ between the two cell types under cytokine stimulation, which could be confounding variables when using the HUVECs and our simplistic BBB model. However, the most important aspect for the purposes of our experimentation is VCAM-1. Without the similarity present, it would be unfeasible to expect the HUVECs to act as a good model for targeting.

3.4.2 Characterizing Non-specific and VCAM-1 related Absorption in HUVECs

Justifying the use of HUVECs in our model was only the first step, however. The next step was to form an understanding of non-specific absorption. We must be able to compare baseline absorption of the HUVEC monolayer under normal conditions to the specific absorption caused by the VCAM-1 targeting. Fluorescent beads are not specifically absorbed by cells and will act as a control to the nanoparticle testing. Due to previously mentioned problems with HBMEC culture, only HUVEC absorption is characterized. Since bead uptake is not specific, it was expected that HUVEC monolayers would absorb more fluorescent beads over time. Additionally, it was hypothesized that

on top of the already-present non-specific absorption, increasing VCAM-1 expression through the TNF-α pathway would result in even greater bead uptake.

While absorption is clear over the five hours observed, the levels of absorption are not as expected. At both the one and five hour time points, it appears that the introduction of either 2 or 20 μg/mL of TNF-α increases absorption marginally compared to the control sample, but increasing the concentration from 2 to 20 μg/mL only serves to decrease overall absorption when making comparisons solely between the two. This does not necessarily match any of the trends seen in the VCAM-1 experiments, which is disconcerting. The only time this shows up is in the unadjusted HBMEC data. Once again, the data is not as easily adjusted in this case, as the background across all the samples nearly identical. Any adjustments would yield negligible changes and the overall trend remains. We suggest the existence of a saturation level with TNF-α that may result in excessive concentrations giving conflicting results.

One of the more important results is the effect that TNF-α has on the cell monolayer. Although the absorption trend is not easily gleaned, the cell layer clearly changes in all the samples. Disruption is easy to see, as gaps between cells are more frequent and morphology is shifting away from those seen in a normal, healthy monolayer. This could partially explain why the trend observed and explained above is inconsistent with the VCAM-1 experiments. With the HUVECs, the pattern of VCAM-1 expression showed that even with the TNF-α, the monolayer was still relatively intact. The combination of the beads and TNF-α caused deterioration that is inconsistent with monolayer morphology observed with only TNF-α. This, in turn, caused an unexpected change in results. It is likely that the introduction of the beads was enough of a stimulus

to enable the deterioration, as even without TNF-α, there is a degree of disruption in the monolayer. With the amount of molecules in the vascular circulation at any given time, we believe that the introduction of beads should not have been enough to cause monolayer disruption. This leads us to suspect our simplistic BBB model as one of the contributing factors to this problem. We believe that future studies that use a more robust BBB model, with hydrogel, astrocytes, and other glial cells, would provide for the additional structural stability innate to the BBB endothelium. Another consideration is that our model lacks flow, something with is clearly present *in vivo* in circulation. Perhaps it was the static presence of the beads that contributed to the monolayer's disruption. Regardless, we recognize that our model likely played a role in some of the problems we saw in our experiments.

Because of this monolayer disruption, it is better to normalize the fluorescence intensities to the number of cells, as the space issue is less of a factor when the monolayer is disrupted. However, nucleus staining was not taken during the bead experiments, making cell counting more difficult. There are clearly cells in the sample, however, there are also other structures that look like cells that are much harder to discern under only phase microscopy. Attempting to count the number of cells would likely result in inconsistent results which would not aid our experiments. It is safer to use the non-normalized data; however the point is made that repeating experiments and normalizing the data could results in more consistent results.

Understanding the baseline absorption is somewhat difficult with only two time points available. Given that kinetics are driven by concentrations, we can assume that absorption follows a decaying exponential; however with only two points, it is still

difficult to characterize the curve – but it is still possible to obtain some useful information. We can still compare the fluorescence levels with other experiments to see the relative absorption rates. For example, the ratio of bead absorption at a particular time point is approximately two times as high as the previous time point. If we see that a different experiment exhibits significantly differing ratios and values, the mechanics of absorption are probably not using non-specific pathways.

To summarize, experiments aiming to obtain a rough estimate of the non-specific absorption properties of HUVECs suggest that most bead uptake was indeed non-specific, with increased VCAM-1 expression only marginally increasing absorption. While not agreeing with initial hypotheses, a TNF-α concentration of 2 μg/mL and bead exposure for five hours was optimal for getting the maximum absorption in our experiments.

3.4.3 Conclusions

The results from the BBB model section of our overall research plan highlight some important results that are important as we move forward. First, VCAM-1 expression, in general, increases as the concentration of TNF-α increases in HBMECs and HUVECs. In HUVECs, smaller concentrations of TNF-α and increasing time result in larger bead absorption, indicating that in at least some capacity, VCAM-1-specific interactions help in molecule absorption. Overall, our results support our decision to use VCAM-1 as a targeting molecule for our nanoparticle-based drug delivery system.

4. Nanoparticle Complex

4.1 Nanoparticle Complex Background

4.1.1 Cationic Solid Lipid Nanoparticles

Nanoparticles have been considered in previous studies as possible carriers for drugs across the BBB.[30,31,33] However, nanoparticles are broadly defined as solid colloidal particles ranging from 1-1000 nm in diameter, and there are several different types of nanoparticles which researchers have investigated.[30,31,86,87] Inorganic options for nanoparticles were not chosen for this study due to adverse effects caused by the lack of biodegradation of these materials, such as gold or silica, *in vivo*.[31] Nanoparticles formed traditionally by emulsion polymerization were also ruled out due the requirement that free radicals, radiation, or UV light are generally needed to trigger polymerization, as well as the dialysis necessary to purify these nanoparticles and maintain stability.[86] We further ruled out nanoparticle types which would have required our drug substitute (BODIPY-TMR) be attached to the surface of the particle to eliminate the possibility of the dye interacting with entities outside of the nanoparticles.

SLNs have been shown to have a high drug load capacity, a low incidence of toxicity in the body, and high stability during long term storage.[30] Studies have also shown that SLNs can be used for the sustained release of therapeutic agents, which demonstrates stability *in vivo.*[88] In addition to showing promise in the delivery of drugs throughout the body, there has also been success in targeting SLNs to the brain.[30,89,90,91]

The CSLNs used in this study were created based on a protocol developed by Kim et al.[29] While Kim utilized the carrying capacity of CSLNs to deliver siRNA to body cells, we will be exploiting the structure of CSLNs to carry a fluorescent dye, which will

simulate a drug, through the BBB. The CSLN components were based on the structure of low density lipoprotein (LDL) cholesterol complexes. LDL cholesterol is a naturally occurring nanoparticle abundant in the body, limiting the possibility of toxicity caused by the drug complex. Natural LDL nanoparticles have also been used previously in delivery of DNA for therapeutic purposes.[29] Creating CSLNs from the components of LDL rather than using naturally occurring LDL allows dye to be incorporated during the formation of the nanoparticles. Creating CSLNs is also more economically feasible than isolating naturally occurring LDL.

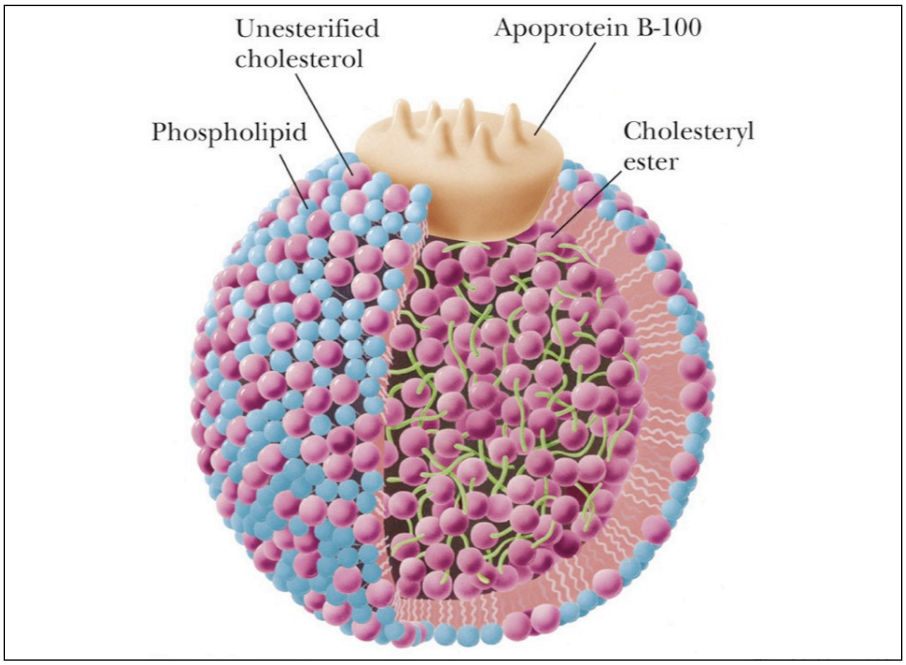

Figure 34. This image shows the composition of LDL. LDL is made up of many components, and so would be difficult to isolate naturally.
Cardiologydoc, cardiologydoc.wordpress.com

The nanoparticles used in this study are composed of cholesteryl oleate, glyceryl trioleate, DOPE, cholesterol, and DC-cholesterol. DOPE and cholesterol are incorporated in the nanoparticles because they are known to improve and stability and reduce the cytotoxicity of cationic lipids.[29] In particular, DOPE also facilitates the fusion of CSLNs

with endosomal membrane phospholipids.[29] Cholesterol was incorporated to provide morphological rigidity to the surface and to promote the stability of CSLNs.[29] DC-cholesterol was introduced as the major cationic lipid to generate positively charged CSLNs, since DC-cholesterol is considered to be less toxic than other comparable cationic lipids.[29] DC-cholesterol based carriers were approved in many clinical treatments, such as melanoma, cystic fibrosis, and breast cancers.[29] Based on previous literature, the ratio of DOPE to cholesterol to DC cholesterol in this protocol is at near optimal molar ratio for efficient liposome formulations.[29] The core of natural LDL is composed of cholesteryl ester and triglyceride.[29]

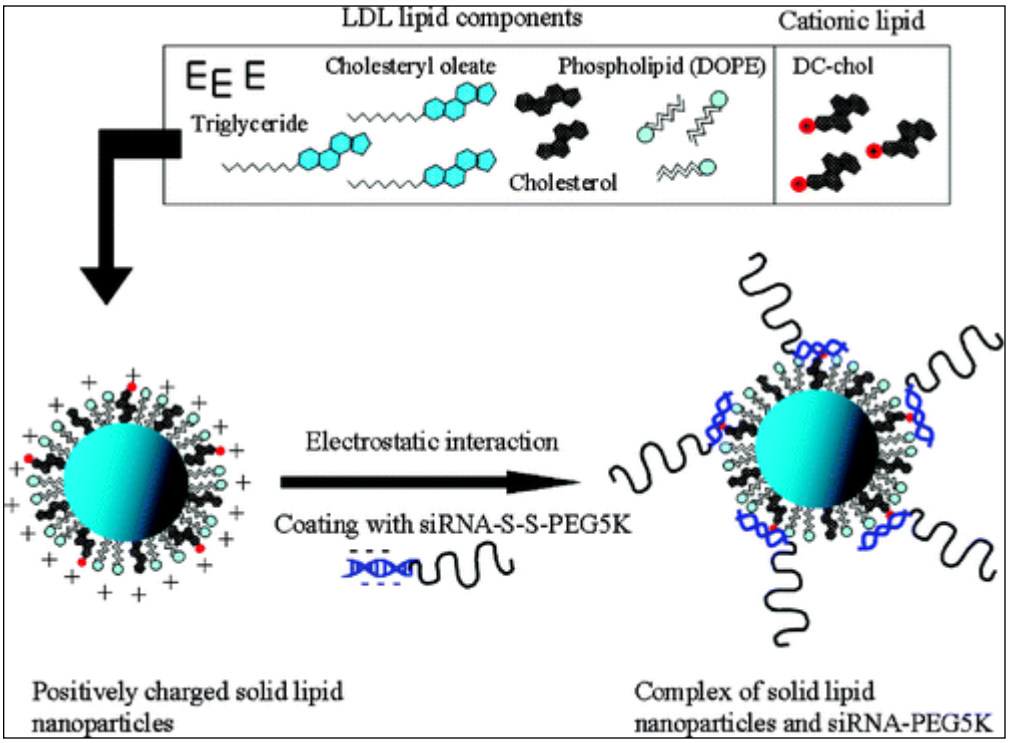

Figure 35. Schematic diagram of the assembly of cationic solid lipid nanoparticles. ACS Publications

4.1.2 Streptavidin

Streptavidin is a crystalline protein purified from the bacterium *Streptomyces avidinii.*[92] It is a 60 kDa tetrameric protein with four subunits, and has an extremely high affinity for biotin, which will be explained in greater detail later.[92] The quaternary structure of the streptavidin protein is composed of four streptavidin monomers, each composed of eight antiparallel β-turns that fold to form a β-barrel tertiary structure.[93] Each subunit contains a biotin binding site, giving each molecule of streptavidin a total of four biotin binding sites.[93]

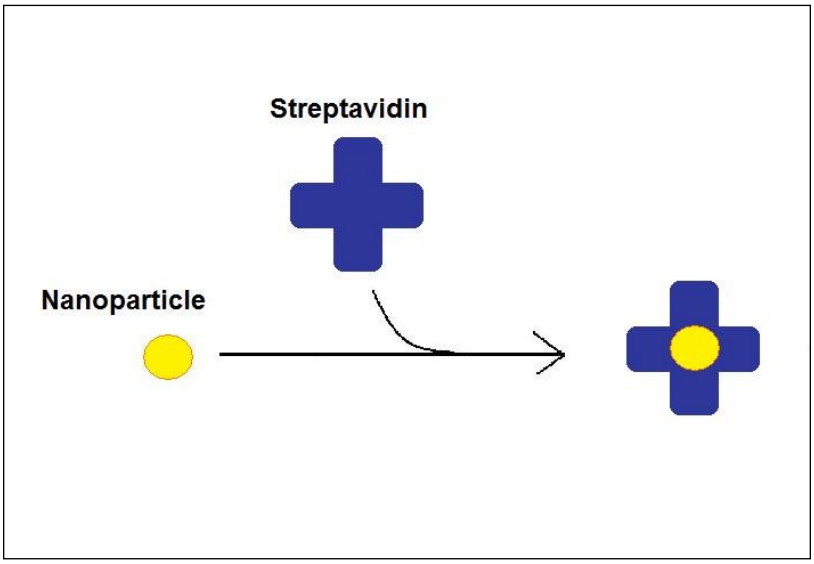

Figure 36. Attaching streptavidin to nanoparticles is the first step of the drug delivery complex; the streptavidin binds to nanoparticles due to electrostatic interactions. Figure not drawn according to scale.

At pH 7.2, streptavidin has a net negative charge because it has an acidic isoelectric point (pI = 5).[92] Streptavidin's negative charge allows it to bind with the positively charged SLNs in neutral biological conditions through electrostatic interactions. It is expected that in solution, streptavidin and SLNs will naturally aggregate and stick together, which completes the first part of our nanoparticle complex. The

purpose of streptavidin in this experiment is to act as a "glue" to connect the nanoparticle to the biotin. Since streptavidin is electrochemically attracted to the nanoparticle, and the biotin-streptavidin bond is the strongest non-covalent bond found in nature, streptavidin is the optimal linker between the nanoparticle and biotin.[94,95,96]

4.1.3 Biotin

The next component of the complex is biotin. Biotin is a vitamin (also known as Vitamin H or Vitamin B7) that is present in all living cells and is essential for numerous biological processes including cell growth, the production of fatty acids, and the functioning of the citric acid cycle. Biotin also works in the body to help transfer carbon dioxide, maintain a steady blood sugar level, and strengthen hair and nails. While biotin has many important functions as a chemical regulator in the body, biotin also plays an important role in biotechnology.[94] Because biotin is only 244.3 daltons, it is a relatively small molecule that can be conjugated to other proteins and molecules without significantly altering their biological activity.[94] Specifically, the streptavidin protein binds biotin with high affinity ($K_d = 10^{-14}$ mol/L) and specificity[94,95,96]. The streptavidin-biotin complex is the strongest known non-covalent interaction between a protein and a ligand.[94,95,96]

The remarkable affinity of streptavidin to biotin has been closely inspected using crystal structures.[95] First, the biotin-binding site on streptavidin highly complements the biotin shape, making for an easy fit for biotin.[95,96] In addition, there is an extensive network of hydrogen bonds formed between streptavidin and biotin once biotin is in the binding site.[95,96] Hydrogen bonds are the strongest type of non-covalent bonds found in

nature, and add to the stability of the streptavidin-biotin complex. However, the streptavidin-biotin affinity is stronger than what would be expected from the hydrogen bond interactions alone, which indicates that there are other mechanisms in place to stabilize the bond even further.[95,96] One such mechanism is that the biotin binding site is hydrophobic, and there are several hydrophobic interactions made to the biotin in the binding site that contribute to the affinity.[95,96] Finally, biotin binding is accompanied by a flexible loop that extends over the bound biotin, acting as a cover over the binding site and accounts for the very high affinity between streptavidin and biotin.[95,96]

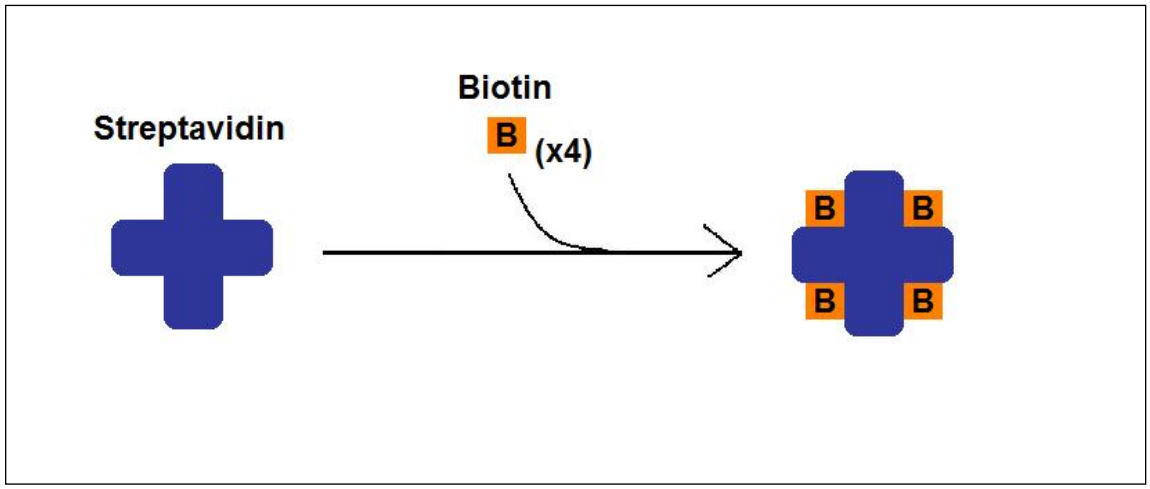

Figure 37. This diagram demonstrates that streptavidin has four biotin-binding sites. This means that each streptavidin protein can bind up to four biotin molecules. Figure is not drawn to scale.

The formation of the bond between streptavidin and biotin occurs very quickly, and once it forms, it is unaffected by extremes of temperature, pH, organic solvents, and other denaturing agents.[96] These features of the streptavidin-biotin bond are often exploited when purifying or detecting proteins conjugated to either component of the interaction.[94]

4.1.4 Complete Complex

In the context of this experiment, biotin is used to connect an antibody to streptavidin, which is attached to a nanoparticle. We used a biotinylated VCAM-1 antibody (biotin conjugated to the antibody) to attach to streptavidin to complete the final nanoparticle complex. The VCAM-1 antibody is used for specific targeting of the VCAM-1 proteins on the BBB monolayer, so that the nanoparticle is delivered in a specific manner. Each streptavidin protein has the ability to bind up to four biotin molecules, as shown in the diagram below.

In this experiment, biotin has a similar role as streptavidin does, in that biotin functions as a "glue" to connect the nanoparticle to the antibody. The biotin of the prepared biotinylated VCAM-1 antibody naturally attaches to streptavidin in solution, due to the extremely high streptavidin-biotin attraction in nature. Meanwhile, streptavidin is also attached to a CSLN, due to the electrochemical attraction between the positively charged nanoparticle and the negatively charged streptavidin. Ideally, the complete nanoparticle complex is composed of a nanoparticle conjugated to a streptavidin protein, which is subsequently attached to four biotinylated VCAM-1 antibodies, as diagrammed in the Figure 38.

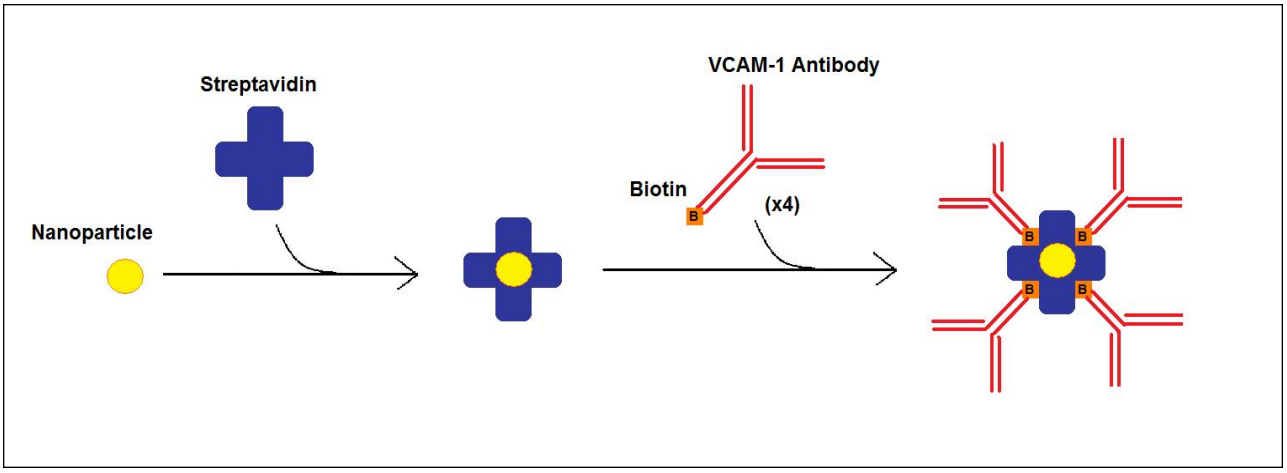

Figure 38. This diagram shows the completed drug delivery complex, which includes a cationic solid lipid nanoparticle (yellow), attached to streptavidin (blue), which is then subsequently attached to a biotinylated VCAM-1 antibody (orange, red). As evidence in the diagram, since each streptavidin has four biotin-binding sites, streptavidin can bind four biotinylated antibodies. Figure is not drawn to scale.

4.1.5 Fluorescent Dye

The dye used to visualize the nanoparticles is BODIPY® TMR maleimide. The BODIPY TMR dye is hydrophobic, which allows it to be incorporated into the hydrophobic core of CSLNs.[97] It is also lacks ionic charge, preventing it from interfering with the other charged components of the nanoparticle complex.[97] These two properties make BODIPY TMR an ideal dye for visualization of the nanoparticle complex. BODIPY TMR is also used to imitate how a real pharmacological drug would act in our drug delivery model. Since choosing and utilizing a real drug lies beyond the scope of our current project, using BODIPY TMR serves the dual purposes of visualization of the nanoparticle complex and simulation of a real drug.

BODIPY TMR peaks in fluorescence emission when it absorbs light at 570nm.[97] The dye has a green fluorescence similar to that of Fluorescein Isothiocyanate

(FITC).[97] Thus, BODIPY TMR is compatible with standard optical filter sets designed for FITC, which is standard on most microscopes that have fluorescent filters.

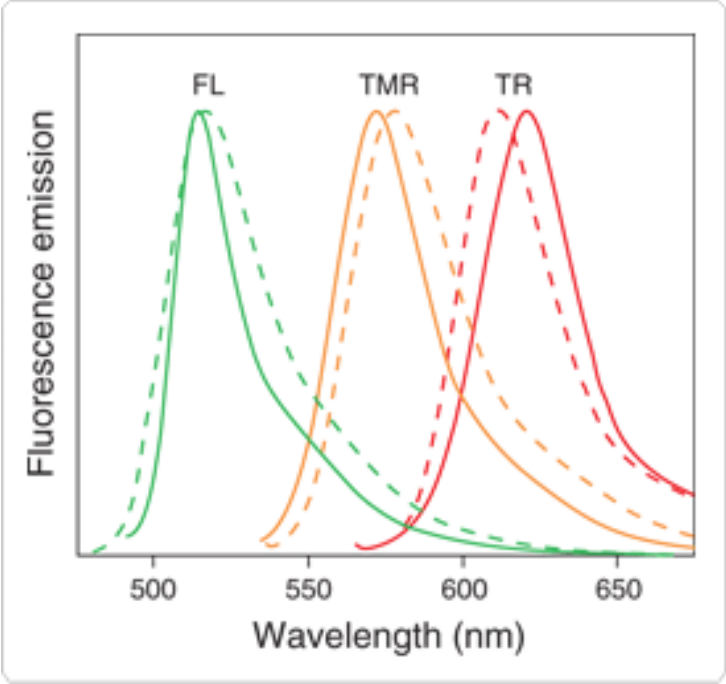

Figure 39. This figure shows the emission spectrum of BODIPY TMR. As shown in the graph, BODIPY TMR peaks in flourescence at around 570 nm.

This dye is not visually shown in the diagram of the nanoparticle complex because it will be encapsulated inside the hollow space of the nanoparticle.

4.2 Nanoparticle Complex Methodology

The nanoparticle complex with streptavidin was created in a series of two steps. The two steps were to create the nanoparticle and then attaching the streptavidin to the nanoparticle created in the first step.

4.2.1 Creating the Nanoparticle

The following compounds listed below were added into a vial of chloroform:methanol mixture (2mL, 2:1 ration per volume).

cholesteryl oleate	22.5mg, 45% w/w
glyceryl trioleate	1.5mg, 3% w/w
DOPE	7mg, 14% w/w
cholesterol	5mg, 10% w/w
DC-cholesterol	14mg, 28% w/w
BODIPY TMR dye	fluoresces at 561nm, 8uL

Afterwards, 10mL of deionized water was added to the mixture and then vortexed thoroughly.[29] The suspension was sonicated thoroughly for 16 minutes at 60Hz.[29] The micro emulsion solution left over after the sonicating was then transferred to a reduced pressure solvent removal apparatus and removed above 52 Celsius. The melting point of cholesteryl oleate is 52 Celsius. The prepared SLN emulsion was stored at 4^{o} Celsius.[29]

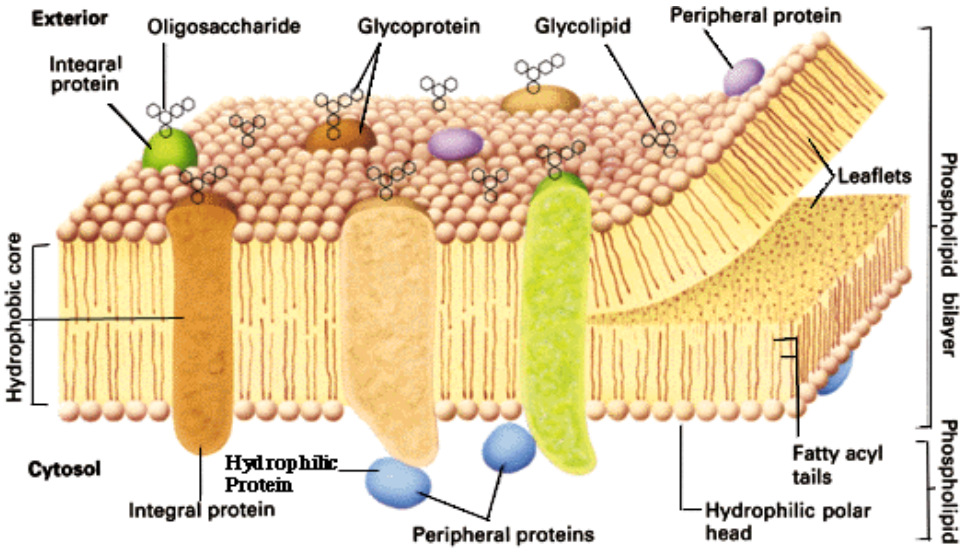

Figure 40. Typical phospholipid bilayer membrane with transmembrane proteins
AP Biology, http://www.biologycorner.com/APbiology

4.2.2 Adding Streptavidin

To create the complex with streptavidin, .5mg of streptavidin was added to 3mL of nanoparticle suspension in a vial.[29] The mixture of streptavidin and nanoparticle suspension was then sonicated for 8 minutes. The mixture of streptavidin and nanoparticle suspension was then placed into a 4 Celsius fridge for storage.[29]

4.2.3 Adding Biotinylated Antibody

To create the complex with biotinylated anti-VCAM-1, 30ug of biotinylated anti-VCAM-1 (purchased from eBioscience) and 10 mL of nanoparticle-streptavidin suspension was added in a vial. The mixture of biotinylated antibody and nanoparticle-streptavidin suspension was then sonicated for 11 minutes. The mixture of biotinylated antibody and nanoparticle-streptavidin suspension was then placed into a 4 Celsius fridge for storage.[29]

4.2.4 Confirmation of the Nanoparticle Complex

In order to confirm whether the nanoparticle and streptavidin has been attached, a series of four experiments were conducted in the following order below:

1. Nanoparticles and streptavidin on glass microscope slides were coated in a layer of biotin plates that were purchased from Xenopore.
2. Nanoparticles and streptavidin on non-biotin plate.
3. Nanoparticles on biotin plates.
4. Nanoparticles on non-biotin plates.

For each of the experiments listed above, 85uL of nanoparticle suspension was placed on a plate.[29] After waiting 2 minutes, the suspension on the plate was washed under de-ionized water and dried with Kim wipes in order to view the complex under 20x objective microscope with fluorescent filter 561nm.

All of the images collected from the experiments listed above were analyzed with ImageJ.

4.3 Nanoparticle Complex Data and Results

4.3.1 Maximize NP Size Uniformity and Reduce Contamination via Filtering

4.3.1.1 Unfiltered Nanoparticles

As shown in Figure 41 below**,** the nanoparticles initially formed were of non-uniform size and shape. Using ImageJ for analysis, an average particle size was determined for each individual picture, as well as the standard deviation for the distribution of particle size within each picture. In order to increase the likelihood that the program was recognizing individual nanoparticles rather than conglomerations of

particles or other contaminates that may have been on the slide, only particles with a circularity (defined by $4\pi(A/C^2)$, where A equals area of the circle and C equals circumference of the circle. A value of 1.00 denotes a perfect circle) of 0.99–1.00.

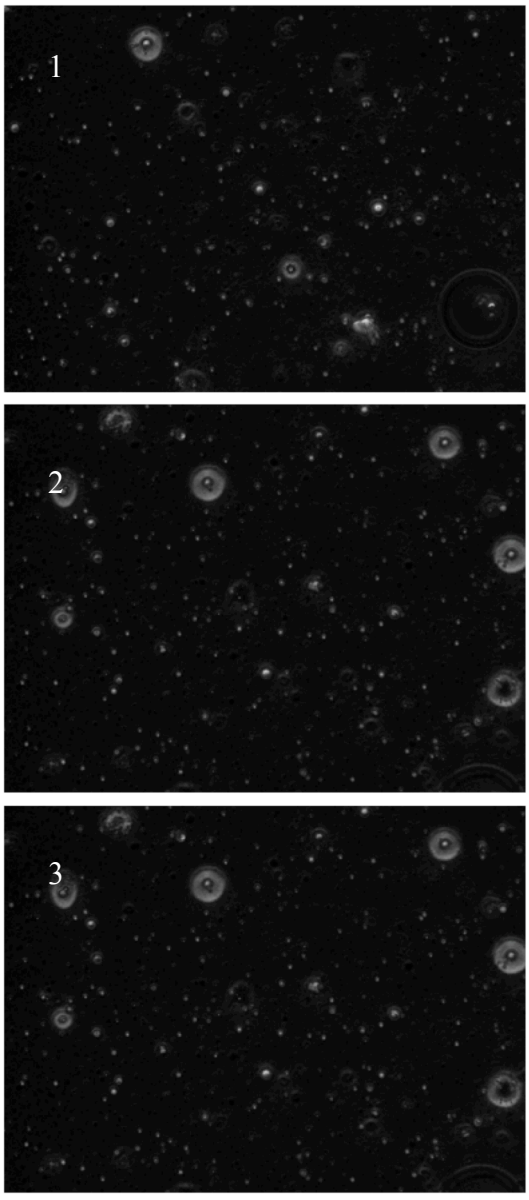

Figure 41 shows three separate photos of the nanoparticles before filtering. These same photos were later used for comparison to the filtered nanoparticles.

Due to the limitations of ImageJ, along with issues with the equipment used to obtain the pictures, it cannot be assumed that the average particle size is only taking into account the sizes of nanoparticles themselves. The ImageJ analysis has been used as a comparison between the filtered and unfiltered nanoparticles, not as a definitive measure of nanoparticle size.

The particles in Figure 41.1 were found to have an average particle size of 381.4 nm, after the removal of extreme outliers from the data (Extreme outliers defined as particles more than 3 standard deviations from the mean as calculated by ImageJ). The distribution of particle size can be seen in Figure 43.1. The particles in Figure 31.1 have a fairly wide distribution. The particle sizes

range from 100.6 nm to 5027.6 nm, with continuous peaks between 100.6 nanometers and 1907.1 nanometers.

The particles in Figure 41.2 were found to have an average particle size of 282.4 nm, after the removal of extreme outliers from the data. The distribution of particle size can be seen in Figure 43.2. The particles in Figure 41.2 have a fairly wide distribution. The particle sizes range from 100.6 nm to 4625.4 nm, with continuous peaks between 100.6 nanometers and 2061.3 nanometers.

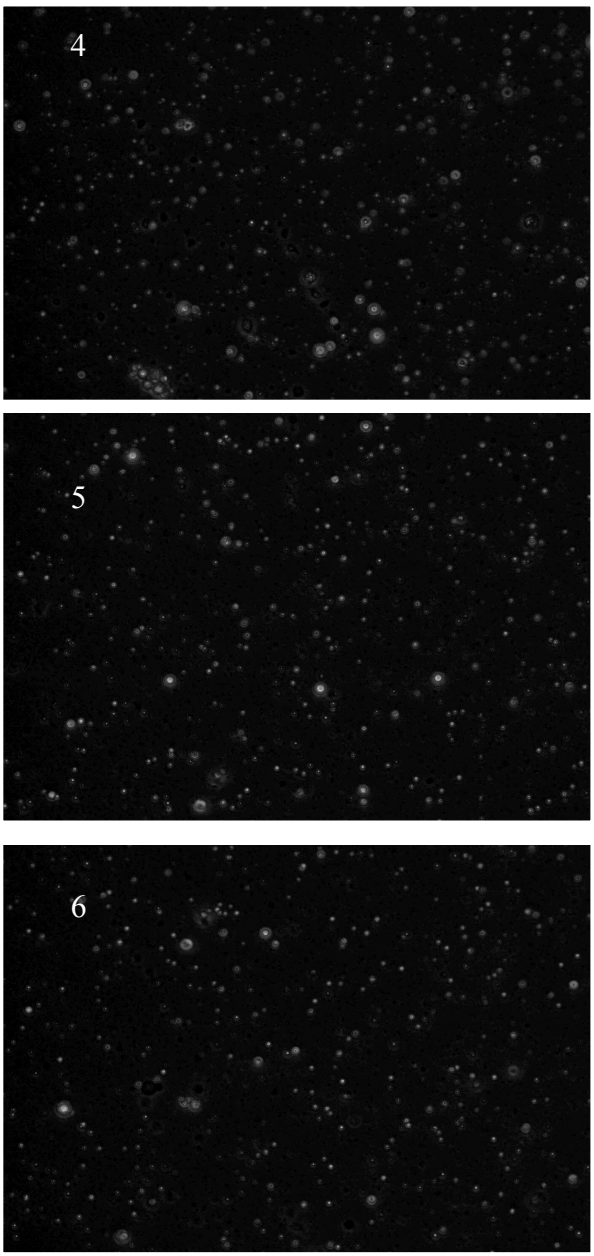

The particles in Figure 41.3 were found to have an average particle size of 203.2 nm, after the removal of extreme outliers from the data. This lower average as compared to the other filtered samples may be attributed to issues with the image quality in the format needed for ImageJ analysis. The distribution of particle size can be seen in Figure 43.3. The particles in Figure 41.3 have a slightly smaller distribution than the other unfiltered nanoparticle samples. The particle sizes range from 100.6 nm to 2815.5 nm, with continuous peaks between 100.6 nanometers and 1729.5 nanometers.

Figure 42 shows three separate photos of the nanoparticles after filtering. These same photos were later used for comparison to the filtered nanoparticles.

4.3.1.2 Filtered Nanoparticles

The particles in Figure 42 were passed through a 200 nm filter in order to produce particles of a more uniform size and of a more optimal size with which to cross the BBB.

The particles in Figure 43.4 were found to have an average particle size of 305.3 nm, after the removal of extreme outliers from the data. The distribution of particle size can be seen in Figure 43.4. The particles in Figure 42.4 have a more narrow distribution that the majority of the unfiltered nanoparticles. The particle sizes range from 100.6 nm to 3720.4 nm, with continuous peaks between 100.6 nanometers and 1789.8 nanometers. These peaks are much shorter on average than those from the distribution the unfiltered particles.

The particles in Figure 42.5 were found to have an average particle size of 211.7 nm, after the removal of extreme outliers from the data. The distribution of particle size can be seen in Figure 43.5. The particles in Figure 42.5 have a more narrow distribution that the majority of the unfiltered nanoparticles. The particle sizes range from 100.6 nm to 1508.3 nm, with peaks between 100.6 nanometers and 663.6 nanometers, though they are not continuous.

The particles in Figure 42.6 were found to have an average particle size of 257.5 nm, after the removal of extreme outliers from the data. The distribution of particle size can be seen in Figure 43.6. The particles in Figure 42.6 have a more narrow distribution that the majority of the unfiltered nanoparticles. The particle sizes range from 100.6 nm to 4122.6 nm, with continuous peaks between 100.6 nanometers and 1141.3 nanometers. These peaks are much shorter on average than those from the distribution the unfiltered particles, with the large majority of particles being less than 502 nm.

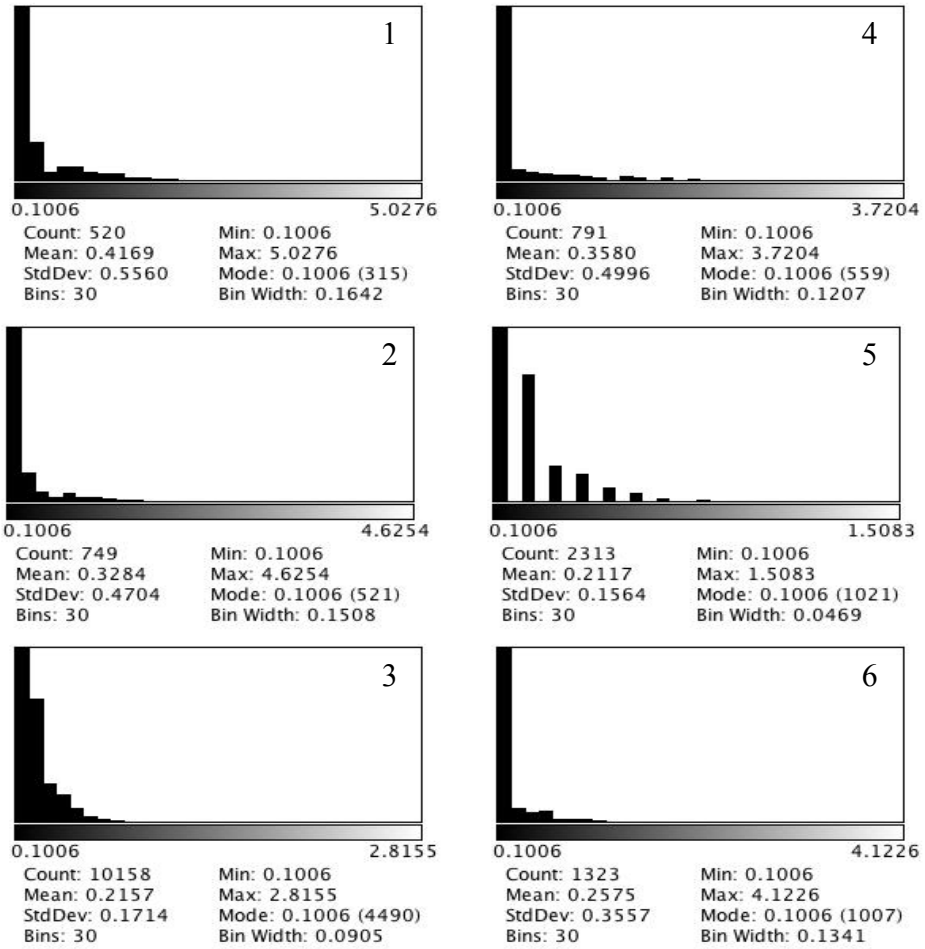

Figure 43 shows the size distribution of the nanoparticles imaged in Figures 41 and 42. Figures 1-3 are of the unfiltered nanoparticles, and Figures 4-6 are of the filtered nanoparticles. The x-axis is the size of nanoparticles in micrometers for all graphs; the y-axis is the number of nanoparticles, for all graphs.

4.3.2 Test that the Nanoparticle can Attach to Streptavidin

The purpose of this experiment was to demonstrate that the CSLNs were able to successfully bind to streptavidin. Samples of nanoparticles and nanoparticle-streptavidin conjugates were placed on both normal microscope slides and biotin-coated slides. The slides were then washed, leaving behind particles that were the most adherent to the

slides. The slides were then observed under fluorescence microscopy to determine whether the samples successfully attached to the slides.

Condition	Average Number of Particles per Frame	
	Trial 1	Trial 2
NP on biotin-coated slide	1.1	1.3
NP on normal slide	0.1	0.2
NP-Strep on biotin-coated slide	24.7	19.9
NP-Strep on normal slide	4.3	0.2

Table 4. Counting nanoparticles

Ten pictures were taken for each trial, with each photograph illustrating a different field of view. The average number of particles in each frame per condition was calculated and recorded in Table 4.

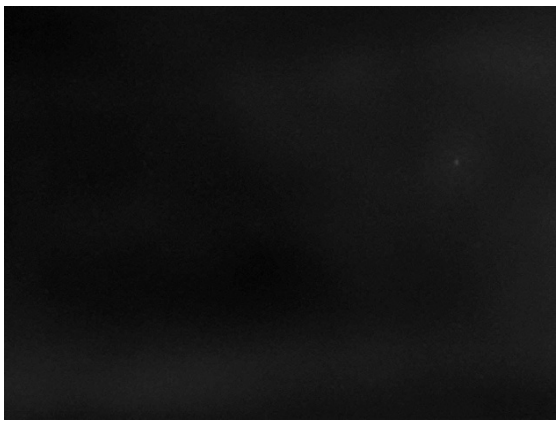

Figure 44. NP on biotin-coated slide

Figure 45. NP on normal slide

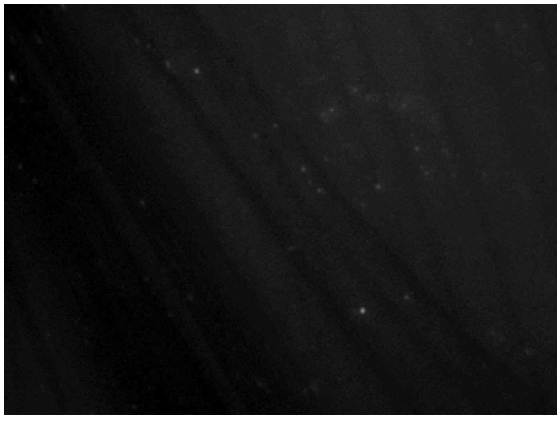

Figure 46. NP-strep on biotin-coated slide

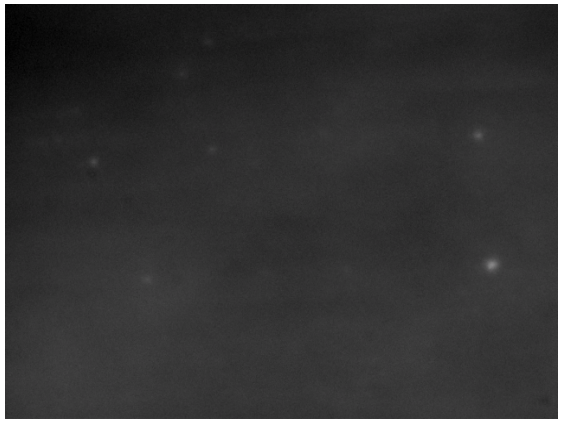

Figure 47. NP-strep on normal slide

Figures 44-47 are photographs selected from each condition of the experiment. Each figure was selected to best represent the relative averages particles listed in Table 4. Figure 45 is a photograph of a nanoparticles on a biotin-coated slide, and there is 1 particle in view. Figure 45 is a photograph of nanoparticles on a normal slide, and there are no particles in view. Figure 46 is a photograph of nanoparticle complexes on a biotin-coated slide, and there are 30 particles in view. Figure 47 is a photograph of nanoparticle complexes on a normal slide, and there are 6 particles in view.

4.3.3 Test that Streptavidin can Attach to Biotin

The following results are from an experiment to validate that streptavidin is able to attach to biotin. We hypothesized that fluorescence and the number of nanoparticles observed in each image will decrease the longer the incubation time.

Images after 2 hour incubation:

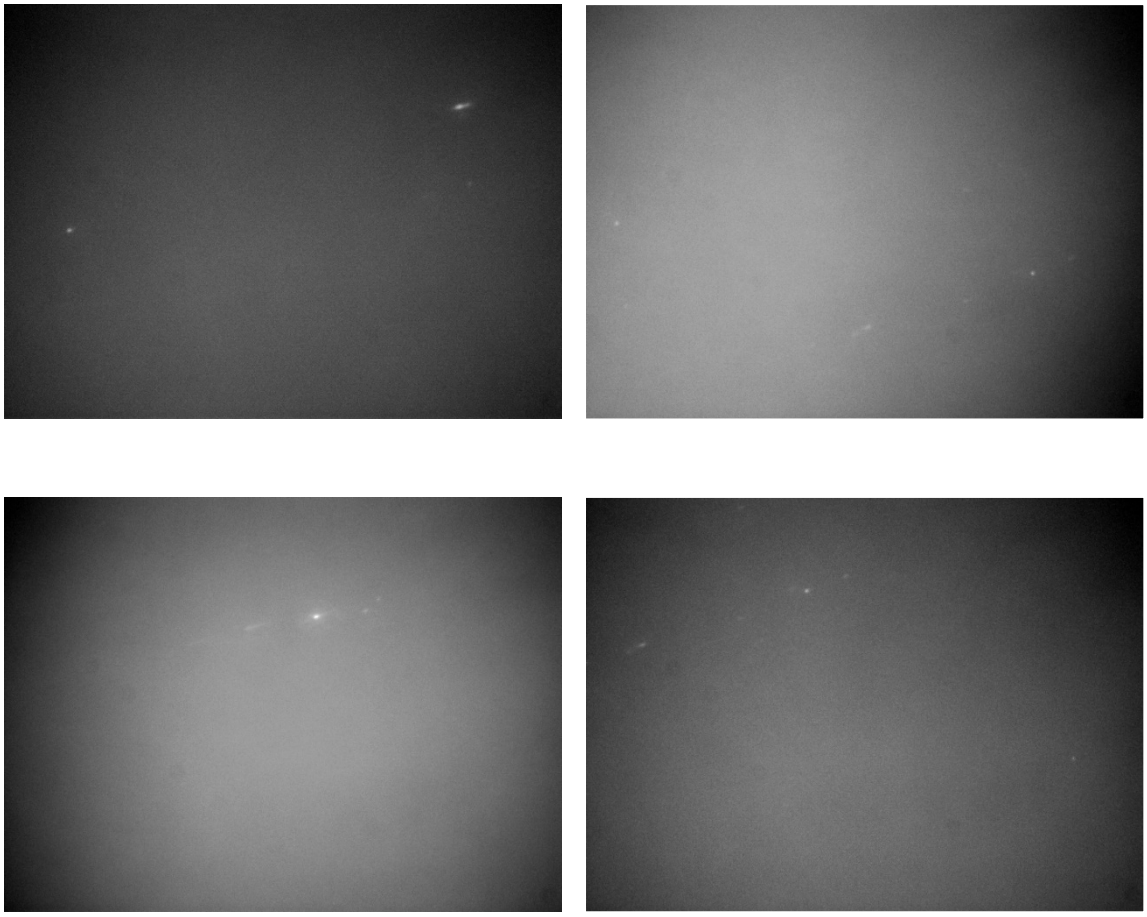

Images after 4 hour incubation:

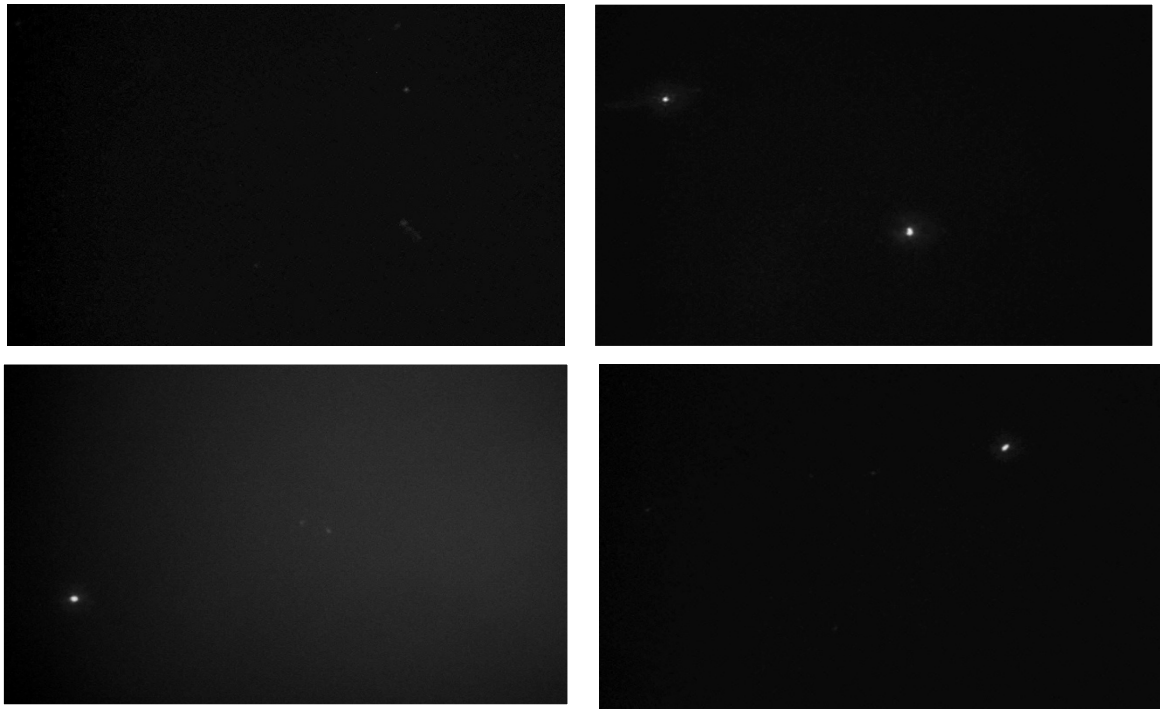

Images after 8 hour incubation:

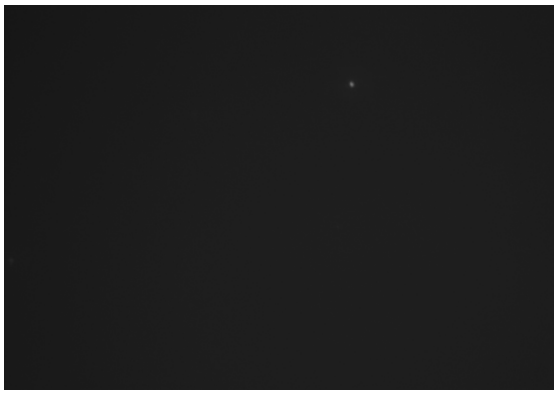

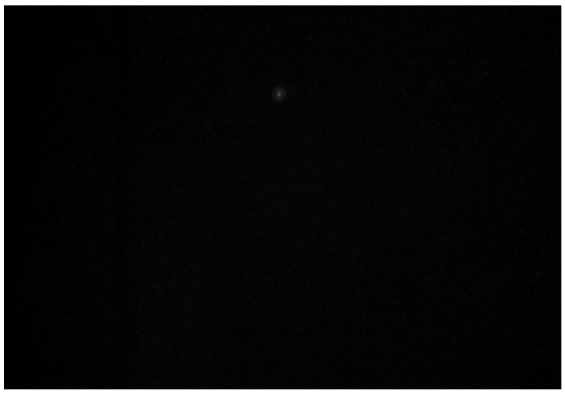

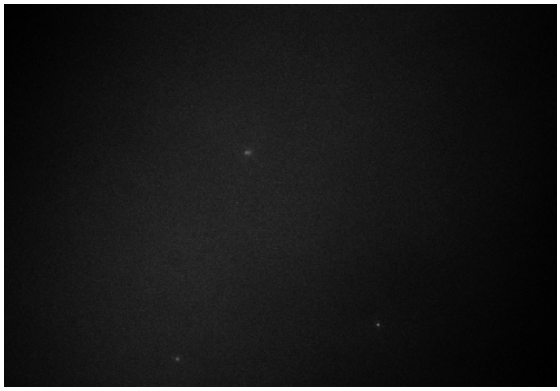

The following chart reveals the number of fluorescent nanoparticles observed in each image, at each time point of incubation.

Number of fluorescent nanoparticles observed in each image			
Time point	2 hour	4 hour	8 hour
	3	4	4
	7	2	1
	4	5	3
	6	3	1
Average	5	2.8	1.8

Table 5. Counting fluorescent nanoparticles. As evidenced by the decreased number of nanoparticles observed on average in each image as length of incubation increased, this experiment confirms that streptavidin is able to attach to biotin.

4.3.4 Determining the Concentration of Nanoparticles in Solution

After pipetting 20 μL of nanoparticle solution onto a microscope slide, we laid a cover-slip on top of the droplet such that the droplet covered the entire face of the cover-slip. We proceeded to take fourteen images of the nanoparticles in random places at 20x magnification using fluorescence microscopy. We used the following fourteen images (as shown below) to determine the concentration of nanoparticles in solution.

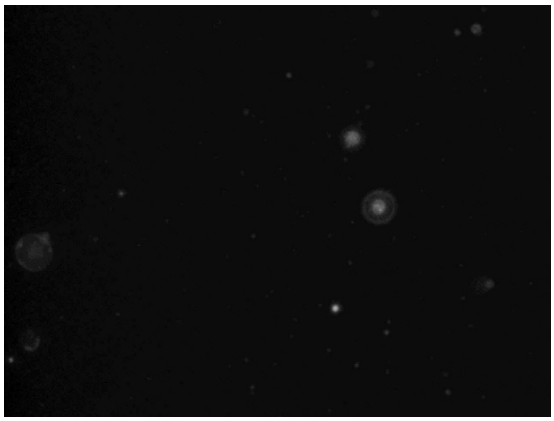
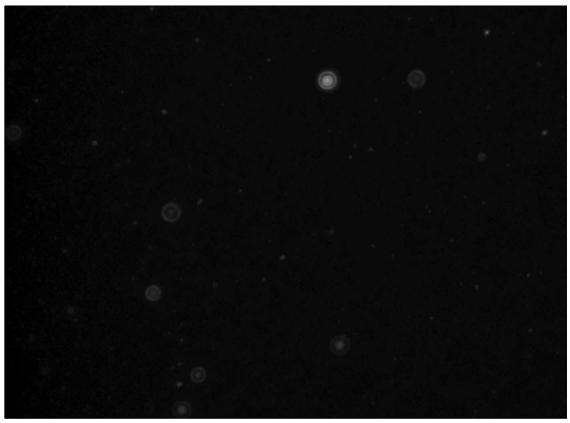

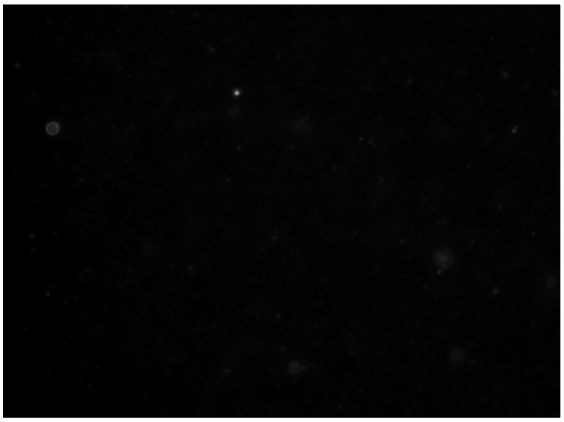
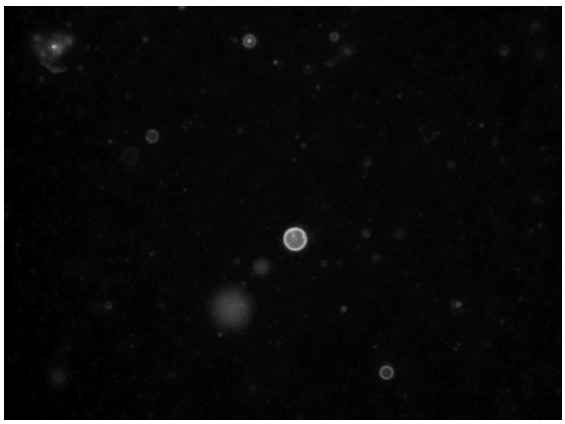
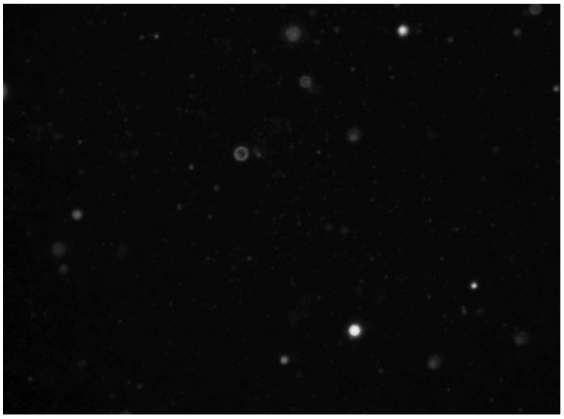

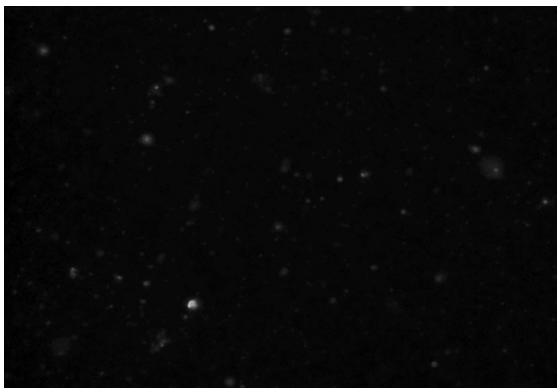
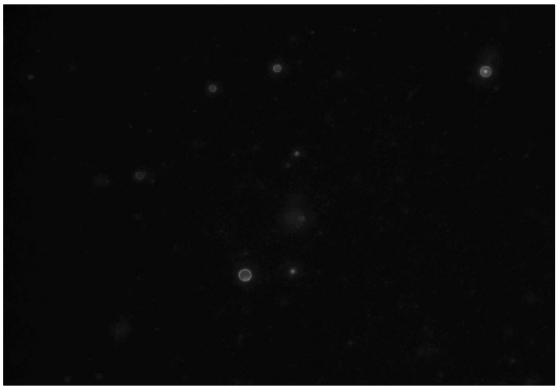
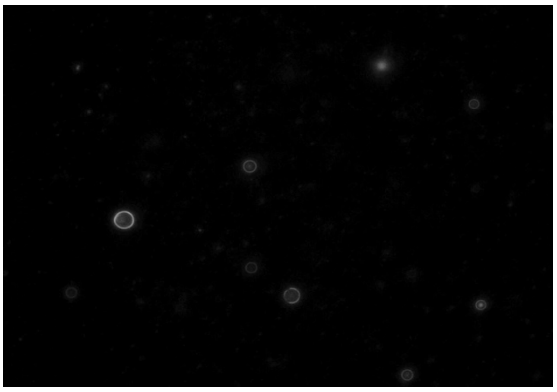
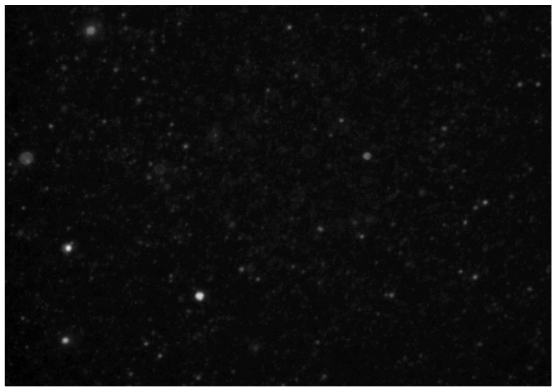
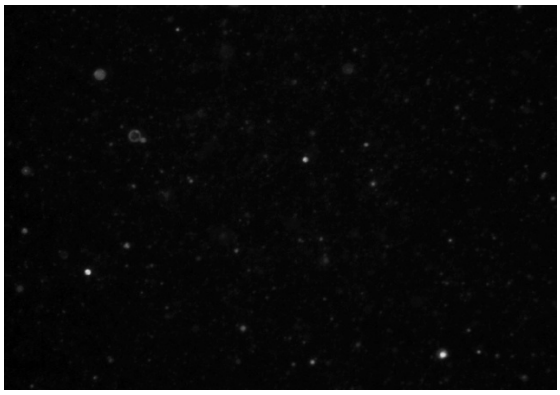
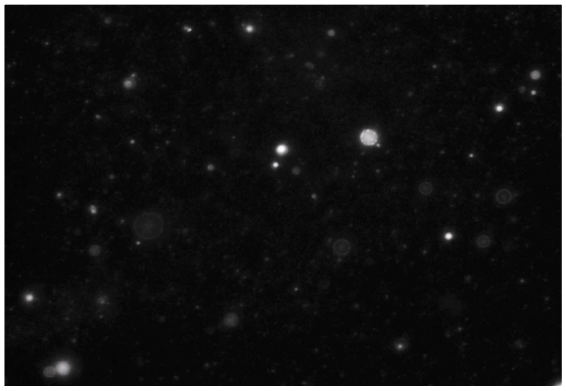
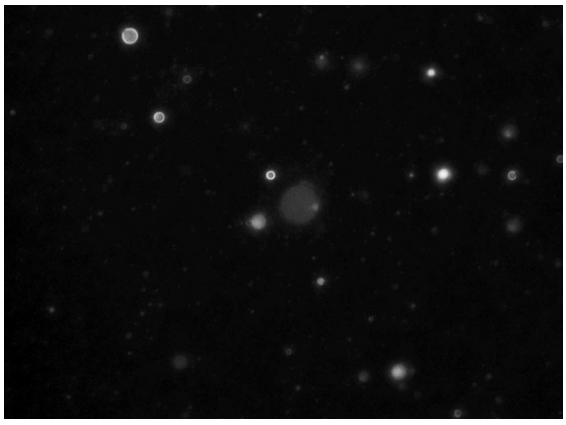
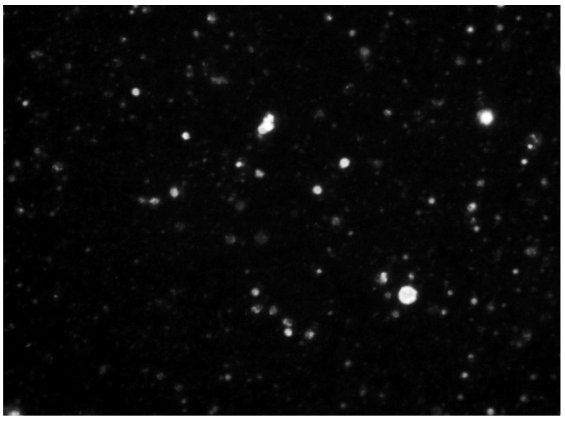

We then counted the number of fluorescent particles that appeared in each image, took the average, and proceeded to calculate the concentration of the nanoparticle solution from there.

Picture #	Nanoparticles
1	7
2	9
3	1
4	5
5	21
6	22
7	38
8	13
9	17
10	68
11	67
12	34
13	24
14	73
Average	28.5

Table 6. This table displays the number of fluorescent particles counted in each of the fourteen images shown above, under fluorescent microscopy.

The average number of nanoparticles observed was 28.5 nanoparticles per image. Based on the magnification of 20x and the 0.3171 μm/pixel scale of the microscope, each image was determined to have the dimensions of 441.4×10^{-6} m by 329.78×10^{-6} m through ImageJ analysis. This means that each image had an area of 0.14556×10^{-6} m^2, or 0.14556 μm^2. So rudimentarily, there are 28.5 nanoparticles per 0.14556 μm^2. Each coverslip has dimensions of 20×10^{-3} m by 20×10^{-3} m, which yields an area of 400 um^2 for each coverslip. Since each image had an area of 0.14556 μm^2, this means that dividing the area of each coverslip by the area of each image would yield the number of images that could fit onto one coverslip: 400 μm^2 / 0.14556 μm^2 = 2748.008

images/coverslip. To determine how many nanoparticles existed on one coverslip, we multiplied 28.5 nanoparticles/image by 2748.008 images/coverslip to yield 78,318.22 nanoparticles/coverslip. Each coverslip contained 20 μL of nanoparticle solution, so 78,318.22 nanoparticles / 20 μL solution = 3915.9 nanoparticles/ μL. The concentration of our nanoparticles is roughly 3900 nanoparticles per μL. We recognize that this method of determining our nanoparticle concentration is not precise, but this method does provide us with a rough estimation that is sufficient for the purposes of our project.

4.4 Nanoparticle Complex Discussion

4.4.1 Maximize NP Size Uniformity and Reduce Contamination via Filtering

Once the nanoparticles had successfully formed, pictures were taken using the ImageJ software. The images were taken for several reasons: to further confirm the formation of the nanoparticles and to determine the size of the formed nanoparticles. Due to the limitations of ImageJ and "noise" present in the pictures used for analysis, the average areas obtained can only be used for comparison between the two sets of nanoparticles.

	Sample 1	Sample 2	Sample 3	Average	Standard Deviation
Unfiltered Nanoparticles	381.4	282.4	203.2	289	+/- 89.3
Filtered Nanoparticles	305.3	199	221.1	241.8	+/-56.1

Table 7. Average nanoparticle area in each sample after the removal of extreme outliers from the data, as well as overall averages and standard deviations between the average particle sizes

As shown in Table **7,** the filtered nanoparticles have a lower average area than the unfiltered particles. These results show that overall, the size of the nanoparticles decreased after the unfiltered particles were passed through the 0.200 μm filter. A smaller particle size is favorable to permeating the BBB model because a smaller particle will more easily sift through the physical membrane. Thus, a smaller particle size increases the likelihood that the drug complex will be capable of passing through the BBB model. Table **7** shows the standard deviation of the average areas of the filtered and unfiltered nanoparticles. The unfiltered nanoparticles have an average size of 289 nm +/- 89.3. The filtered nanoparticles have an average size of 241.8 nm +/- 56.1. The smaller standard deviation in the areas of the filtered particles indicates that more of the particles are closer to the average size. From this it can be concluded that the nanoparticles are of a more uniform size once they have been passed through the filter.

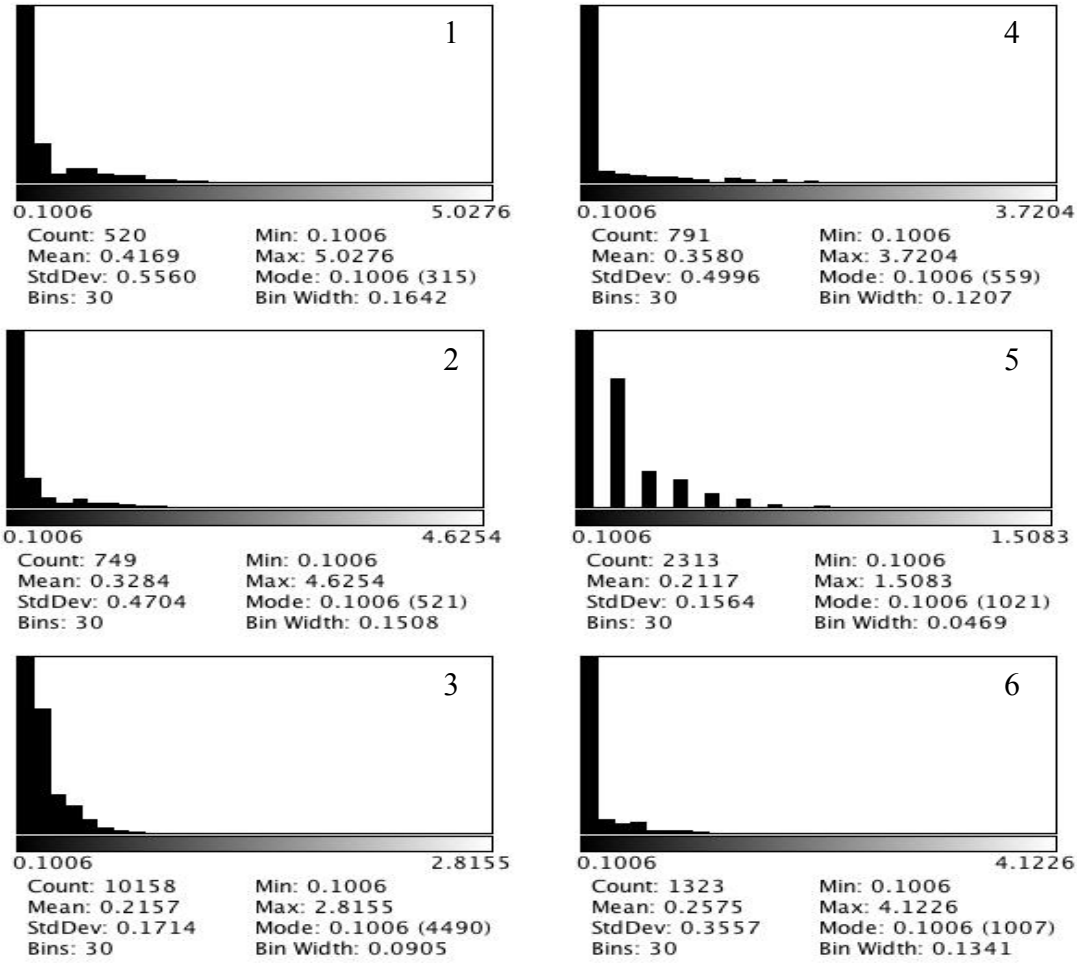

Figure 48. S distribution of the nanoparticles before and after filtering. Figures 1-3 are of the unfiltered nanoparticles, and Figures 4-6 are of the filtered nanoparticles. The x-axis is the size of nanoparticles in micrometers for all graphs; the y-axis is the number of nanoparticles, for all graphs.

Figure 48 shows the size distribution of the filtered and unfiltered nanoparticles. On average, the filtered nanoparticles have a higher percentage of particles which are of a smaller size. The unfiltered nanoparticles have more individual particles of higher sizes. These distributions further support the conclusion that filtering the nanoparticles result in nanoparticles of a more uniform size, and increases the likelihood of the nanoparticles passing through the BBB model.

4.4.2 Test that the Nanoparticle can Attach to Streptavidin

When nanoparticles and nanoparticle conjugates are placed on slides and subsequently washed off, the particles that remain are those that successfully bound to the surface of the slides. A larger number of particles adhering to the microscope slides indicates stronger intermolecular interactions between the particles and the surface of the slides. This is because stronger interactions cause more particles to adhere to the slide despite the slide being washed.

According to Table 7, in both trials, nanoparticle-streptavidin conjugates on biotin-coated slides yielded by far the largest result of the four conditions tested. This suggests that the CSLN successfully attached to streptavidin, as the strong streptavidin-biotin interaction allowed more nanoparticle-streptavidin conjugates to attach to the biotin-coated slides. The control conditions in which nanoparticles were tested on biotin-coated and normal slides yielded close to 0 particles. This further confirms that the CSLN successfully attached to streptavidin. This is because these results demonstrate that the nanoparticles themselves are incapable of attaching to the slides. Thus, the vast majority of the fluorescent particles visible in the pictures of nanoparticle-streptavidin complex on biotin-coated slides are the result of the CSLNs successfully attaching to streptavidin, allowing the fluorescent nanoparticles to adhere to the biotin-coated slides through streptavidin-biotin interactions.

However, in Trial 1, nanoparticles-streptavidin on normal slides yielded a larger average number of particles per frame than expected. This condition resulted in 4.3 particles per frame, while the other two control conditions resulted in 1.1 and 0.1 particles per frame. This is not the case in Trial 2 though, as the nanoparticles-

streptavidin on normal slides yielded 0.2 particles per slide, which is close to 0 as expected. A possible explanation for this is that the glass slide used in Trial 1 was accidentally rubbed at some point, giving the slide a net charge. Because both CSLNs and streptavidin are charged, the charge on the glass slide may have caused the nanoparticles-streptavidin conjugates to attach via electrostatic interactions.

4.4.3 Test that Streptavidin can Attach to Biotin

The purpose of this experiment was to validate and confirm that the streptavidin could indeed attach to biotin. Even though it is known throughout scientific literature that streptavidin and biotin have the strongest non-covalent attractive force that exists in nature, we wanted to make sure that was true in our experimental settings. In this experiment, we incubated the nanoparticle-streptavidin complex with excessive free biotin, added it to biotin-coated microscope slides, and observed the amount of nanoparticle-streptavidin complex that bound to the biotin-coated slides under fluorescent microscopy at two, four, and eight hour time points. The thought behind our experiment was that since streptavidin has four biotin-binding sites, the more we incubate the streptavidin with excess biotin, the more biotin-binding sites on streptavidin will be occupied, so the less chance that streptavidin can adhere to the biotin-coated slides (because all the biotin-binding sites on streptavidin would have been occupied by the free biotin). Essentially, our experiment is based on the principles of saturation. We predicted that the longer we saturate the nanoparticle-streptavidin complex, the less fluorescence will be observed on the biotin-coated slides, due to the decreased adherence of the nanoparticle-streptavidin complex on the biotin-coated slides.

Images under fluorescent microscopy at hour two after initial incubation yielded an average of 5 fluorescent complexes per image. In contrast, images under fluorescent microscopy at hour four after initial incubation yielded on average 2.8 fluorescent complexes per image, while images at hour 8 had on average 1.8 fluorescent complexes per image.

The number of fluorescent complexes per image observed at hour four compared to hour two decreased by nearly 50%, and the number of fluorescent complexes per images observed at hour eight compared to hour two decreased by about 64%. We consider these to be significant results because we understand that within two hours, much of the biotin-binding sites on streptavidin would already have been occupied by the free biotin. There is still a significant difference in fluorescence observed among the two, four, and eight hour time points and that is a significant result. With these results, we confirm that the streptavidin and biotin we purchased do bind to each other in an attractive manner. Thus, these results indicate that the streptavidin/biotin portion of our ultimate nanoparticle complex will adhere and connect as expected.

4.4.4 Determining the Concentration of Nanoparticles in Solution

The purpose of determining the concentration of nanoparticles in our nanoparticle solution was so that we could determine the appropriate ratios of streptavidin and biotin to add to make the complex in order to maximize the number of nanoparticle complexes we would create. To determine the concentration of the nanoparticles in solution, we began by taking images of the nanoparticles under fluorescent microscopy. We took images in random locations on the microscope slides, so that we would receive an even

representation of the total slide. After taking into account the size of the microscope coverslip, the real size of each image, and how many nanoparticles we originally plated onto the microscope slide, we determined through several mathematical calculation that we have 3915.9 nanoparticles/μL, or roughly 4000 nanoparticles/μL.

5. Nanoparticle Complex with BBB Model

5.1 Nanoparticle Complex with BBB Model Methodology

In this stage of the experiment, both the BBB model and nanoparticle complex were completed and ready to be tested together to see the level of nanoparticle complex permeation through the BBB model. The non-complexed nanoparticle and the full-complexed nanoparticle were each tested against the HUVEC monolayers with varying TNF-α, and the aggregation of nanoparticles after 1 hour and 5 hour incubation was imaged using phase and fluorescent microscopy.

HUVEC cells were cultured until the fourth passage, after which they were plated onto fibronectin-coated, glass coverslips to produce 6 fully confluent HUVEC monolayers. To simulate varying degrees of inflammation in the brain, different levels of TNF-α were added to individual coverslips, specifically 0μg/mL, 2μg/mL, 20μg/mL of TNF-α. TNF-α was added to the fully confluent HUVEC coverslips 18 hours prior to the addition of non-complexed nanoparticle control. Two coverslips had 0μg/mL TNF-α (non-diseased state), two coverslips had 2μg/mL TNF-α, and another two coverslips 20μg/mL TNF-α. After 18 hours, the cells were washed with 2 mL of HUVEC media. 2 mL of fresh media was added to each coverslips, followed by 25μL of non-complexed nanoparticle solution (4000 nanoparticles/μL). The coverslips were placed in a 5% CO2 incubator at 37°C. Three coverslips (0μg/mL, 2μg/mL, and 20μg/mL of TNF-α) were examined after a one hour nanoparticle incubation at 37°C in a 5% CO_2 environment. The coverslips were imaged underneath phase and fluorescent microscopy to observe the aggregation of nanoparticles around the HUVEC cell monolayer. For each individual well, multiple images were taken of randomly chosen locations on the monolayer, using

both phase and fluorescent microscopy under 10x magnification. Phase images were captured at 250 ms exposure, and fluorescent images were captured at 100 ms exposure. Three additional wells (0μg/mL, 2μg/mL, 20μg/mL of TNF-α) were examined after a 5 hour nanoparticle incubation at 37°C in a 5% CO_2 environment.

The same protocol was performed using the full nanoparticle complex, which included the streptavidin and biotinylated antibody attached to the nanoparticle. Images taken from both the control and experimental trials were observed and compared at their respective time points.

5.2 Nanoparticle Complex with BBB Model Data and Results

5.2.1 Nanoparticle Control Results

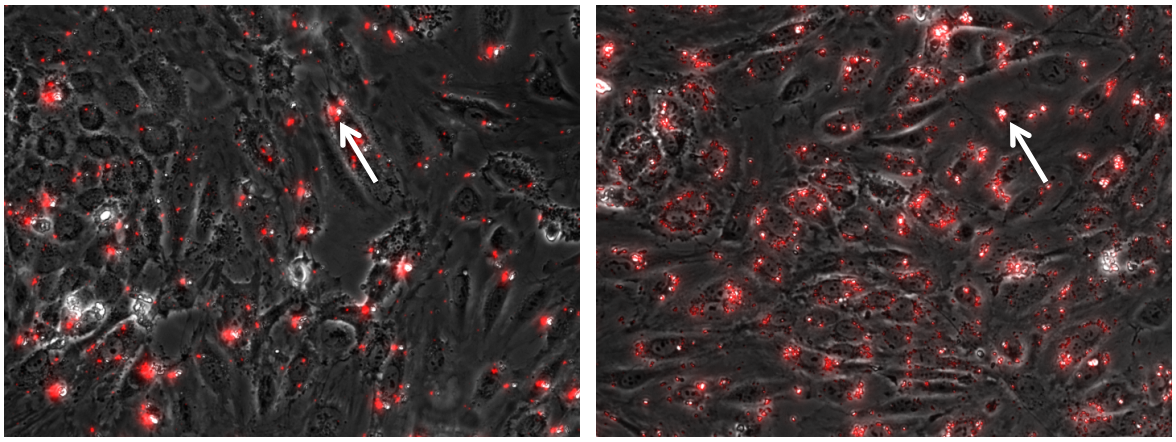

Figure 49. Composite images of bare nanoparticle absorption by HUVECS when incubated with no TNF-α at 1 hour (left) and 5 hours (right). Absorption greatly increases with time, with many more fluorescent points. Red fluorescence indicated the bare nanoparticle, as seen with the arrows.

Images were analyzed using a combination of ImageJ and MATLAB in order to characterize fluorescence emitted by the nanoparticle. Fluorescence resulting from the nanoparticles is combined with the phase images to observe localization of nanoparticle absorption. These results are used to compare nanoparticle absorption with the non-

specific bead absorption kinetics as a way to differentiate kinetics and mechanisms. Also, the results are useful in determining the efficacy of targeting VCAM-1 using CSLNs.

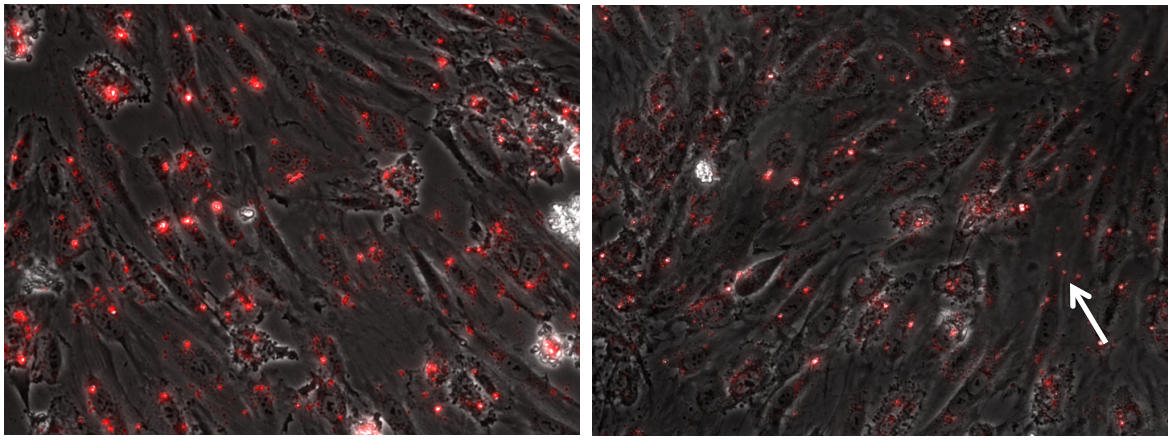

Figure 50. Composite images of bare nanoparticle absorption by HUVECS when incubated with 2 µg/mL TNF-α at 1 hour (left) and 5 hours (right). The 5 hour case seems anomalous with a visual decrease in fluorescence, as seen by less dense fluorescence at points like the one denoted by the arrow.

The first set of experiments is the control: the nanoparticle without anti-VCAM incubated with HUVECs. The two time points match the bead experiments. On initial visual inspection, the one hour time point for each level of TNF-α shows low levels of nanoparticle absorption, less so than non-specific bead absorption. Fluorescence is clearly visible, indicating that the fluorescent signal is distinguishable from the background. Among the three samples taken at each level of TNF-α, each has a clear drop in fluorescence once the MFIs are taken into account. With no TNF-α present, the MFI is 3.3 averaged across 4 groups, as seen in Figure 49. However, there is a single point that was an outlier, with the MFI of 1 instead of 3 or 4. Removing the outlier, the MFI average for the three samples becomes 4. The trend in fluorescence in the presence of TNF-α is more or less the same as previous experiments. When observing HUVECs incubated in 2 µg/mL TNF-α, the MFI is 3.8 for 3 groups (Figure 50), but at 20 µg/mL

the MFI drops back to 3.3 (Figure 51). This result is not unsurprising given the results from the bead experiments, where the MFI for the 20 µg/mL is lower than the 2 µg/mL sample. The MFIs correspond to a decrease of approximately 7.2x and 6.6x in fluorescence as compared to the bead experiments. Since the nanoparticles and beads are not directly comparable, the difference in magnitude is less important than the trends in absorption.

Some of the same trends from the bead experiments carry over besides the fluorescence intensity trends. The increasing levels of TNF-α yields similar effects on the cell layer when inspecting the phase images. Disruption is evident especially in the 2 µg/mL sample where there are many gaps in the cell layer not present in the 0 µg/mL sample. The same can be said for the 20 µg/mL sample, although the relative size of the gaps is hard to determine from the phase images. Arguably, the 20 µg/mL sample actually shows slightly less disruption in the cell layer. Some of the cell morphology is changing under the combined conditions of the TNF-α and nanoparticle.

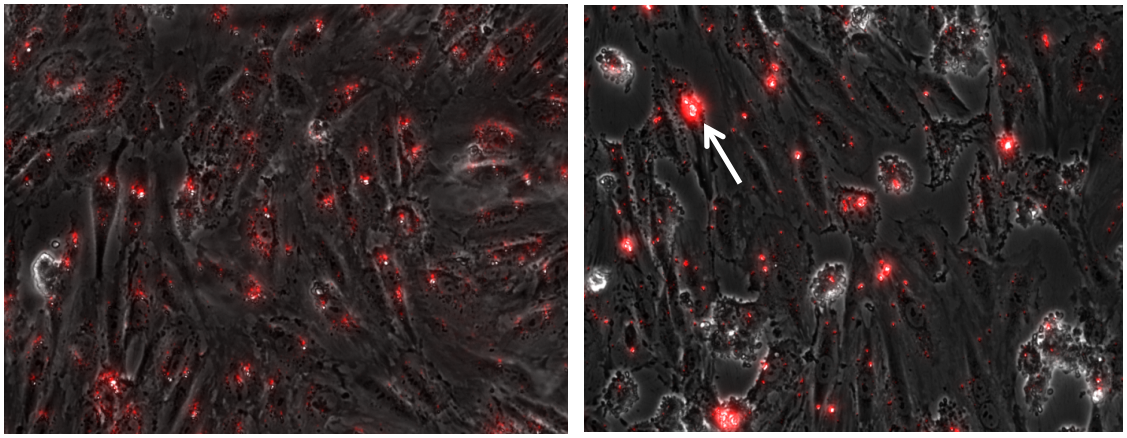

Figure 51. Composite images of bare nanoparticle absorption by HUVECS when incubated with 20 µg/mL TNF-α at 1 hour (left) and 5 hours (right). The 5 hour case shows denser fluorescence in certain areas but not necessarily more throughout as compared to the control case, such as the area denoted by the arrow.

The five hour time point shows more fluorescence, as expected, but once again not to the degree of non-specific absorption. Visually, there is an increased number of nanoparticle clusters in the 0 μg/mL sample. This indicates that during the initial incubation period, not many cells absorb the nanoparticles. Also, the fluorescence at these clusters is increasingly bright. Over time not only do cells absorb more, as expected, but also more cells absorb the nanoparticle based on these images.

When the cells are not incubated with TNF-α, the resulting MFI is 7.6, an increase of 2.3x over the four hours. Each sample has 3 trials. The increase is in line with the non-specific bead absorption kinetics, implying that absorption kinetics are similar but differ by a constant. In other words, the magnitude of absorption is lower with the bare nanoparticles, but the rate of change of absorption is similar to the beads.

There is a degree of uncertainty in the results once TNF-α is added. Visually, the fluorescence at 2 μg/mL is much lower than the other two levels, and even on par with the one hour time point. The drop is seen across all three samples taken at 2 μg/mL. As all three samples are taken from the same set of cells, it is likely that the cells were sub-optimal in some way, causing all results taken from the well to be distorted.

The MFI of the 2 μg/mL sample is only 4.1, showing that the drop in visual fluorescence is substantiated by the overall mean of the pixel intensities. The MFI is 5.9 for the 20 μg/mL sample, a slightly better result but still not matching the sample without any TNF-α. The increase between time points is only 1.8x in this case, a drop from the previous experiment which typically saw increases greater than 2x.

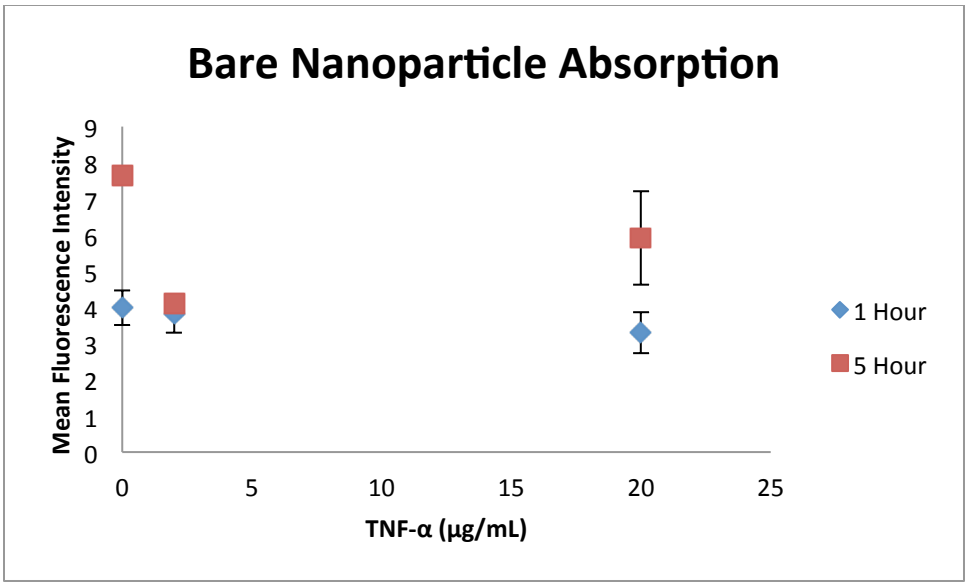

Figure 52. Bare nanoparticle absorption trend in relation to TNF-α. There is a general decrease in fluorescence compared to TNF-α, although not as noticeably logarithmic as in the bead absorption.

Some of the trends are still in play. Overall there was a decrease in nanoparticle absorption in relation to TNF-α, as seen in Figure 52. This is similar to the bead absorption. For the data without the outlier, there is a clear decrease at the 1 hour time point between the 2 and 20 µg/mL samples, with only a small difference between the 0 and 2 µg/mL samples. For the 5 hour, the differences are thrown off slightly by the anomalous data points for the 2 µg/mL sample. Regardless, we are not necessarily seeing a logarithmic decrease in absorption this time, but this could potentially be due to small sample sizes used. There is the possibility that these results reflect a similarity of the absorption kinetics in the presence of TNF-α.

5.2.2 Nanoparticle Complex Results

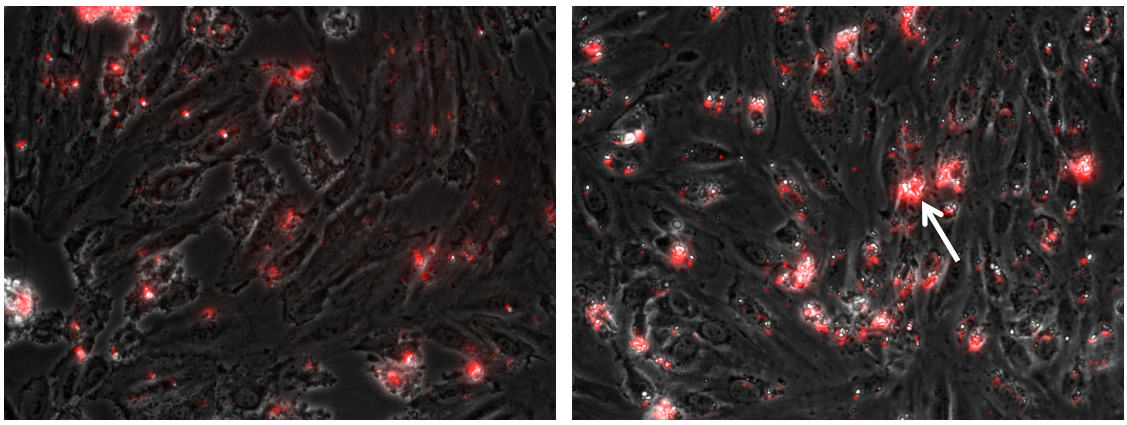

Figure 53. Composite images of nanoparticle complex absorption by HUVECS when incubated with no TNF-α at 1 hour (left) and 5 hours (right). Fluorescence shows dense absorption within several cells rather than across most cells, as seen by the density in the cell with the arrow.

With the baseline non-specific and baseline nanoparticle absorption kinetic behaviors, it is possible to compare the control kinetics with the kinetics of the full nanoparticle complex. Also, it is possible to infer the specificity of the targeting mechanism by observing the fluorescence intensity distributions as compared to the previous control experiments. Images were once again analyzed with a combination of MATLAB and ImageJ.

The pattern for the full nanoparticle complex is similar to the bead experiments. Upon visual inspection, there does not seem to be much different between the bare nanoparticles and the nanoparticle complex. Cells at the one hour time point show a level of cell layer degradation typically seen in the presence of TNF-α. This is particularly odd as even in the sample incubated without TNF-α there is noticeable morphology changes. The trend extends to the other samples, although the disruption is more in the monolayer and less in the morphology.

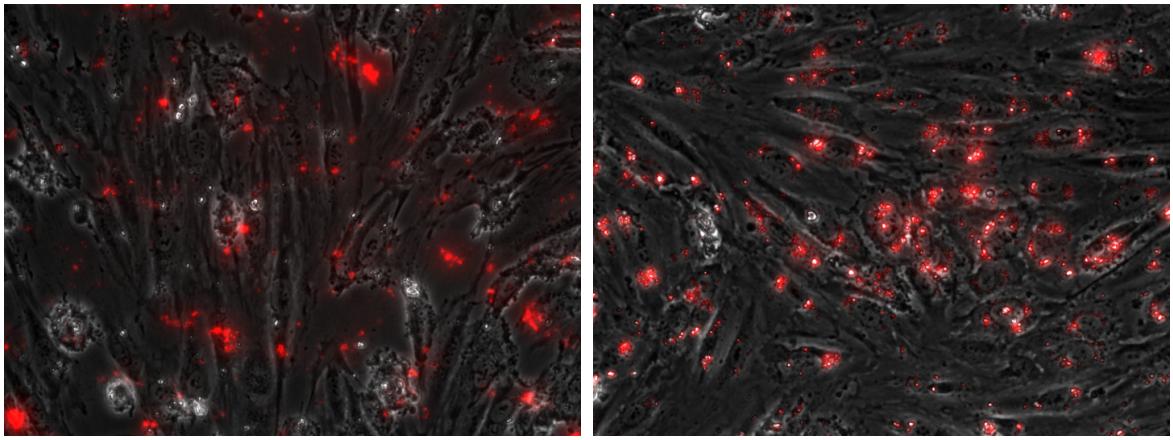

Figure 54. Composite images of nanoparticle complex absorption by HUVECS when incubated with 2 µg/mL TNF-α at 1 hour (left) and 5 hours (right). Once again, maximal fluorescence occurs in this sample.

At the one hour time point, the MFIs at the three levels of TNF-α are 13.3, 14.2, and 12.4 in increasing order. These correspond to Figures 53, 54 and 55 respectively. Seeing a decrease in mean fluorescence for the 20 µg/mL sample is no surprise now and at this point can be attributed to the degradation of the monolayer. The important note is that the MFIs are much higher than the nanoparticle control; the ratio of MFIs between the experimental and control group comes out to be 4.1, 3.7, and 3.8, with 3 trials for each sample. This is a relatively large difference when compared to the increase over time for the bare nanoparticles.

A result of note is that absorption at one hour is moderately higher than with the bare nanoparticle. This result indicates that the nanoparticle complex absorption kinetics begins at a higher rate than in non-specific absorption. However, the result for the 0 µg/mL sample is strange. There is little VCAM-1 expression in the staining as seen in the previous section, and yet the absorption of the nanoparticles with anti-VCAM-1 attached is very similar to the other levels of TNF-α. It is possible that even baseline VCAM-1

expression is enough to cause absorption of the nanoparticle complex or the absorption mechanism is not as expected.

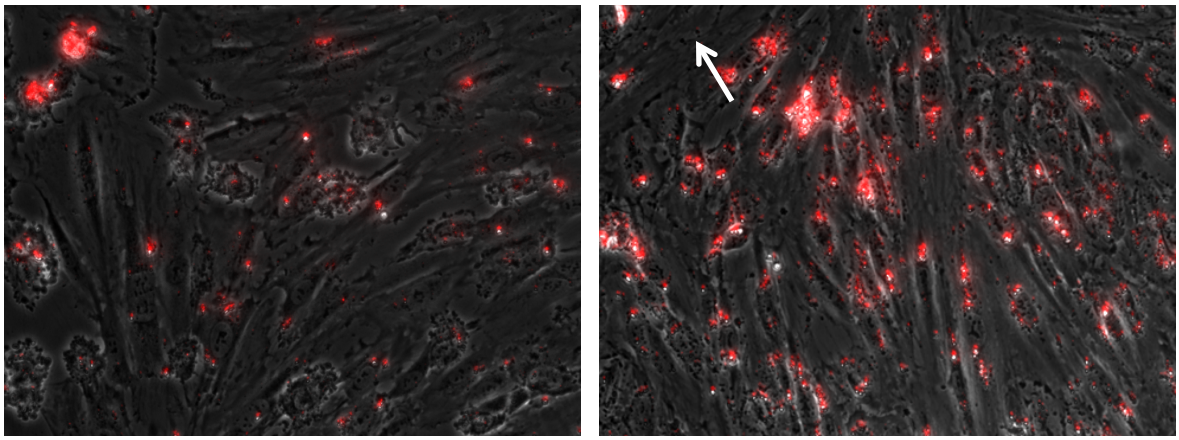

Figure 55. Composite images of nanoparticle complex absorption by HUVECS when incubated with 20 µg/mL TNF-α at 1 hour (left) and 5 hours (right). The 5 hour shows a large increase in fluorescence, but once again it is not evenly distributed through the cells. A dead patch is shown with the arrow.

At the five hour time point, results show the typical increase in fluorescence, although not to the same degree as with the beads. Once again, more fluorescence is seen throughout the cell layer; the clusters of fluorescence are typically denser, resulting in the increase of overall fluorescence seen in the image. However, only in the sample incubated in 20 µg/mL TNF-α is there a marked increase in the number of clusters. The MFIs match the observation; for the three levels, the MFIs are 18.4, 18.5, and 18.5. This is the first time that the spread has been so small, although this could be a result of the wildly varying results seen at the one hour time point as well.

When comparing the effects of TNF-α on the cell layer to other experiments, it seems that the five hour time point shows far less change than in the one hour time point, and even possibly in other experiments. There is a slight morphological change as the level of TNF-α increases, but the amount of disruption is fairly constant throughout the

increase in TNF-α. This could possibly be an explanation for the relatively small difference seen in the MFIs at the five hour time point.

The ratio between the five hour time point MFIs of the complex and control samples is smaller than at the one hour time point. It is only approximately 2 or 3 this time; 2.4 for the 0 μg/mL sample and 3.1 for the 20 μg/mL sample. It is hard to determine exactly what the ratio is for the 2 μg/mL sample given that the control had an anomalous data point. However, it is safe to say that the ratio decreases from the one hour to the five hour time point when compared to the control experiments. Thus the nanoparticle complex has slightly different absorption kinetics than both the non-specific case and the bare nanoparticle case. Based on the two time points, the complex has more rapid initial absorption but slows down. The complex would then most likely reach critical concentrations in the specimen sooner than a bare nanoparticle.

Once again the MFI of the 0 μg/mL sample is disturbing. Despite the lack of VCAM-1 expression, the absorption is undisturbed. Should the MFI have remained at the previous level, the results would be more reasonable. However, now the question arises: by what mechanism is the absorption achieved? Clearly the level of VCAM-1 expression as regulated by TNF-α does not significantly affect absorption of the nanoparticle complex.

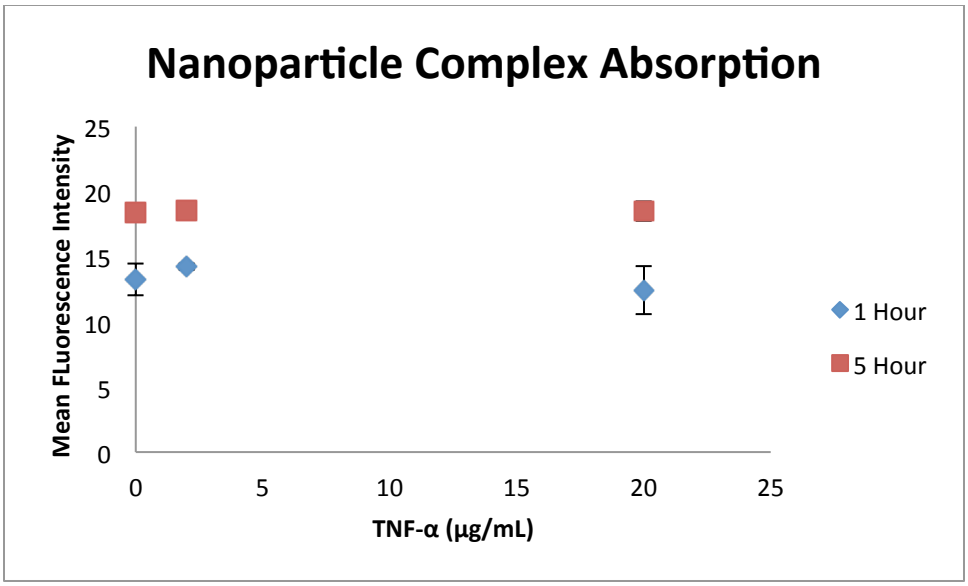

Figure 56. Nanoparticle complex absorption trend in relation to TNF-α. The trend is no longer a general decrease. Instead we see a biphasic trend at the 1 hour time point, and a flat amount of fluorescence for the 5 hour time point.

An interesting note to make for the nanoparticle complex is the different absorption trend in relation to TNF-α. In the beads as well as the bare nanoparticle results (with the outlier removed), we saw a general decrease in absorption in relation to TNF-α. Despite the anomalous data point for the control at the 5 hour time point, the trend is still very similar. This is in contrast with what we see in the nanoparticle complex absorption, as seen in Figure 56. What we actually see instead is a biphasic trend, with the maximal amount of fluorescence occurring in the 2 µg/mL group instead of the 0 µg/mL group. This is not necessarily evident at the 5 hour time point though, as all the groups show very similar fluorescence. However, it is clear at the 1 hour time point that the absorption trend is different than the bare nanoparticle absorption. The results show that the mechanism is most likely different from non-specific absorption seen in both the beads and bare nanoparticles.

5.3 Nanoparticle Complex with BBB Model Discussion

5.3.1 Discussion of Image Trends

Many of the same trends seen in the VCAM-1 staining and bead absorption experiments are once again seen in the nanoparticle absorption experiments. TNF-α has expected effects on the cell layer, although these results did not necessarily translate to increased fluorescence. In both sets of experiments, gaps between cells increased as TNF-α also increased. With cells covering a smaller area, there should be less fluorescence, which is seen for the 20μg/mL samples in both the control and the experimental groups.

The reduced cellular area is in competition with the effects of TNF-α though. At 2 μg/mL, the fluorescence increases across almost all samples, from the HBMECs through the complex. The only exception is the one hour time point for the nanoparticle absorption experiments where the mean fluorescence drops. It is somewhat strange that we would see a sudden drop in only that particular sample. The possibility arises that the sample was affected in some way before the experiment that caused variations we did not expect to see. It makes it hard to compare the fluorescence values with the five hour time points and other data sets.

Aside from that sample, we can expect that these results are reasonable. Then, as previously mentioned, at 20 μg/mL the fluorescence goes back down compared to the 2μg/mL samples. TNF-α acts both to disrupt the monolayer and signal cells to increase absorption. As we can see, one effect is more dominant at certain levels. At higher concentrations, there is less cellular area and thus less area for fluorescence to appear, reducing the mean fluorescence. At lower concentrations, the cell signaling is the predominant effect.

One of the difficulties in comparing the nanoparticle images is the lack of a background stain to compare the fluorescence with. In the VCAM-1 staining experiments, the resulting VCAM-1 fluorescence can be compared to other images by normalization based on the number of cells seen in nucleus stains. While in that case, the normalization was not necessary given the coverage of VCAM-1 in the samples, it is more important in the absorption experiments. Without a full monolayer present, the total cellular area is not approximated by the total area of the image. Normalization would then make sense to compare fluorescence per cell as opposed to overall fluorescence. Without a way to accurately quantify either the number of cells aside from counting them in the phase image, normalization would not represent the fluorescence well. Even counting cells in the phase image is difficult as cell morphology changes make cells hard to differentiate at points. Normalization may bring the MFIs for the 20 μg/mL samples back in line with the trends seen in the VCAM-1 experiments, although that is not a guarantee.

5.3.2 Ranging Effects of TNF-α on Endothelial Cells

TNF-α is a cytokine present during the inflammatory response, but its actions are not limited to just the regulation of cell adhesion molecules. TNF-α can additional cause the release of other cytokines and other chemotactic factors.[98] The cellular cascades that these other cytokines may be similar to the actions of TNF-α or entirely different, therefore we are unable to take into account the inevitable physiological changes not resulting directly from TNF-α. TNF-α inhibits cell growth, causes cytocidal activity, modulation of gene expression, activation of g proteins, modulation of protein

phosphorylation.[99] Overall, TNF-α can cause endothelial damage and increased perfusion.[100] These physiological and architectural effects are illustrated with the addition of 2μg/mL and 20μg/mL of TNF-α, with significant gaps apparent in the monolayer of HUVEC cells in both the control and full complex tests.

The lack of a monolayer in portions of the coverslips may have contributed to the inconsistent findings within the control and full complex results at 20μg/mL, because both types of nanoparticles could have aggregated in those open areas instead of binding primarily to the HUVECs. The aggregation of particles due to the changes in morphology also could have either prevented the removal of unbound particles during washing due to interactions with the cytoskeleton or exasperated the removal of unbound nanoparticles in gaps in the monolayer. These two factors could have played a factor in the unexpected fluorescent patterns going from 2μg/mL and 20μg/mL of TNF-α. Overall, the physiological and architectural changes to our HUVEC monolayer after the addition of TNF-α could have contributed to the inconsistency in fluorescence and apparent nanoparticle binding.

5.3.3 Cell-Adhesion Molecule Targeting Capabilities

As stated in the background section about the blood-brain barrier, during diseased states, infected cells secrete TNF-α to produce the inflammatory response. VCAM-1 is a cellular adhesion molecule that is up-regulated during these states as a result of cellular cascades. VCAM-1, however, is not immune to other physiological changes and also requires the use of other receptors. VCAM-1 expression is also coupled with oxidative stress caused through oxidation-reduction reactions, which can additionally affect

transcriptional and translational pathways within the HUVEC cells.[101] This additional molecular consequence could have altered expected levels of cell adhesion molecule expression in a way that we are unable to account for. The activation of nuclear factor NF-κB seems to involved in these redox reactions with VCAM-1, and is involved in the cellular cascades that help create the inflammatory conditions, relating back to the changes in morphology in our HUVEC monolayers.[98] VCAM-1 appears to be dependent on NF-κB to mediate leukocyte binding to ECs.[101]

VCAM-1 is also dependent on a counter receptor, VLA-1 that is present on monocytes and lymphocytes.[101,102] The interaction of these two molecules facilitates the binding of leukocytes to the ECs in general, and the lack of this additional receptor on our nanoparticle complex may contribute to the lack of efficient binding to our HUVEC monolayer. In relation to the binding of nanoparticle complex to cells bathed in no TNF-α, there could be some underlying expression of VCAM-1 in the HUVECs. Such weak expression was found in other types of ECs, but this should not impede our nanoparticle binding.[103] This reasoning could explain why there is baseline aggregation/attachment of our nanoparticle complex to our HUVEC monolayers at 0μg/mL of TNF-α. However, we are unable to assess the degree of this binding in comparison to aggregation of clusters around the monolayer itself.

Other cellular adhesion molecules, such as ICAM-1 and E-selectin receptors are additionally present on the surface of the HUVEC ECs.[101,102] TNF-α greatly increases the mRNA expression of these cellular adhesion proteins.[98] The two other receptors also help bind leukocytes to the ECs through specific ligand interactions. The expression of these molecules on ECs occurs at similar time periods: E-selectin has a maximum expression at

4 hours, and then decreases after 24 hours, ICAM-1 has a maximum expression at 12-14 hours and stays elevated for several days, and VCAM-1 has a maximum expression at 12 hours, and then slowly declines over several days.[102]

The TNF-α incubation period for all of the nanoparticle tests were roughly 18 hours, therefore numerous cell adhesion molecules were present at close to maximum level during our VCAM-1 nanoparticle-complex test. The overall time-dependent increase in several important cell adhesion molecules on the HUVECs could be one reason why the there was some inconsistencies in fluorescence at differing TNF-α levels and time points. The nanoparticle complex theoretically should have primarily interacted with elevated VCAM-1 levels, and fluorescence should have been greater compared to the nanoparticle control. This may have been present initially after the additions of the nanoparticle complex, as absorption kinetics begin at a higher rate compared to non-specific interaction after 1 hour incubation. However, the increase from 0μg/mL to 2μg/mL and then finally to 20μg/mL of TNF-α did not show a substantive trend between the control and full complex. Additionally, the VCAM-1 expression may have decreased over time between the one and five hour time points, since this was past the maximal expression time point (testing was performed at 18 hours), thus causing additional discrepancies in fluorescence between the one and five hour time points. The additional interaction of the nanoparticles with the additional up-regulated cell adhesion molecules may somehow disrupt or inhibit binding to VCAM-1 receptors, thus reducing the apparent fluorescence upon observation. However, this is theoretical speculation, and we are unable to prove that this is a hindering consequence of TNF-α addition.

While the research on VCAM-1 as a targeting prospect is still in development, much research exists on the efficacy of ICAM-1 as a possible means for drug-delivery. ICAM-1 is also upregulated during inflammatory conditions, and mediates attachment of all classes of leukocytes to the EC.[102,104] Additionally, ICAM-1 has been found to aid in the actual transmigration of leukocytes through the EC itself, and thus can aid in transmigration through the BBB.[104] VCAM-1 has been found to be sensitive to deregulation, but ICAM-1 however, is not sensitive to this mechanism.[101] The two classes of cell adhesion molecules may have similar expression mechanisms at the onset of inflammatory conditions, but the steady expression of these cell adhesion molecules is different. ICAM-1 can be internalized back into the cell membrane, but then reappear on the surface through molecule recycling mechanisms.[74] It is not known whether or not VCAM-1 posses this internalization capability, as there are many contradictory studies.[103] One study that used immunoliposomes targeted to VCAM-1 showed that the liposomes bound specifically to VCAM-1, and that some of them were taken up by clathrin coated vesicles, but the authors cited the need for additional experiments to confirm the internalization.[103]

This recycling property has posed as an attractive target for drug-delivery because it provides a pathway for recurrent drug interaction on infected cells, thus having longer therapeutic effects. In one specific study, 50% of internalized ICAM-1 was recycled back to the plasma membrane relatively intact within one hour after initial internalization of the molecule.[74] One ICAM-1 molecule can go through several rounds of internalization and reappearance, thus theoretically allowing for sustained drug-delivery targeting and

therapeutic effects.[74,105] Experiments with binding of nanocarriers to multiple copies of anti-ICAM-1 showed endocytic uptake and intracellular delivery of internal cargo.[105]

Our novel drug-delivery carrier focuses on VCAM-1 adhesion, and while VCAM-1 is found to work in tandem with ICAM-1 to traffic leukocytes to inflamed states in the brain (black), the overall efficacy of choosing VCAM-1 as a particular drug delivery tactic may be less significant compared to ICAM-1 research. Our experiment is purely in its primary trial phase, as data was only collected once for each experiment due to time and budgetary issues, so this conclusion can only be speculated at this time. Additional trials, technical refinement, and potential comparisons to ICAM-1 tests are necessary before we can evaluate the significance of VCAM-1 as a drug-delivery target for the BBB.

6. Conclusion

6.1 Blood Brain Barrier Experiments

We created an *in vitro* BBB model to simulate the structure of the BBB to later test our nanoparticle-based drug delivery mechanism. Adding varying levels of TNF-α to simulate inflammation in the barrier was expected to increase expression of the cell adhesion molecule VCAM-1. Thus, our goals in testing the BBB model were to, first, determine the patterns of VCAM-1 expression under varying levels of TNF-α, then determine the absorption characteristics of our monolayer. In the course of our experiments, we were forced to simplify the properties of our model (including eliminating Transwell inserts and a hydrogel layer then using HUVECs instead of HBMECs) because of exogenous constraints such as resources and inconsistent cell growth. However, we were still able to conduct the appropriate experiments to meet our testing goals.

In the first test of VCAM-1 expression in HBMECs, we find that VCAM-1 expression, measured by fluorescence, increases with additional TNF-α, but in a logarithmic fashion. In the second experiment doing the same process but using HUVECs, we see that VCAM-1 expression does not continuously increase with rising levels of TNF-α. Instead, it increases at the second level then decreases back to baseline at the maximum level of TNF-α. Finally, we tested non-specific absorption properties of the HUVEC monolayer using fluorescent beads. The results are similar to the HUVEC VCAM-1 staining experiment. There are higher concentrations of fluorescence at later time points (more at 5 hours compared to 1 hour), but the pattern of VCAM-1 expression at increasing levels of TNF-α actually decreases much like the second experiment.

Although the magnitude and pattern differ between HBMECs and HUVECs in VCAM-1 expression through fluorescence, there is a noted up-regulation in fluorescence with the addition of TNF-α. This similarity makes HUVECs an appropriate proxy for HBMECs in our model to test with the drug delivery mechanism. To test the absorption properties of the model using HUVECS, we added fluorescent beads, the uptake of which we hypothesized would increase over time and with more TNF-α. We found that absorption actually decreased at higher levels of TNF-α, but that there is increased absorption over time, which may be because of deterioration of the simplistic monolayer with the introduction of beads.

The testing of our BBB model resulted in some inconsistencies and unexpected results, providing more understanding into the limitations of our simplistic model. However, we were able to discern in some capacity that there is up-regulation of VCAM-1 expression with added TNF-α that increases absorption, which makes VCAM-1 an appropriate targeting molecule on our model for the drug delivery mechanism.

6.2 Nanoparticle Complex Experiments

After taking the necessary steps to create the nanoparticles, we had to quantitatively and qualitatively assess nanoparticle formation. Newly formed, unfiltered nanoparticles were non-uniform in size and shape. Moreover, the unfiltered nanoparticles displayed a wide range of sizes. Since diverse nanoparticle morphology is unsatisfactory for our purposes, we passed newly formed nanoparticles through a 0.200 μm filter. The filtered nanoparticles displayed greater size uniformity, lower average size, and smaller distribution of sizes than the unfiltered nanoparticles. Filtration not only produced smaller

nanoparticles, but also decreased variability in nanoparticle morphology. This ultimately increases the chance of our nanoparticles to pass the BBB. Thus, filtration allowed us to bypass a limiting factor in BBB permeation

We then added streptavidin to the nanoparticles, as the nanoparticle-streptavidin complex constitutes half of our overall nanoparticle complex. Since the binding of nanoparticles to streptavidin is a limiting factor in forming the overall nanoparticle complex, we had to confirm that streptavidin successfully attached to nanoparticles. We found that nanoparticle-streptavidin complexes exposed to biotin-coated slides displayed the greatest number of fluorescent particles. Also, there was no particle visualization when nanoparticles with no streptavidin bound were placed on biotin slides. As a control, nanoparticles placed on a biotin free slide displayed insignificant numbers of particles. Due to the strong affinity of biotin and streptavidin, these findings suggest that nanoparticles successfully bound to streptavidin.

We also had to determine if the nanoparticle-streptavidin complex could attach to biotin, since this is another checkpoint to complex formation. Though past research suggests streptavidin and biotin have a strong affinity for each other, we had to quantitatively confirm this affinity to eliminate potential sources of error. Due to limited binding sites on streptavidin and principle of saturation, we expected that increased incubation time (two, four, and eight hour incubation times) would decrease counted nanoparticle-streptavidin complexes. This trend was significantly produced, suggesting that nanoparticle-streptavidin complex did bind to biotin.

We also found the concentration of filtered nanoparticles in our solution, which would allow us to later determine an appropriate ratio of streptavidin and biotin to add to

solution of nanoparticles. An appropriate ratio is needed to maximize the number of combination nanoparticle complexes. We found roughly 4000 nanoparticles/μL.

Our quality control tests for our nanoparticles displayed that filtered nanoparticles would be ideal for our purposes. Moreover, the nanoparticle-streptavidin complex was found to be stable and able to bind to biotin. Furthermore, knowing the concentration of nanoparticles in our solution, we can effectively form the end-stage nanoparticle complex with confidence that intra-complex interactions will be strong enough to support the final complex as we perform combination experiments.

6.3 Combination Experiments

We performed fluorescent imaging of the combined nanoparticle complex. Specifically, we performed MFI on a control group, involving the nanoparticle complex without anti-VCAM-1 incubated with HUVECs, and an experimental group consisting of the nanoparticle complex with anti-VCAM-1 incubated with HUVECs.

We found that the MFI in the experimental group was twice as great as the MFI in the control group. This suggests that targeting VCAM-1 successfully increases absorption of the nanoparticle complex into the cell layer. Moreover, this trend is seen across all levels of TNF-α. Generally, we found greater MFI measurements as incubation times of the cells were increased. MFI was also greater as the concentration of TNF-α was increased.

However, the cells displayed slight morphology changes as TNF-α levels were increased, but the observed amount of disruption was consistent throughout all levels of TNF-α. In essence, we confirmed that greater amounts of TNF-α do increase space

between cells. Moreover, cells covering a smaller surface are expected to display less fluorescence. Though surface area changes are in competition with TNF-α levels, we found this trend to hold true with 20 μg/mL samples, but not other samples. We also observed an unexpected sharp decrease in MFI at the one hour mark for nanoparticle absorption experiments.

In essence, we found that TNF-α significantly disrupts cell monolayers to increase absorption of our nanoparticle complex. Still, there is a push-pull mechanism to consider. At greater concentrations of TNF-α, there is less cell surface area, which in turn limits the amount of measured fluorescence. At lower levels of TNF-α, cell signaling to absorb the nanoparticle complex is predominant.

VCAM-1 expression is also mediated by other cellular mechanisms, which we did not account for with our experiments. Also, VCAM-1 is not the only cellular adhesion molecules found in HUVECs. Since all cellular adhesion molecules are expressed more so in the presence of TNF-α, their presence contributes additional bias to our results.

6.4 Experimental Considerations

6.4.1 Creating a More Accurate *in vitro* BBB Model

First, our *in vitro* BBB model was a simplistic design that did not incorporate many other aspects of the *in vivo* BBB such as pericytes and astrocytes.[58] Because of resource and time constraints, we decided to create a simple monolayer of ECs. We had originally planned to use Transwell inserts and a hydrogel layer to both better simulate permeation and be better able to analyze volume of final nanoparticles. Unfortunately, forming a monolayer on the Transwell inserts using either the HBMECs or the HUVECs

was problematic. After multiple attempts to produce a Transwell monolayer did not work, we had to adapt our *in vivo* BBB by using endothelial cells on glass coverslips. Creating a more complex, realistic *in vitro* BBB would allow us to obtain more realistic results and make more relevant conclusions. Additionally, our model used HUVECs instead of HBMECs because we had difficulty maintaining the HBMEC lines. Although HUVECs have similar properties as HBMECs because they are both ECs, HBMECs are more useful to study transport across the BBB because they have been shown to have higher TEER values than HUVECs. This means that HMBECs would have provided tighter junctions and been more representative of an *in vivo* BBB.[106] Again, since we were limited by time, we could not improve upon our HBMEC culturing methods or repeat our experiments using a model made of HBMECs. We were limited to plating HBMECs onto fibronectin, so we were unable to accurately represent the BBB as described by other model studies, which primarily use co-culture techniques in Transwell inserts. Co-culture techniques produce a more physiologically viable BBB due to the release of chemical mediators from accessory cells (astrocytes and pericytes). Lastly, the addition of flow would be highly beneficial in simulating *in vivo* conditions and could cause significant changes in our results. Creating a more complex, realistic *in vitro* BBB would allow us to obtain more realistic results and make more relevant conclusions.

Biologically, TNF-α is expressed in much smaller quantities than those used in our experimental trials. We chose the levels of 0μg/mL, 2μg/mL, and 20μg/mL to provide a significant difference that would allow for visualization of nanoparticle complex transmigration. Now that we have concluded that our drug delivery complex

does indeed use VCAM-1 targeting, we would complement a more realistic BBB model with more biologically relevant TNF-α concentrations.

6.4.2 Fine-Tuning Nanoparticle Creation

Our nanoparticle complex also could have benefitted from more fine-tuning to create even smaller and more uniform particles. Our ability to minimize and homogenize the size of our nanoparticles was limited, because our sonicator was limited to a frequency of only 60 Hz, while previous studies involving CSLN sonicated their nanoparticles at 20kHz.[29] Our ability to measure the size and uniformity of our nanoparticles was also limited. We were able to limit the size of our nanoparticles to below 200 μm in diameter by filtering the nanoparticle solution through a 200 μm filter. The sizes of our nanoparticles were analyzed rudimentarily through ImageJ analysis, but more precise estimates and numbers could have been obtained using a Zetasizer instrument.

6.4.3 Nanoparticle Complex Physiological Side Effects

It is also important for us to understand the physiological side effects of our nanoparticle complex on the BBB. Possible toxicity in the nanoparticle components or media could have been detrimental to the cells in our BBB model. We could have could have assessed the toxicity of our nanoparticles by applying them at different concentrations to cultures of HUVECs, and comparing our results against negative control groups. While we attempted to detoxify our nanoparticle solution by filtering it through a 200 μm filter to filter out any existing bacteria, the process could have been

enhanced by performing all of our experiments under sterile conditions (i.e. in a sterile hood). While our filtering of the nanoparticle solution significantly decreased the amount of contamination experienced on our BBB model, there was still a lot of debris that could have been minimized through sterilization techniques.

In our experiments, we only added a fixed concentration of the nanoparticle complex, which may or may not have caused the individual particles to aggregate. It would be of interest to replicate our experiments using varying concentrations of the complex in order to investigate the complex's aggregating properties, and whether this benefits its transmigration.

6.4.4 Conducting Multiple Trials

Lastly, time and resource restraints prevented us from conducting as many trials in each experiment as we had originally intended. Local fluctuations in cell fluorescence in our samples may have skewed our results since we had too few samples. To obtain more definitive results, we would want to repeat each control and experimental trial at least three more times. The data presented in this paper is therefore preliminary, and should be reconfirmed through additional experimentation using the same methodology.

6.5 Future Directions

Drug delivery through the BBB is a topic with immense potential in the medical field. It has important implications for neurological diseases and understanding of physiological functions. There is much more work that can be done to perfect these methods and save more lives.

6.5.1 *In vivo* BBB Model Experiments

An important next step in BBB experiments would be to conduct experiments *in vivo*. This would allow us to test how our drug delivery mechanism would actually interact within the body and bring to light the many other factors to consider when in a complex environment. *In vitro* environments may attempt to capture *in vivo* conditions as much as possible, however, there are still physiological characteristics that are difficult to recreate in an external setting; for example, the heterogeneity of VCAM-1 up regulation in the brain. Once *in vitro* data is confirmed with additional experiments, *in vivo* experiments should be proposed to consider our drug-delivery capabilities in an organism. The goal of our project was to see if our nanoparticle complex was able to migrate across the BBB more efficiently than current drug delivery methods. The next step is to determine how the drug would be released from the nanoparticle complex into a specific region of the brain once it passes through the BBB.

6.5.2 Drugs to Replace Fluorescent Dye

Eventually, nanoparticle carriers will need to include actual drugs to treat neurological diseases instead of fluorescent dye substitutes. This would allow investigators to both determine the interaction of drugs within the nanoparticle complex and better simulate actual release of drugs into the body. This is an important step because of the current dearth of neurological drugs whose development is hindered by the inability to penetrate the BBB. The amount of neurological drugs would have to increase by 500% to be comparable to cardiovascular drugs.[107] Since only small, hydrophilic molecules can cross the BBB, this limits the kinds of drugs developed. Many of the most

prominent afflictions, such as Alzhiemer's, brain cancer, stroke, Huntington disease, and amyotrophic lateral sclerosis (ALS) cannot be treated drugs of this size. Creating viable methods for other objects to traverse the BBB would spur more research and development for actual drugs combat these serious brain disorders.

Bibliography

1. Cardoso FL, Brites D, Brito MA. Looking at the blood-brain barrier: Molecular anatomy and possible investigation approaches. *Brain Research Reviews.* 2010;64:328-363.

2. Lim S-T. Nuclear-localized focal adhesion kinase regulates inflammatory VCAM-1 expression. In: Miller NLG, ed. Vol 197: The Rockefeller University Press; 2012:907-919.

3. Banks WA, Erickson MA. The blood-brain barrier and immune function and dysfunction. *Neurobiol Dis.* Vol 37. United States2010:26-32.

4. Begley DJ. Delivery of therapeutic agents to the central nervous system: the problems and the possibilities. *Pharmacology and Therapeutics.* 2004(104):29-45.

5. Banks W. The Blood Brain Barrier. In: Ikezu T, Gendelman HE, eds. *Neuroimmune Pharmacology*. New York: Springer; 2008:21-38.

6. Ballabh P, Braun A, Nedergaard M. The blood–brain barrier: an overview: Structure, regulation, and clinical implications. *Neurobiology of Disease.* 2004;16(1):1-13.

7. Carvey PM, Hendey B, Monahan AJ. The blood–brain barrier in neurodegenerative disease: a rhetorical perspective. *Journal of Neurochemistry.* 2009(111):291-314.

8. Lai CH, Kuo KH. The critical component to establish in vitro BBB model: pericyte. *Brain Research Review.* 2005(50):258-265.

9. Persidsky Y, Ramirez SH, Haorah J, Kanmogne GD. Blood-brain barrier: structural components and function under physiologic and pathologic conditions. *Journal of Neuroimmune Pharmacology.* 2006(1):223-236.

10. Rubin LL, Hall DE. A Cell Culture Model of the Blood-Brain Barrier. 1991.

11. Weksler BB, Subileau EA, Perriere N, et al. Blood-brain barrier-specific properties of a human adult brain endothelial cell line. *The FASEB Journal.* 2005.

12. Banks WA, Ercal N, Price TO. The Blood-Brain Barrier in NeuroAIDS. *Current HIV Research.* 2006;4(3):259-266.

13. Butt AM, Jones HC, Abbott NJ. Electrical resistance across the blood-brain barrier in anaesthetized rats: a developmental study. *J Physiol.* Oct 1990;429:47-62.

14. Li G, Simon M. Permeability of Endothelial and Astrocyte Cocultures: In Vitro Blood–Brain Barrier Models for Drug Delivery Studies. 2010.

15. Hatherell K. Development of a three-dimensional, all-human in vitro model of the blood–brain barrier using mono-, co-, and tri-cultivation Transwell models. 2011.

16. Stroka KM, Aranda-Espinoza H. Endothelial cell substrate stiffness influences neutrophil transmigration via myosin light chain kinase-dependent cell contraction. 2011.

17. Kitahara T, Hiromura K. Mesangial cells stimulate differentiation of endothelial cells to form capillary-like networks in a three-dimensional culture system.

18. Kleinman H, Martin G. Matrigel: Basement membrane matrix with biological activity. 2005.

19. Choong C, Hutmacher D, Triffitt J. Co-culture of Bone Marrow Fibroblasts and Endothelial Cells on Modified Polycaprolactone Substrates for Enhanced Potentials in Bone Tissue Engineering 2006.

20. Banks W, Audus K, Davis T. Permeability of the Blood-Brain Barrier to Peptides: An Approach to the Development of Therapeutically Useful Analogs. 1992.

21. Ragnaill MN, Brown M, Ye D, et al. Internal benchmarking of a human blood-brain barrier cell model for screening of nanoparticle uptake and transcytosis. *European Journal of Pharmaceutics and Biopharmaceutics.* Apr 2011;77(3):360-367.

22. Agarwal A, Agrawa H, al e. Cationic ligand appended nanoconstructs: A prospective strategy for brain targeting. *International Journal of Pharmaceutics.* 2011;421(1):189-201.

23. Briz V, Poveda E, Soriano V. [HIV entry into the cells--mechanisms and therapeutic possibilities]. *Med Clin (Barc).* Mar 2006;126(9):341-348.

24. Ma Y, Nolte RJM, Cornelissen JJLM. Virus-based nanocarriers for drug delivery. *Advanced Drug Delivery Reviews.* (0).

25. Garcea RL, Gissmann L. Virus-like particles as vaccines and vessels for the delivery of small molecules. *Current Opinion in Biotechnology.* 2004;15(6):513-517.

26. Engelhardt B, Ransohoff RM. The ins and outs of T-lymphocyte trafficking to the CNS: anatomical sites and molecular mechanisms. *Trends in Immunology.* 2005;26(9):485-495.

27. Ruth Lyck YR, Nicole Gerwin, John Greenwood, Peter Adamson, and Britta Engelhardt. T-cell interaction with ICAM-1/ICAM-2 double-deficient brain endothelium in vitro: the cytoplasmic tail of endothelial ICAM-1 is necessary for transendothelial migration of T cells. The American Society of Hematology; 2003.

28. Kim Y, Dalhaimer P, Christian DA, Discher DE. Polymeric worm micelles as nano-carriers for drug delivery. Vol 16: IOP Science Nanotechnology; 2005:S484-S491.

29. Kim HR, Kim IK, Bae KH, Lee SH, Lee Y, Park TG. Cationic Solid Lipid Nanoparticles Reconstituted from Low Density Lipoprotein Components for Delivery of siRNA. *Molecular Pharmaceutics.* 2008;5(4):10.

30. Bondi ML, Di Gesu R, Craparo EF. Lipid nanoparticles for drug targeting to the brain. *Methods Enzymol.* 2012;508:229-251.

31. Faraji AH, Wipf P. Nanoparticles in cellular drug delivery. *Bioorganic & Medicinal Chemistry.* 2009;17(8):2950-2962.

32. Cho K, Wang X, Nie S, Chen Z, Shin DM. Therapeutic Nanoparticles for Drug Delivery in Cancer. *Clinical Cancer Research.* March 1, 2008 2008;14(5):1310-1316.

33. Roney C, Kulkarni P, Arora V, et al. Targeted nanoparticles for drug delivery through the blood–brain barrier for Alzheimer's disease. *Journal of Controlled Release.* 2005;108(2–3):193-214.

34. Koo OM, Rubinstein I, Onyuksel H. Role of nanotechnology in targeted drug delivery and imaging: a concise review. *Nanomedicine: Nanotechnology, Biology and Medicine.* 2005;1(3):193-212.

35. Bickel U, Yoshikawa T, Pardridge WM. Delivery of peptides and proteins through the blood-brain barrier. *Adv Drug Deliv Rev.* Mar 1 2001;46(1-3):247-279.

36. Fukui H, Koike T, Saheki A, Sonoke S, Seki J. A novel delivery system for amphotericin B with lipid nano-sphere (LNS®). *International Journal of Pharmaceutics.* 2003;265(1–2):37-45.

37. Yu YH, Kim E, Park DE, et al. Cationic solid lipid nanoparticles for co-delivery of paclitaxel and siRNA. *European Journal of Pharmaceutics and Biopharmaceutics.* 2012;80(2):268-273.

38. Montenegro L, Trapani A, Latrofa A, Puglisi G. In vitro evaluation on a model of blood brain barrier of idebenone-loaded solid lipid nanoparticles. *J Nanosci Nanotechnol.* Jan 2012;12(1):330-337.

39. Holmberg A, Blomstergren A, Nord O, Lukacs M, Lundeberg J, Uhlen M. The biotin-streptavidin interaction can be reversibly broken using water at elevated temperatures. *Electrophoresis.* 2005;26(3):10.

40. Hubbard AK, Rothlein R. Intercellular adhesion molecule-1 (ICAM-1) expression and cell signaling cascades. *Free Radical Biology and Medicine.* 2000;28(9):1379-1386.

41. Bhowmick T, Berk E, Cui X, Muzykantov VR, Muro S. Effect of flow on endothelial endocytosis of nanocarriers targeted to ICAM-1. *Journal of Controlled Release.* 2012;157(3):485-492.

42. Bloeman PGM, Henricks PAJ, van Blous L, et al. Adhesion molecules: a new target for immunoliposome - mediated drug delivery. *Federation of European Biochemical Societies.* 1995;357:140-144.

43. Dietrich J-B. The adhesion molecule ICAM-1 and its regulation in relation with the blood–brain barrier. *Journal of Neuroimmunology.* 2002;128(1–2):58-68.

44. Hohsfield LA, Humpel C. Homocysteine enhances transmigration of rat monocytes through a brain capillary endothelial cell monolayer via ICAM-1. *Curr Neurovasc Res.* Aug 2010;7(3):192-200.

45. Voinea M, Manduteanu I, Dragomir E, Capraru M, Simionescu M. Immunoliposomes directed toward VCAM-1 interact specifically with activated endothelial cells - a potential tool for specific drug delivery. *Pharmaceutical Research.* 2005;22(11):1906-1917.

46. Hwang SJ, Ballantyne CM, Sharrett AR, et al. Circulating adhesion molecules VCAM-1, ICAM-1, and E-selectin in carotid atherosclerosis and incident coronary heart disease cases: The Atherosclerosis Risk In Communities (ARIC) study. *Circulation.* 1997;96(12):4219-4225.

47. Steffen BJ, Butcher EC, Engelhardt B. Evidence for involvement of ICAM-1 and VCAM-1 in lymphocyte interaction with endothelium in experimental autoimmune encephalomyelitis in the central nervous system in the SJL/J mouse. *Am J Pathol.* Jul 1994;145(1):189-201.

48. Steiner O, Coisne C, Cecchelli R, et al. Differential roles for endothelial ICAM-1, ICAM-2, and VCAM-1 in shear-resistant T cell arrest, polarization, and directed crawling on blood-brain barrier endothelium. *J Immunol.* Oct 2010;185(8):4846-4855.

49. Gosk S, Moos T, Gottstein C, Bendas G. VCAM-1 directed immunoliposomes selectively target tumor vasculature *in vivo*. *Biochimica et Biophysica Acta.* 2008;1778(4):854-863.

50. Wong D, Dorovini-Zis K. Expression of Vascular Cell Adhesion Molecule-1 (VCAM-1) by Human Brain Microvessel Endothelial Cells in Primary Culture. *Microvascular Research.* 1995;49:325-339.

51. Briscoe DM, Cotran RS, Pober JS. Effects of tumor necrosis factor, lipopolysaccharide and IL-4 on the expression of vascular cell adhesion molecule-1 in vivo. *J. Immunol.* 1992;149(9):2954-2960.

52. de Lemos JA, Hennekens CH, Ridker PM. Plasma concentration of soluble vascular cell adhesion molecule-1 and subsequent cardiovascular risk. *Journal of the American College of Cardiology.* 2000;36(2):423-426.

53. Addabbo\ F. *Globular adiponectin counteracts VCAM-1-mediated monocyte adhesion via AdipoR1/NF-κB/COX-2 signaling in human aortic endothelial cells*. Italy: Dept. of Biomedical Sciences and Human Oncology, University of Bari; 2011.

54. Gunawan RC, Almeda D, Auguste DT. Complementary targeting of liposomes to IL-1α and TNF-α activated endothelial cells via the transient expression of VCAM1 and E-selectin. *Biomaterials.* Dec 2011;32(36):9848-9853.

55. Voinea M, Manduteanu I, Dragomir E, Capraru M, Simionescu M. Immunoliposomes Directed Toward VCAM-1 Interact Specifically with Activated Endothelial Cells—A Potential Tool for Specific Drug Delivery. Nov 24 2005(11):1906-1917.

56. Osborn L, Hession C, Tizard R, et al. Direct expression cloning of vascular cell adhesion molecule 1, a cytokine-induced endothelial protein that binds to lymphocytes. *Cell.* 1989;59(6):1203-1211.

57. Ricard I, Payet MD, Dupuis G. - VCAM-1 is internalized by a clathrin-related pathway in human endothelial cells but its α 4β 1 integrin counter-receptor remains associated with the plasma membrane in human T lymphocytes. 1998;-28(- 5):- 1718.

58. Abbott NJ, Ronnback L, Hansson E. Astrocyte-endothelial interactions at the blood-brain barrier. *Nat Rev Neurosci.* 2006;7(1):41-53.

59. Davson H, Oldendorf WH. Transport in the central nervous system. *Proceedings of the Royal Society of Medicine.* 1967;60:326-328.

60. Wolburg H, Lippoldt A. Tight junctions of the blood-brain barrier: development, composition and regulation. *Vascul Pharmacol.* Vol 38. United States2002:323-337.

61. Weiss N, Miller F, Cazaubon S, Couraud PO. The blood-brain barrier in brain homeostasis and neurological diseases. *Biochim Biophys Acta.* Vol 1788. Netherlands2009:842-857.

62. Reese TS, Karnovsky MJ. Fine structural localization of a blood-brain barrier to exogenous peroxidase. *J Cell Biol.* Jul 1967;34(1):207-217.

63. Daneman R, Agalliu D, Zhou L, Kuhnert F, Kuo CJ, Barres BA. Wnt/β-catenin signaling is required for CNS, but not non-CNS, angiogenesis. *Proceedings of the National Academy of Sciences of the United States of America.* 2008;106(2):641-646.

64. Liebner S, Corada M, Bangsow T, et al. Wnt/β-catenin signaling controls development of the blood–brain barrier. *Journal of Cell Biology.* 2008;183(3):409-417.

65. Janzer RC, Raff MC. Astrocytes induce blood-brain barrier properties in endothelial cells. *Nature.* Jan 15-21 1987;325(6101):253-257.

66. Armulik A, Genove G, Mae M, et al. Pericytes regulate the blood–brain barrier. *Nature.* 2010;468:557-561.

67. Nowacek A, Gendelman HE. NanoART, neuroAIDS and CNS drug delivery. *Nanomedicine (Lond).* Jul 2009;4(5):557-574.

68. Herve F, Ghinea N, Scherrmann J-M. CNS Delivery via Adsorptive Transcytosis. *AAPS.* 2008;10(3):455-472.

69. Wilhelm I, Fazakas C, Krizbai I, A. I*n vitro m*odels of the blood-brain barrier. *Acta Neurobiologiae Experimentalis.* 2011;71:113-128.

70. de Vries HE, Blom-Roosemalen MCM, van Oosten M, et al. The Influence of cytokines on the integrity of the blood-brain barrier in vitro. *Journal of Neuroimmunology.* 1996;64:37-43.

71. Balbuena P, Li W, Bissel-Magnin G, Meldrum B, Ehrich M. Comparison of Two Blood-Brain Barrier *In Vitro* Systems: Cytotoxicity and Transfer Assessments of Malathion/Oxon and Lead Acetate. *Toxicological Sciences.* 2009;114(2):260-271.

72. Hurst RD, Clark JB. Alterations in Transendothelial Electrical Resistance by Vasoactive Agonists and Cyclic AMP in a Blood-Brain Barrier Model System. *Neurochemical Research.* 1998;23(2):149-154.

73. Rosenberg GA. Neurological diseases in relation to the blood-brain barrier. *Journal of Cerebral Blood Flow and Metabolism.* 2012;32(7):1139-1151.

74. Muro S, Gajewski C, Koval M, Muzykantov VR. ICAM-1 recycling in endothelial cells: a novel pathway for sustained intracellular delivery and prolonged effects of drugs. *Blood.* 2005;105:650-658.

75. Marugan JJ, Zheng W, Muro-Galindo S, Inventors. DELIVERY OF TRANSTHYRETIN ACROSS THE BLOOD-BRAIN BARRIER AS A TREATMENT FOR ALZHEIMER'S DISEASE. 2009.

76. Ley K, Huo Y. VCAM-1 is critical in atherosclerosis. *Journal of Clinical Investigation.* 2001;107(10):1209-1210.

77. Peterson JW, Bo L, Mork S, Chang A, Ransohoff RM, Trapp BD. VCAM-1-Positive Microglia Target Oligodendrocytes at the Border of Multiple Sclerosis Lesions. *Journal of Neuropathology & Experimental Neurology.* 2002;61(6):539-546.

78. Altannavch T, Roubalova K, Kucera P, Andel M. Effect of High Glucose Concentrations on Expression of ELAM-1, VCAM-1 and ICAM-1 in HUVEC with and without Cytokine Activation *Physiological Research.* 2003;53:77-82.

79. Wagener F, Feldman E, de Witte T, Nader A. Heme Induces the Expression of Adhesion Molecules ICAM-1, VCAM-1, and E Selectin in Vascular Endothelial Cells. Society for Experimental Biology and Medicine; 1997.

80. Kanda T, Sriga T, Kubodera H, et al. Glycosphingolipid composition of primary cultured human brain microvascular endothelial cells. *Journal of Neuroscience Research.* 2004;78(1):141-150.

81. Guillotin B, Bourget C, Remy-Zolgadri M, et al. Human primary endothelial cells stimulate human osteoprogenitor cell differentiation. *Cellular Physiology and Biochemistry.* 2004;14(4-6):325-332.

82. L'Azou B, Fernandez P, Bareille R, et al. *In vitro* endothelial cell susceptibility to xenobiotics: Comparison of three cell types. *Cell Biology and Toxicology.* 2005;21(2):127-137.

83. Shen JS, Meng XL, Moore DF, et al. Globotriaosylceramide induces oxidative stress and up-regulates cell adhesion molecule expression in Fabry disease endothelial cells. *Molecular Genetics and Metabolism.* 2008;95(3):163-168.

84. Iademarco MF, Barks JL, Dean DC. Regulation of vascular cell adhesion molecule-1 expression by IL-4 and TNF-alpha in cultured endothelial cells. *The Journal of Clinical Investigation.* 1995;95(1):264-271.

85. Hamilos DL, Leung DY, Wood R, et al. Eosinophil infiltration in nonallergic chronic hyperplastic sinusitis with nasal polyposis (CHS/NP) is associated with endothelial VCAM-1 upregulation and expression of TNF-alpha. *American Journal of Respiratory Cell and Molecular Biology.* 1996;15(4):443-450.

86. Lockman PR, Mumper RJ, Khan MA, Allen DD. Nanoparticle Technology for Drug Delivery Across the Blood-Brain Barrier *Drug Development and Industrial Pharmacy.* 2002;28(1):1-13.

87. Vaidya A, Agarwal A, Jain A, Agrawal RK, Jain SK. Bioconjugation of polymers: a novel platform for targeted drug delivery. *Curr Pharm Des.* 2011;17(11):1108-1125.

88. Lobovkina T, Jacobson GB, Gonzalez-Gonzalez E, et al. In Vivo Sustained Release of siRNA from Solid Lipid Nanoparticles. *ACS Nano.* 2012/02/22 2011;5(12):9977-9983.

89. Uner M, Yener G. Importance of solid lipid nanoparticles (SLN) in various administration routes and future perspectives. *International Journal of Nanomedicine.* 2007;2(3):12.

90. Martins S, Costa-Lima S, Carneiro T, Cordeiro-da-Silva A, Souto EB, Ferreira DC. Solid lipid nanoparticles as intracellular drug transporters: An investigation of the uptake mechanism and pathway. *Int J Pharm.* Mar 23 2012.

91. Kuo Y-C, Wang C-C. Electrophoresis of human brain microvascular endothelial cells with uptake of cationic solid lipid nanoparticles: Effect of surfactant composition. *Colloids and Surfaces B: Biointerfaces.* 2010;76(1):286-291.

92. Robison A, Huang D, Jung H, Cremer P. Fluorescence modulation sensing of positively and negatively charged proteins on lipid bilayers. *Biointerphases.* 2013;8(1).

93. Hendrickson W, Pahler A, Smith J, Satow Y, Merritt E, Phizackerley R. Crystal structure of core streptavidin determined from multiwavelength anomalous

diffraction of synchrotron radiation. *Proceedings of the National Academy of Sciences.* 1989;86(7):5.

94. Hnatowich D, Virzi F, Rusckowski M. Investigations of avidin and biotin for imaging applications. *Journal of Nuclear Medicine.* 1987;28(8):9.

95. Dechancie J, Houk K. The origins of femtomolar protein-ligand binding: hydrogen bond cooperativity and desolvation energetics in the biotin-(strept)avidin binding site. *Journal of the American Chemical Society.* 2007;129(17):11.

96. Weber P, Ohlendorf D, Wendoloski J, Salemme F. Structural origins of high-affinity biotin binding to streptavidin. *Science.* 1989;243(4887):4.

97. BODIPY Dye Series. In: Johnson I, Spence MT, eds. *The Molecular Probes® Handbook—A Guide to Fluorescent Probes and Labeling Technologies*. 11 ed: Invitrogen; 2010.

98. Zhou Z, Liu Y, Miao AD, Wang SQ. Protocatechuic aldehyde suppresses TNF-alpha-induced ICAM-1 and VCAM-1 expression in human umbilical vein endothelial cells. *Eur J Pharmacol.* Vol 513. Netherlands2005:1-8.

99. Dbaibo GS, Obeid LM, Hannun YA. Tumor necrosis factor-alpha (TNF-alpha) signal transduction through ceramide. Dissociation of growth inhibitory effects of TNF-alpha from activation of nuclear factor-kappa B. *J Biol Chem.* Aug 25 1993;268(24):17762-17766.

100. Sharief MK, Ciardi M, Thompson EJ, et al. Tumour necrosis factor-alpha mediates blood-brain barrier damage in HIV-1 infection of the central nervous system. *Mediators Inflamm.* 1992;1(3):191-196.

101. Marui N, Offermann MK, Swerlick R, et al. Vascular cell adhesion molecule-1 (VCAM-1) gene transcription and expression are regulated through an antioxidant-sensitive mechanism in human vascular endothelial cells. *J Clin Invest.* Oct 1993;92(4):1866-1874.

102. Briscoe DM, Cotran RS, Pober JS. Effects of tumor necrosis factor, lipopolysaccharide, and IL-4 on the expression of vascular cell adhesion molecule-1 in vivo. Correlation with CD3+ T cell infiltration. *J Immunol.* Nov 1 1992;149(9):2954-2960.

103. Voinea M, Manduteanu I, Dragomir E, Capraru M, Simionescu M. Immunoliposomes directed toward VCAM-1 interact specifically with activated endothelial cells--a potential tool for specific drug delivery. *Pharm Res.* Nov 2005;22(11):1906-1917.

104. Dietrich JB. The adhesion molecule ICAM-1 and its regulation in relation with the blood-brain barrier. *J Neuroimmunol.* Vol 128. Netherlands2002:58-68.

105. Bhowmick T, Berk E, Cui X, Muzykantov VR, Muro S. Effect of flow on endothelial endocytosis of nanocarriers targeted to ICAM-1. *J Control Release.* Feb 2012;157(3):485-492.

106. Man S, Ubogu EE, Williams KA, Tucky B, Callahan MK, Ransohoff RM. Human Brain Microvascular Endothelial Cells and Umbilical Vein Endothelial Cells Differentially Facilitate Leukocyte Recruitment and Utilize Chemokines for T Cell Migration. *Clin Dev Immunol.* 2008;2008:8.

107. Pardridge WM. Blood-brain barrier drug targeting: the future of brain drug development. *Mol Interv.* Vol 3. United States 2003:90-105, 151.